Morphological Design of Nanoscale Polymer Systems:
Influence of Film Fabrication, Post-Processing Conditions, and Interfaces on Properties

by

J. K. Wenderott

A dissertation submitted in partial fulfillment
of the requirements for the degree of
Doctor of Philosophy
(Materials Science and Engineering)
in the University of Michigan
2018

Doctoral Committee:

Professor Peter F. Green, Chair
Professor John Kieffer
Professor Jinsang Kim
Assoc. Professor Pramod Reddy

J. K. Wenderott

jillkw@umich.edu; jwenderott@gmail.com

ORCID: 0000-0002-8419-2702

Dedication

This thesis is dedicated to my nephews, Tate Remington and Hudson Hayes, and to the future and dreams that belong to you.

Acknowledgements

The journey of a thousand miles. Graduate school can almost seem like this. My journey from start to finish was comprised of about three years and ten months, about 1400 days give or take. In this time, I was advised, supported, loved, encouraged, thoughtfully critiqued, and validated by many folks. There is not enough space to list everyone that impacted me, but there are a number of people that deserve special recognition.

First, I would like to thank my advisor, Prof. Peter Green. Peter has provided me support on many fronts throughout my graduate career, and his style of mentorship has allowed me the freedom to choose problems that I found interesting while also asking questions that stimulated my scientific curiosity. Peter's guidance in my time at the University of Michigan (UM) made me a better scientist, and for this I am grateful. Peter also invited me to attend the Joint Undertaking for an African Materials Institute (JUAMI) live-in school in June 2016 in Arusha, Tanzania, which, unknowingly at the time, prepared me for several international opportunities that I pursued later in graduate school. Without Peter, as well, I would not have climbed Mt. Kilimanjaro, so he deserves 19,341 feet of gratitude, literally. I would also like to extend special thanks to the rest of my committee, Prof. John Kieffer, Prof. Jinsang Kim, and Prof. Pramod Reddy. I have been fortunate to learn a lot from each of my committee members, whether this was through class instruction, direct one-on-one discussions, research collaborations, or even through students or post-docs that learned from them and passed this knowledge onto me.

Second, I would like to extend special thanks to several organizations, entities, and people both at the University of Michigan and otherwise that have supported me in my graduate career. In terms of financial support at various stages in my graduate career, I would like to acknowledge and thank the Rackham Graduate School at UM (Rackham Merit Fellowship), the Department of Materials Science and Engineering (MSE) at UM, and the National Science Foundation. I would also like to recognize the MSE Graduate Student Council and the Graduate Society of Women Engineers (GradSWE) at UM, two organizations where I found homes while at UM. These organizations provided me a place to grow as an organizer, grant writer, networker, and whole person. Special thanks to the MSE department chair, Prof. Amit Misra, graduate chair, Prof. Jinsang Kim (past) and Prof. Anisha Tuteja (current), and graduate coordinator, Renee Hilgendorf, and the rest of the MSE staff for their support of the MSE GSC goals. In addition, it was through GradSWE that I was able to visit Liberia in August 2017 and meet some of the most passionate, caring, and inspiring women I have ever known – the women of Liberia-SWE. These women changed my life.

Third, I want to acknowledge my scientific collaborators with which I have worked while at UM. Thank you (sorted by group or project): (1) Avi Bregman, Dr. Wesley Chapkin, and Prof. Alan Taub, (2) Da Seul Yang, Dr. Byeongseop Song, and Prof. Jinsang Kim, (3) Anubhav Raghav, Prof. Soumitra Satapathi, and Prof. Max Shtein, and (4) Dr. Nicki Baker and Prof. Robert O'Rourke. I also want to thank Dr. David Montiel Taboada for advice on data interpretation, and Dr. Mathew Boban and Prof. Anish Tuteja for their assistance collecting experimental data. It would be impossible to recognize collaborators without specially distinguishing my fellow and former Green group members (in alphabetical order): Abdulla Alqubati, Dr. Jojo Amonoo, Dr. Peter Chung, Dr. Ban Dong, Dr. Emmanouil Glynos, Dr. Kyle

Johnson, Andrew Li, Dr. Anton Li, Dr. Ravi Sharma, Dr. Aaron Tan, and Dr. Junnan Zhao. I owe so much to my Green group folks: office cube-mates (Anton, Kyle, and Ravi), best AFM teachers and gurus (Jojo and Aaron), first published paper co-author (Ban), not to mention the friendship, encouragement, and advice offered along the way.

Fourth, it would be impossible to forget my friendships I formed outside of lab. These folks kept me happy, sane, and contributed to me being my best self. To the fabulous people of the Wulff Pack, Traver Apt Crew, QE5, Bill Murray House (all iterations), Wolverine Den, In Da (Book) Club, and everyone that does not fit neatly into one (or several) of these categories: I owe you more than I can ever repay. From pitch and UM football games to meet-ups at TRC, TLW, WBC, ABC, the Kitty and beyond, to family dinners and Friendsgivings, I have been blessed beyond words for the joy and laughter you all have contributed to my life. For all my friends (from childhood, undergrad, and in-between) that are living their best lives in other locations outside of Ann Arbor, I also thank you for your support, love, and in a lot of cases, coming to visit.

Fifth, I would like to express my utmost appreciation and love to my family, mostly back in Kansas: my father, Doug; my mother, Chris; brothers, Adam and Todd; sister-in-law, Jenn; niece, Hannah; nephews, Tate and Hudson; grandmother, Janet; grandfather, Jim; and all of my aunts, uncles, and cousins. I miss you all every day, and I am entirely grateful for your presence in my life. I also specially recognize my late grandmother, Sharon, and late grandfather, Bill. My family, past and present, has taught me to value and believe in myself.

Lastly, I must thank my love, Bryan. It seems proper to both thank graduate school for bringing me to you and thank you for bringing me through graduate school. I owe so much to you. And Wendy, of course.

Table of Contents

List of Tables

List of Figures

List of Appendices

Abstract

Polymer thin films provide unique challenges and opportunities with properties that can be tuned by modifying the overall structure, or morphology. To realize improvement and implementation of polymer thin films in advanced applications, understanding of the intimate and complex connection between polymer morphology and properties is warranted. This dissertation focuses on the morphological design of polymer systems that exhibit unique properties and interpreting these systems in terms of a theoretical framework that exists to describe inherently-disordered polymer landscapes. The findings of this dissertation illustrate the wide tunability of properties accessible with informed design and control of (i) film fabrication, (ii) interfacial modification by self-assembled monolayers (SAMs) and interactions, and (iii) post-processing conditions.

Energy level alignment, and the corresponding band bending of the energy levels of conjugated polymers due to charge transfer at the polymer/electrode interface, impacts the performance of organic electronic devices. It was shown that the degree of band bending, known to vary between conjugated polymers, differs as significantly in a single conjugated polymer with varied morphologies. The morphologies investigated were fabricated via spin-casting and matrix-assisted pulsed laser evaporation (MAPLE), which imparts a unique globular morphology to conjugated polymer films. MAPLE-deposited films possessed stronger band-bending behavior and slower out-of-plane charge transport as compared to the spin-cast analogs. From band-bending data, a wider density of states (DOS) was extracted for the MAPLE-deposited films than

the spin-cast films, indicating more energetic disorder in the MAPLE-deposited films arising from the spatial disorder the films possess.

Modification of the interface between the conjugated polymer and electrode with polar SAMs changes the effective work function of the substrate and results in a surface energy change. These changes to the interface further affect band-bending behavior of conjugated polymer films. In MAPLE-deposited films, band-bending data was fit to extract a variety of DOS widths for these films atop varied substrates modified by SAMs. It was found that the surface energy of the substrate modified by the SAM influenced the thin MAPLE-deposited film morphology, with lower surface energy substrates yielding thin films that were rougher and possessed wider DOSs.

Post-processing with solvent annealing yields new morphologies upon subjection of fabricated films to solvent vapor. Band-bending behavior of conjugated polymer films revealed that solvent annealing led to more uniform spin-cast films, especially in the thicker films (>40 nm), with narrow DOSs. A separate study of solvent annealing on bismuth-based perovskite films noted the films had increased grain size, preferential grain orientation in the face-on direction, and reduction in film roughness upon solvent annealing. These structural changes led to improvements in both intragrain charge conductivity and power conversion efficiencies in devices containing the solvent-annealed films.

Interfacial interactions at the polymer/substrate interface are responsible for several thickness-dependent polymer properties like glass transition temperature and chain mobility. Strong (e.g. hydrogen bonding) interfacial interactions were seen to influence the morphology of an insulating polymer film near the substrate, with preferential vertical orientation of the average dipole moment, as compared to weak (e.g. van der Waals) interfacial interactions. Realized with

a combination of techniques to measure surface potential and ratios of in- to out-of-plane orientation of signature bonds of the polymer, these findings illustrate the influence of interfacial interactions on polymer thin film structure.

Chapter 1: Introduction

1.1 History of Structure-Property Control in Macromolecules

Polymers have held a prominent place in technological applications for centuries, beginning with natural polymers like silk, wool, and cellulose. With the advent of techniques at the turn of the 20th century to investigate structure and chemical composition of these natural polymers, the scientific study of macromolecules began.[1] Synthetic polymers, including the first synthetic plastic Bakelite,[2] were also developed around this time. Early semi-quantitative studies of small molecules, such as compositional and structural studies on sugars and amino acids by Emil Fischer in Berlin,[3] paved the way to synthesis of larger molecular species. In the 1920s and 1930s, development of experimental methods, including those enabled by the discovery of X-ray diffraction (XRD) in 1911 by von Laue and in 1912 by Bragg,[4,5] allowed for more systematic analysis of polymers to elucidate their structure in the solid state, average molecular weight, behavior in solution, and new synthesis pathways.[1,6] Continued advancements over the next few decades in polymer physics were realized with statistical thermodynamics models by Flory[7] and Huggins,[8] shape and size description by Kuhn,[9] and relaxation dynamics models by Rouse,[10] Zimm,[11] and de Gennes,[12] among others.

Alongside advancements in theory to understand polymer structure and dynamics, experimental structural characterization of polymeric systems has progressed significantly since the early to mid-1900s. In early XRD of semi-crystalline polymers, either produced by stretching

or arising naturally, the display of diffuse reflections and amorphous halos was observed, indicating the coexistence of both crystalline and amorphous regions in undetermined ratios.[13,14] Grazing incidence wide angle X-ray scattering (GIWAXS), a modern X-ray technique, offers the capability to quantify lattice parameters, crystallite orientation distributions, and degree of crystallinity of semi-crystalline polymers.[15,16] Other characterization techniques like variable angle spectroscopic ellipsometry (VASE) to determine average orientation of the polymer backbone relative to the substrate and atomic force microscopy (AFM) to assess film topography and roughness have also been recently implemented in the study of semi-crystalline polymers. Glassy polymers exhibit an amorphous structure, but this structure can be affected by externally applied stresses and packing variations caused by entropic and/or enthalpic effects.[17] Thus, structural changes in the form of packing differences in glassy, amorphous polymers are probed often with techniques that can measure relaxation dynamics of polymer chains, like broadband dielectric spectroscopy (BDS).[18,19]

Determination of the connection between structure and property is a cornerstone of materials science. Polymers, with their inherent long-range disorder due to weak chain-chain van der Waals (VDW) interactions, have a wide range of accessible morphologies that depend on various conditions to which the polymer is subjected during fabrication. These conditions influence the polymer chains in terms of configuration, packing density, formation of ordered aggregates, and interactions with external interfaces. The effect of morphology on properties of polymer films has been well documented in literature. Semiconducting, or conjugated, polymers possess both ordered aggregates and amorphous regions, and structural changes in these thin films due to interactions with interfaces are responsible for orders of magnitude difference in out-of-plane charge mobility.[20] Insulating polymers used as gas separation membranes show

varied performance with film roughness which can be controlled with solvent choice.[21] These are just two examples of many that illustrate the importance of morphological control of polymers to obtain desired properties.

Morphological design in thin polymer systems can be realized in several ways (see Figure 1.1). Dependent on the way in which the film is fabricated, the post-processing conditions imposed on the film, and the nature of the interface between the film and the substrate, a variety of film morphologies, and thus, film properties are available. As certain applications call for specific properties, precise tuning of polymer thin film morphology is desired for implementation of polymers in advanced applications both now and in the future. The work in this dissertation discusses several ways in which morphology can be controlled: (i) film fabrication by laser deposition (Chapter 2), (ii) introduction of self-assembled monolayers (SAMs) at the polymer/substrate interface (Chapter 3), (iii) post-processing via solvent annealing (Chapter 4), and (iv) interfacial interaction modification (Chapter 5). The work in Chapters 2-4 employs conjugated polymers as the subject of study and seeks to understand the effect of morphological changes on electronic properties. An additional study in Chapter 4 involves solvent-annealed bismuth-based perovskite films and the electronic properties obtained post-solvent annealing. The work in Chapter 5 utilizes an insulating polar polymer and investigates the effect of varying interfacial interactions on the thin film structure. The results of these chapters showcase the vast range of properties accessible by morphological design of polymers and other materials, and these findings are interpreted in terms of current theoretical models that exist.

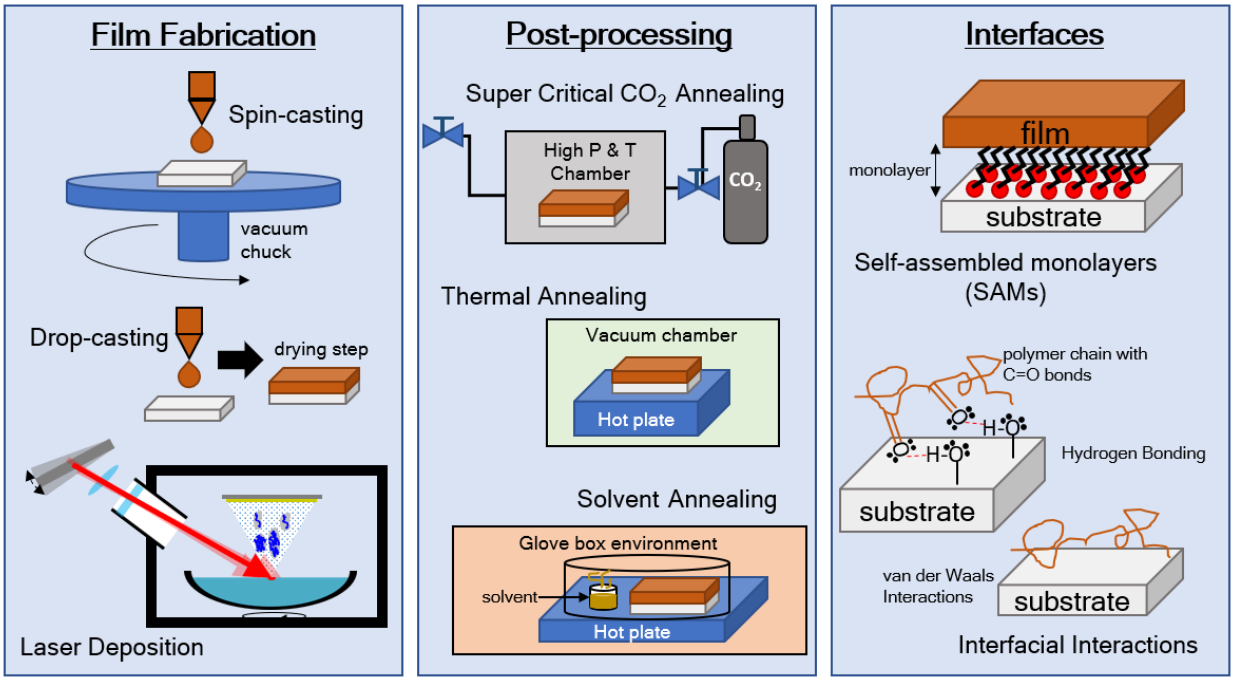

Figure 1.1.Tools for morphological design of conjugated polymers separated into three categories: film fabrication, post-processing, and interfaces.

1.2 Nanoscale Polymer Systems: Influence of Nanoconfinement

Increasingly, polymeric materials must function under various conditions of geometric confinement at the nanoscale. Research interest in this area stems from the experimental observations that functional properties such as elastic moduli,[22] ferroelectric behavior,[23] and charge carrier mobilities in conjugated polymers[24] can deviate from analogous bulk behavior when these materials are confined to length scales on the order of which their molecular relaxation processes occur. The driving forces behind this phenomenon are twofold: entropic "packing" and chain conformational effects, together with enthalpic intermolecular interactions with external interfaces.

Regarding entropic effects, the local packing of segments is perturbed in the vicinity of the interfaces because the density of packing of segments is not spatially uniform. For a nanoconfined homopolymer, simulations indicate that the density profile oscillates away from the substrate over a length scale (ξ) of ~ 1 nm.[25,26] In addition, the packing of monomers and their respective orientation changes at interfaces largely manifest the effects of short-range intermolecular interactions.[27–29] Generally, the dynamics at a "wall" are anisotropic, and the relaxations of the segments normal to the substrate are slow compared to the bulk. This sluggishness is suggested to be due to the longer time scales associated with desorption of segments from the walls, or correspondingly, decreased configurational freedom of the chains in the proximity of the substrate. In essence, interactions of a chain segment in contact with a wall reduce the relaxations of a chain by increasing the activation barriers. Stronger interactions with the walls lead to longer desorption times and hence slower dynamics.[29] Correspondingly, at a free surface, simulations show that local packing constraints are not as severe (larger configurational freedom) as they are at a hard wall.[27,30–33] These simulations reveal the existence of a mobile surface layer with thickness on the order of ~ nms.

Much of these initial predictions are now supported by experimental observations. For freely-standing polymer films, the average T_g of the film decreases in relation to the bulk, provided the film is sufficiently thin.[34–36] The same is generally true for asymmetrically-confined films – existence of a free surface and an interface in contact with a substrate – where the polymer interactions with the substrate are weak van der Waals (VDW) forces.[37–41] This T_g depression is due to the previously mentioned mobile surface layer at the polymer-free surface interface. Even in cases of asymmetrically confined supported films, the additional configurational mobility at the free surface is sufficient to overcome reduced mobility at the

polymer-substrate interface. On the other hand, for cases where there exists attractive interactions between the polymer and substrate (e.g. hydrogen bonding) the average T_g of the film is greater than that of the bulk.[39,42–44] In such cases, the strength of the enthalpic interactions dictates the deviation in the glass transition.

Experimental observations show that changes in the T_g of thin films occur over much longer length scales (h) than the density fluctuation length scales (ξ). Theory by Schweizer and coworkers[45] provides a molecular perspective for this behavior. They consider a chain segment as caged, such that the size of the cage is the first minimum in the radial distribution function on the order of the monomer size. The requirement of cooperativity reveals that the motions of a chain segment must be facilitated by local volume dilations of the cage. This increase in local volume is accommodated by long-range elastic fluctuations, producing an elastic energy barrier. In the case of a free surface, the number of nearest neighbors is smaller, and the elastic energy barrier is "cut off". At the substrate, when strong intermolecular interactions exist, there are large energetic barriers for chain cooperative motion. In the case of weak VDW interactions at the substrate, the elastic energy barrier is weak, and deviations in T_g are nonexistent.

In addition to T_g deviations, interactions at the substrates can also lead to deviations in various chain relaxation processes (side chain,[46] segmental,[47] end-to-end[48]). There is still some debate as to the extent of these effects,[40,49,50] as the length scales over which the T_g appears to be affected by substrate interactions is comparatively large ($h >> \xi$), approaching the order of ~100s nm depending on geometry. On the other hand, the length scales (L) over which such effects affect chain dynamics are much smaller ($L \sim \xi$). This connection between thermal measurements such as the glass transition and dynamic measurements such as segmental relaxations under nanoconfinement is still a topic of debate.[51,52] Furthermore, the connection between dynamics

and T_g under various conditions of hard and soft confinement remains poorly understood. In this dissertation, we further probe the length scales over which an interface influences a polymer film by investigating the effects of different types of interfacial interactions (strong versus weak) on thin film polymer morphology (Chapter 5).

1.3 Conjugated Polymers

With the studies of Chapters 2-4 relying heavily on semiconducting, or conjugated, polymers, a brief introduction to these materials is warranted. This introduction will include a discussion of charge transport mechanisms, how the disordered nature of a conjugated polymer affects charge transport, a theoretical model widely used to understand charge transport, and a brief view of what occurs in a device from a charge carrier standpoint when a conjugated polymer film and a conductive electrode are brought together.

1.3.1 Mechanisms for Charge Transport

Conjugated polymers are defined as long chain molecules that possess alternating single

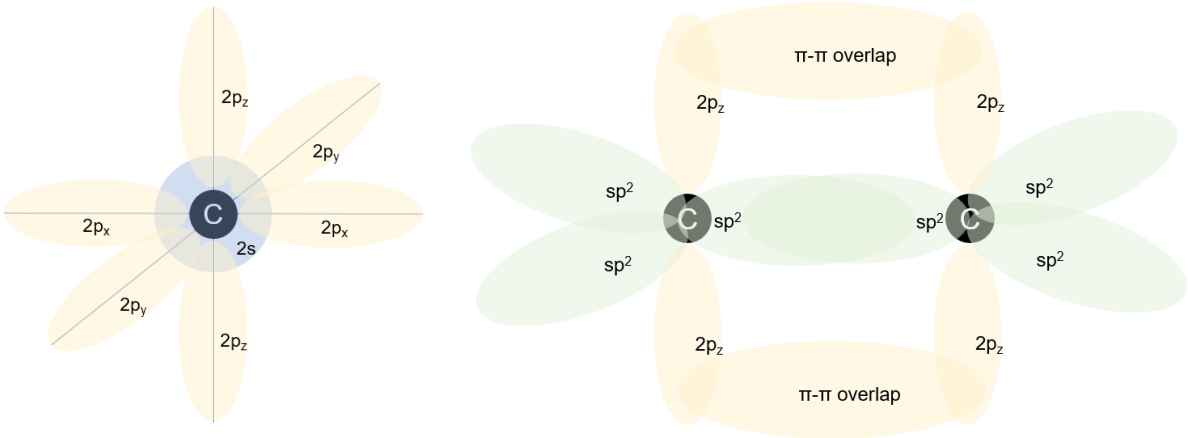

Figure 1.2. Molecular orbitals of isolated carbon atom (1s not shown) (left). Hybridization of 2s and 2p orbitals of two carbon atoms with p_z orbital overlap for delocalization of electrons and charge transport intra-chain (1s not shown) (right).

and double carbon bonds along their backbone. The carbon atoms along the backbone are considered sp^2 hybridized. This means that the 2s orbital mixes with two of the three available 2p orbitals to form three "directional" sigma bonds (three sp^2 orbitals), leaving one remaining 2p orbital that is oriented out of the plane of the polymer backbone (p_z direction) that is available to participate in pi (π)-bonding (see Figure 1.2). The electrons in these π orbitals can overlap with neighboring π orbitals, leading to electron delocalization across the polymer chain. This enables charge conduction along the length of the chain (intra-chain transport), provided the chain is free of kinks and/or twists that break the π orbital overlap in the chain.

Charge transport in conjugated polymers is a fundamentally different process than that occurring in inorganic semiconductors. Inorganic semiconductors, with atoms at determined locations on a crystalline lattice, have generally well-defined band structures that dictate charge transport. Organic semiconductors, including both small molecules and conjugated polymers, are

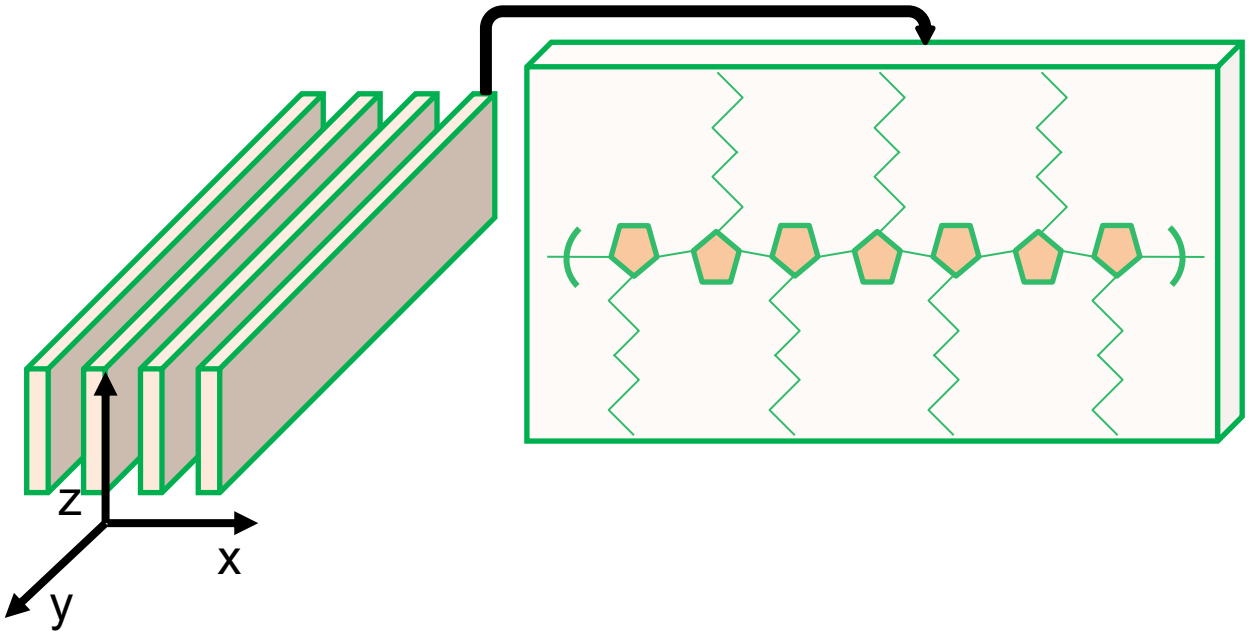

Figure 1.3. Various pathways for charge transport in conjugated polymer in order of efficiency – intra-chain (**y-direction**), inter-chain via π-π stacking (**x-direction**), inter-chain across side chains (**z-direction**) (left). An orientation of a single chain is shown (right).

molecular structures, and charges are transported via a hopping mechanism between available sites. In conjugated polymers, charges can be transported intra-chain, which is the most efficient mode of transport, or inter-chain if two chains are close enough that their π orbitals overlap, leading to so-called "π-π stacking". Inter-chain transport is less efficient than intra-chain due to the larger distances associated with the transport and weaker coupling of the orbital overlap. Generally speaking, it is also possible for charges to be transported inter-chain across side groups. Because of the traditionally bulky side groups that do not possess conjugation, this is a much less efficient mode for transport. The directions for transport in conjugated polymers are shown schematically in Figure 1.3.

1.3.2 Impact of Disorder on Transport

As mentioned previously, the most efficient mechanism for charge transport is intra-chain across the length of the polymer chain. It is often not possible for a charge to traverse the entire length of the polymer chain due to kinks in the polymer chain. In this case, if the energy barrier is large enough, the charge must hop to a different chain to continue its motion. Since carrier motion inter-chain is slower than intra-chain, the mobility significantly decreases with inter-chain hopping. This is one example of how charge carrier mobility can be specifically influenced by the structure of the chains at the nanoscopic scale.

In addition, the microscopic and macroscopic morphology of the conjugated polymer plays a role in the mobility of carriers. The semi-crystallinity of conjugated polymers originates from the coexistence of amorphous regions and ordered aggregates. The weak VDW forces between polymer chains, as well as the numerous conformations a single chain can have, lead to an inevitable degree of structural disorder and energetic traps present following fabrication and post-processing of films. Increasing the size of the aggregates with respect to the amorphous

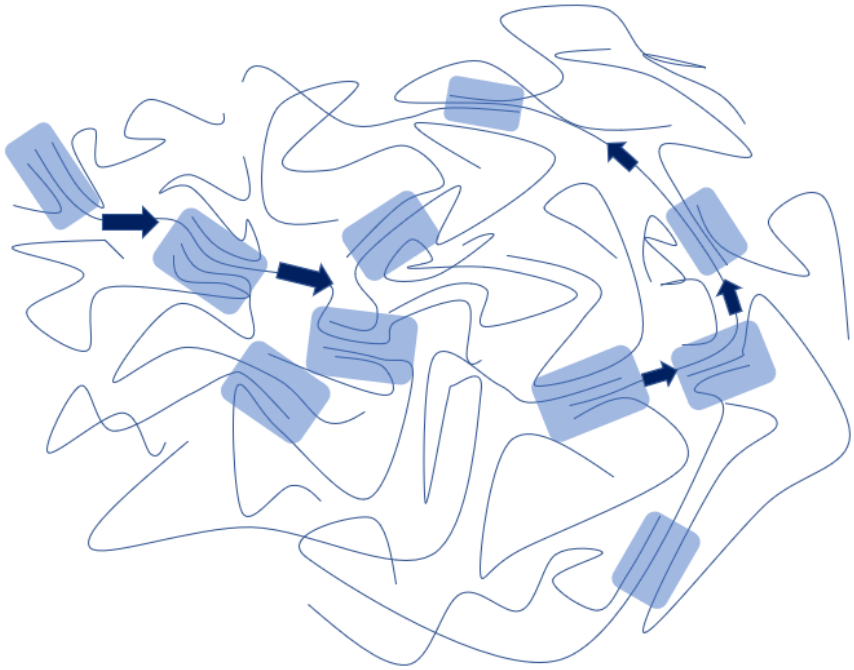

Figure 1.4. Schematic of ordered aggregates (blue background) and amorphous regions (white background) in conjugated polymer. Arrows show "tie-molecules" connected aggregates.

regions improves crystallinity of the conjugated polymer. The high carrier mobilities of highly-crystalline P3HT and poly(2,5-bis(3-alkylthiophen-2-yl)thieno[3,2-b]thiophene) (PBTTT) initially indicated that long-range order due to high crystallinity was critical to the efficient movement of carriers.[53,54] While improved crystallinity allows for less hindered motion of carriers along the polymer backbone or between overlapping π-orbitals within aggregates, charges must also be able to traverse between aggregates along "tie-molecules" for efficient transport (see Figure 1.4).[55] This confining of charge carriers to aggregates results because of the energy barrier encountered as a carrier tries to move from ordered aggregate to amorphous region. Improved connectivity between aggregates explains why molecular weight tends to improve carrier transport in conjugated polymers, even though crystallinity is decreased.[56,57] Thus, several factors are influential to carrier transport in conjugated polymers with inherent disorder, including aggregation, molecular weight, chain rigidity, and chain packing.[55,57]

1.3.3 Charge Transport Theory: Gaussian Disorder Model

In a conjugated polymer, modelling how charge carriers are transported requires a framework that accounts for both structural and energetic disorder. The most commonly utilized model that accounts for these two terms of disorder is the Gaussian Disorder Model (GDM), originally described by Bässler.[58,59] The GDM describes both the electric field and temperature dependencies of carrier transport in conjugated polymers. Charge transport occurs between elementary sites, either those participating in transport or defects, that have energies subjected to a Gaussian distribution. In the simplest case, hopping between sites is uncorrelated, though further corrections to the GDM have been proposed to include correlated behavior.[60] Hopping rates between sites are dictated by the Miller-Abrahams equation (1.1):

$$v_{ij} = v_0 e^{-2\gamma a \frac{r_{ij}}{a}} \times e^{-\frac{\varepsilon_j - \varepsilon_i}{kT}} \; for \; \varepsilon_j > \varepsilon_i$$

$$v_{ij} = v_0 e^{-2\gamma a \frac{r_{ij}}{a}} \times 1 \qquad for \; \varepsilon_j \leq \varepsilon_i \tag{1.1}$$

where v_{ij} is the hopping rate between two sites i and j with energies ε_i and ε_j, v_0 is the frequency pre-factor, γ is related to the electronic coupling between sites, a is the average lattice distance, and r_{ij}/a is the relative jump distance between sites. As seen in equation (1.1), charge carriers move to higher energy sites in a thermally-activated process. If a charge carrier moves to a site lower in energy, a random walk is executed.

The GDM predicts a non-Arrhenius temperature dependence of carrier mobility, scaling as $1/T^2$. The temperate and electric field dependencies of carrier mobility are described using the following equation (1.2):

$$\mu(T,E) = \mu_0 \exp[-\tfrac{2}{3}\left(\tfrac{\sigma}{kT}\right)^2] \exp\{C[\left(\left(\tfrac{\sigma}{kT}\right)^2 - \Sigma^2\right] E^{\frac{1}{2}}\} \tag{1.2}$$

where μ is mobility, T is temperature, E is electric field, σ is the Gaussian DOS width, Σ describes positional disorder, and C is a fitting parameter. The GDM, as indicated by this equation, predicts that positional disorder can have a negative influence on the carrier mobility as the electric field is increased. Carriers in high electric fields, able to overcome energy barriers, are forced to take shorter, but slower, routes from point to point. It is noted here that there can be contributions from both polaronic (charge carrier and its distorted surroundings) and disorder-induced effects (energetic sites with Gaussian distribution), and these contributions together manifest themselves as logμ behavior being between $1/T$ and $1/T^2$ dependencies.[61] These contributions can be separated with carefully-controlled experiments, though both polaronic "self-trapping" of carriers and Gaussian disorder have similar influences on charge transport. In the following chapters, equation (1.2) will be utilized primarily, because in our experiments the logμ follows a $1/T^2$ dependency and a decrease in mobility with increased electric field has also been noted, which is predicted by the GDM.

1.3.4 Transport at the Conjugated Polymer/Electrode Interface

At the device level, the ways in which charges are transported between the conjugated polymer and electrode at their interface is significant for device processes and performance. Though conjugated polymers have charge transport governed by hopping between molecular sites, band-like behavior has been observed in polymers with high carrier concentrations, either due to doping or intrinsic levels.[62–64] When the conjugated polymer and electrode are brought into contact, the Fermi levels of the two materials align. If the work function of the substrate exceeds a critical value so that the built-in potential between the polymer and electrode Fermi levels is "large", upon contact there will be charge transfer into the tail states of the conjugated polymer, resultant in band bending of the highest occupied molecular orbital (HOMO) and

lowest unoccupied molecular orbital (LUMO) levels toward the occupied tail states in the energy gap. This band-bending phenomenon has been noted in various conjugated polymers on a variety of substrates, and the degree of band bending has been proposed to depend on the work function of the substrate and the electronic structure of the conjugated polymer.[62] Based on the GDM and the intertwined landscapes of structural and electronic disorder, a connection between morphology and electronic structure of a conjugated polymer necessarily exists, and in fact is shown explicitly in Chapter 2. From band-bending data, it is possible to extract the density of tail states (DOTS) width to clarify electronic disorder in conjugated polymers, making the measurement of band bending quite useful.

1.4 Polymer Morphology Design Tools

With the connection between morphology and properties clearly elucidated, the ability to control morphology to design polymer films with well-defined properties is desired. As noted in several examples in this dissertation, many polymer properties are not intrinsic to the material, but instead tunable depending on how precisely the film is fabricated or processed post-fabrication. Several morphological design tools are discussed here, though the list is not exhaustive.

First, films may be fabricated in a variety of ways, including spin casting and drop casting. In these two methods, the polymer is mixed with solvent with which it is miscible, and the solution is either dropped on a spinning substrate (spin casting) or on a still substrate (drop casting). The solvent evaporates to leave the film behind. In these two cases, the thickness and structure of the film can be altered by many parameters, including concentration, spin speed, and choice of solvent. Films can also be deposited with a laser, as shown in Chapters 2 and 3. The

method utilized in these chapters is known as matrix-assisted pulsed laser evaporation (MAPLE). In MAPLE, a laser targets a frozen polymer/solvent mixture in a high vacuum chamber. Most of the energy is absorbed by the solvent, limiting polymer degradation. A plume of organic material and solvent is ejected toward the substrates rotating above the frozen mixture. The volatile solvent is removed under the high vacuum environment, leaving the organic material to be deposited on the substrates. Unique globular film morphology is accessible with this technique.

Second, processing films post fabrication can vastly alter polymer film morphology. Included in post-processing techniques are annealing procedures, like thermal, solvent, and super critical CO_2 annealing. Thermal annealing involves application of heat to the film, either in an ambient or inert environment. In solvent annealing, films are exposed to solvent vapor that can penetrate the film or lead to a liquid or quasi-liquid state at the surface of the film. Solvent annealing was used in Chapter 4 to post-process both conjugated polymer films and bismuth-based perovskite films. Super critical CO_2 annealing subjects films to super critical CO_2 fluid at a well-defined temperature and pressure. This "green" post-processing technique has proven successful in altering conjugated polymer morphology near the interface of the polymer/substrate, leading to enhanced in-plane carrier transport properties.[65]

Finally, tailoring interfacial interactions allows for the modification of polymer morphology and properties, especially in thin films in which the area near the interface comprises a sizeable volume percentage of the total film. SAMs were employed in Chapter 3 at the conjugated polymer/electrode interface. Other interfacial constituents, like molecular films and surface modifiers, have also been applied to change the interaction at the interface, resultant in a variety of consequences like change to substrate work function and surface energy. These alterations of substrate work function and surface energy have implications for both band-

bending behavior and film morphology. Furthermore, manipulation of the strength of interfacial interactions can impact thin film polymer structure, as considered in Chapter 5. For instance, if the polymer can hydrogen bond with its substrate (strong interfacial interaction) as opposed to weak VDW bonding, the thin film structure near this interface can be influenced.

Chapter 2: Film Fabrication: Influence on Morphology and Electronic Properties of Conjugated Polymer Films

Reproduced from Wenderott, J. K; Dong, B. X.; Green, P.F. Band Bending in Conjugated Polymer Films: Role of Morphology and Implications for Bulk Charge Transport Characteristics. *J. Mater. Chem. C* **2017**, *5* (30), 7446-7451 from Reference [66] with permission from the Royal Society of Chemistry.

2.1 Introduction

Understanding energy level alignment at interfaces in organic electronic devices is critical to their optimal performance both in terms of power conversion efficiencies and stability. Band bending in conjugated polymers, initially believed to not occur due to the distribution of localized electronic states as opposed to the band structure of crystalline inorganic semiconductors, is possible when the density of charge carriers in the polymer is either increased due to doping or the intrinsic values are sufficiently high, leading to a depletion region upon contact between the polymer and a conductive substrate.[62–64] Shifting, or bending, of the highest occupied molecular orbital (HOMO) and the lowest unoccupied molecular orbital (LUMO) energy levels of a polymer occurs at the interface as the Fermi levels (E_F) of the two materials align, or equilibrate, upon contact.[62,67–69] This alignment, resulting in band bending, is a direct result of charge transfer that occurs between the conductive substrate (metal – M) and the

electronic energy states of the conjugated polymer (organic semiconductor – O) close to the substrate.[70] Studies of organic semiconductor/metal (O/M) interfaces have shown band bending depends on both the electronic structure of the conjugated polymer and the work function of the substrate.[62,71]

While several studies have explored the effect of different substrate work functions, virtually no studies have clearly elucidated how band bending at the conjugated polymer (O)/conductive substrate (metal (M) or semiconductor (I – inorganic)) interface is influenced by the morphology of the polymer. Carrier transport models for structurally-disordered organic material systems include terms that quantify the role of both positional (i.e.: distribution of hopping site distances) and energetic disorder (statistical distribution of energy states).[58] These models implicate a connection between morphology, electronic structure and, thus, band bending. More recently, experiment and calculation have shown that changing the backbone orientation of conjugated polymer films significantly impacts both energy level alignment at O/O and O/I interfaces and also bulk charge carrier transport.[20,72–74] In order to investigate the role of morphology we employed two very different strategies to prepare poly(3-hexyl thiophene) (P3HT) films on conductive indium tin oxide (ITO)/poly(3,4-ethylenedioxythiophene):polystyrene sulfonate (PEDOT:PSS) substrates. The two fabrication methods were conventional spin-casting and the novel matrix-assisted pulsed laser evaporation (MAPLE). We find that depending on the fabrication conditions, the morphology of P3HT films changes, severely impacting band bending, density of states (DOS), and out-of-plane charge transport properties. Our results highlight the role morphology plays in energy level alignment at the O/M interface.

2.2 Experimental Section

2.2.1 Preparation of Spin-Casted and Matrix-Assisted Pulsed Laser Evaporation (MAPLE)-Deposited Samples

All substrates were cleaned by ultrasonication in an Alconox® detergent solution, DI water, acetone, hot Hellmanex® solutions and 2-propanol for 5 minutes each, followed by UV-ozone treatment for 20 minutes. Kelvin probe force microscopy (KPFM) and current extracted by linearly increasing voltage (CELIV) measurements were performed on polymer films on indium tin oxide (ITO)/glass substrates coated with a layer of poly(3,4-ethylenediosythiophene): polystyrene sulfonate (PEDOT:PSS).

Poly(3-hexylthiophene) (P3HT) (Reike Metal, ~95% regioregularity, Mw = 50,000 g/mol) solutions were prepared by dissolving the polymer in 1,2-dicholorobenzene (DCB). Solutions were allowed to mix overnight before being filtered with 0.45 µm polytetrafluoroethylene (PTFE) filter. To make the spin-casted films, filtered solutions were spun onto prepared substrates at 600 rpm for 2 minutes.

MAPLE deposition was performed with a system purchased from PVD products with a Er:YAG laser (Quantel) of 2.94 µm wavelength. An emulsion-based approach[75] was utilized in which the P3HT was dissolved in DCB and then mixed with benzyl alcohol and deionized water that contained 0.0005 wt % sodium dodecyl sulfate surfactant at a ratio of 1:0.3:3. To create an emulsion, the mixture was ultrasonicated until visibly homogeneous. The emulsion was then placed in a cooled (-170 °C) target cup, and upon freezing, the chamber was pumped to a high vacuum condition (< 2 x 10-5 Torr). ITO/PEDOT substrates were placed 5.5 cm above the target cup, and both the target cup and the substrates were kept at constant rotation during deposition. The laser fluence was maintained at ~1.3 J/cm2 at a repetition rate of 5 Hz as it rastered across

the frozen emulsion surface. The deposition time was varied to achieve varying thicknesses of P3HT films. Thicknesses of the samples were confirmed with spectroscopic ellipsometry.

2.2.2 Work function Measurement by Kelvin Probe Force Microscopy (KPFM)

KPFM measurements were performed using Pt-coated Si probes made by Nanosensors (stiffness ~0.5-1 N/m, resonant frequency ~75 kHz) on an Asylum Research MFP3D atomic force microscope. Most measurements were made in air with 10-30% humidity. KPFM acts as a double-pass, intermittent contact technique. First, the sharp metallic tip raster-scans across the surface of interest, measuring the topography. During the first pass, the cantilever is driven at its first harmonic resonance frequency, and the amplitude of this mechanical oscillation is used as the feedback signal. In the second pass, which follows the same path as the first pass, an AC bias at the first harmonic resonance frequency of the cantilever is applied to the tip that generates oscillating electrical forces between the tip and sample. The mechanical oscillations of the cantilever are set to zero and the tip is lifted to a set height ("lift height"). This distance is between 10-20 nanometers, which captures the electrostatic interactions but remains far removed from short-range VDW forces. A lock-in amplifier is employed to extract the electrical force component with the first harmonic frequency and apply a DC bias until this oscillation is nullified. These oscillations are continually nullified as the tip follows the second pass, providing a local map of the surface potential.

Shown theoretically, an AC bias, applied to the tip during the second pass, leads to an electrostatic force between the tip and sample that is given by:

$$F_{el} = -\frac{1}{2}\Delta V^2 \frac{\partial C(z)}{\partial z}, \tag{2.1}$$

where z is normal to the sample surface, ΔV is the voltage difference between the tip and the contact potential difference and dC/dz is the capacitive gradient between the tip and sample. The voltage difference can be written as:

$$\Delta V = V_{tip} - V_{CPD} = (V_{DC} - V_{CPD}) + V_{AC}\sin(\omega t), \tag{2.2}$$

where $V_{DC}+V_{AC}sin(\omega t)$ is the voltage applied to the tip and V_{CPD} is the contact potential difference voltage. By plugging equation (2.2) into (2.1), the electrostatic force is given by:

$$F_{el} = -\frac{1}{2}\frac{\partial C(z)}{\partial z}[(V_{DC} - V_{CPD}) + V_{AC}\sin(\omega t)]^2. \tag{2.3}$$

This electrostatic force can be separated into three components – one static, one dependent on the first harmonic (ω) and one dependent on the second harmonic (2ω). The component dependent on the first harmonic, sought with KPFM, is given by:

$$F_{\omega} = -\frac{\partial C(z)}{\partial z}(V_{DC} - V_{CPD})V_{AC}\sin(\omega t) \tag{2.4}$$

Equation (2.4) shows, if the DC bias is applied to match that of the CPD, $F_{\omega} = 0$ and electrical oscillations of the tip will be nullified. In this way, the applied DC bias is equal to that of the CPD and this value can be acquired across the surface of the sample. The V_{CPD}, as first seen in equation (2.2), is defined as:

$$V_{CPD} = \frac{\varphi_{tip} - \varphi_{sample}}{-e}, \tag{2.5}$$

where φ_{tip} and φ_{sample} are the work functions of the tip and sample, respectively, and $-e$ is the elementary charge. As equation (2.5) shows, the work function of the tip must be known to find the absolute work function of sample. This is accomplished through the use of highly ordered pyrolytic graphite (HOPG), which has a well-defined work function of 4.6 eV. A schematic of the KPFM technique is provided in Appendix A.

2.2.3 Out-of-Plane Mobility Measurements by Current Extracted by Linearly Increasing Voltage (CELIV)

The out-of-plane carrier mobility measurement was conducted on samples of ~ 100 nm thickness. The triangle voltage for the CELIV measurement was created by a BK Precision 4075 function generator and the responded current was amplified using a FEMTO amplifier before being recorded by a Tektronix digital oscilloscope. All of the mobility measurements were carried out in a vacuum cryostat (Janis Inc.) at specific temperatures controlled by a temperature monitor (LakeShore Cryotronics). In a CELIV measurement, there are two major contributions to the responded current: the displacement current $j(0)$ due to the geometric capacitance of the sample and the drift current $\Delta j = j - j(0)$ resulting from the extraction and flow of free charge carriers within the film. The hole mobility μ in a CELIV measurement is calculated using the following relation[76]

$$\mu = \frac{2h^2}{3At_{\max}^2(1+0.36\frac{\Delta j}{j(0)})} \tag{2.6}$$

Here, h is the film thickness, A is the voltage ramping rate and t_{max} is the time at which the current reaches the maximum value. The electric field dependence measurement at each temperature was performed by changing the ramping rate, A (electric field, $E = At_{max}/h$).

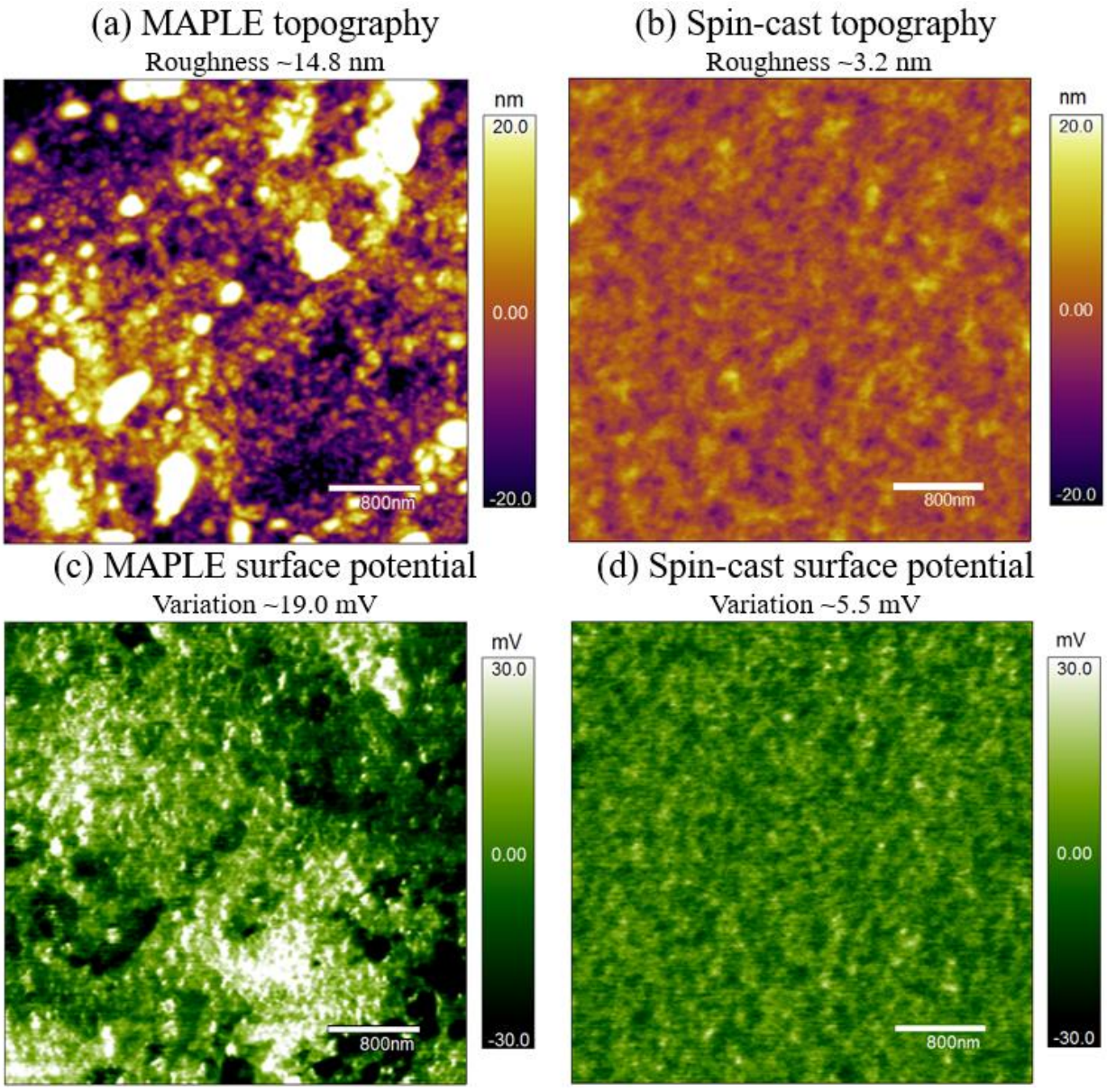

Figure 2.1. Comparison of topography (a and b) and surface potential (c and d) scans of MAPLE-deposited (a and c) and spin-cast (b and d) P3HT films. Roughness of topography and surface potential are listed, showing the variations are larger for the MAPLE-deposited samples. MAPLE-deposited and spin-cast films are ~70 nm and ~50 nm thick respectively.

2.3 Results and Discussion

It should be noted that in both spin-cast or MAPLE-deposited films, the contacts made between the P3HT and the ITO/PEDOT:PSS substrate would be categorized as weakly interacting, implying the energetics at the interface are controlled entirely by charge transfer.[62] As seen in Figure 2.1a and 2.1b, MAPLE-deposited P3HT films are significantly rougher than their spin-cast counterparts (more than four times) and possess a globular morphology consistent with previous reports of MAPLE-deposited polymer films.[15,77–79] In this case, the representative films in Figure 2.1 correspond to the thickest films tested (~70 nm, MAPLE-deposited and ~50 nm, spin-cast) on ITO/PEDOT:PSS with atomic force microscopy (AFM) techniques. This globular morphology is due to the deposition mechanism: a laser targets a frozen mixture of the polymer and solvent and a resultant plume of polymer droplets is directed toward the substrate. Because the energy of the laser is absorbed primarily by the solvent host, degradation of the polymer molecular weight is minimized, which makes MAPLE more attractive for vacuum deposition of polymer thin films than other physical laser deposition methods.[75]

It is also evident from Figure 2.1c and 2.1d that the surface potential across a MAPLE-deposited P3HT film has greater variation than that of the spin-cast sample. This surface potential corresponds to the DC bias required to nullify mechanical oscillations of an AFM tip at its first harmonic frequency at all points across the surface map. This method, Kelvin probe force microscopy (KPFM), utilizes the null-detection condition to provide the contact potential difference (V_{CPD}), which is precisely equal to the DC bias applied to the tip. The V_{CPD} can be related to the work function of the sample (ϕ_{poly}) through the simple relation shown previously, equation (2.5).

KFPM was specifically chosen to measure the work function of the P3HT samples for several reasons. First, similar to macroscopic Kelvin probe (KP), KPFM is performed in the dark, so samples that are highly conductive, semiconductive, and insulating at varying thicknesses can be tested without charging of the sample taking place. Additionally, KPFM is not dependent on charge transport as certain other methods of assessing DOS, which removes it from concerns of measuring an effective DOS since charge transport depends on the DOS. Finally,

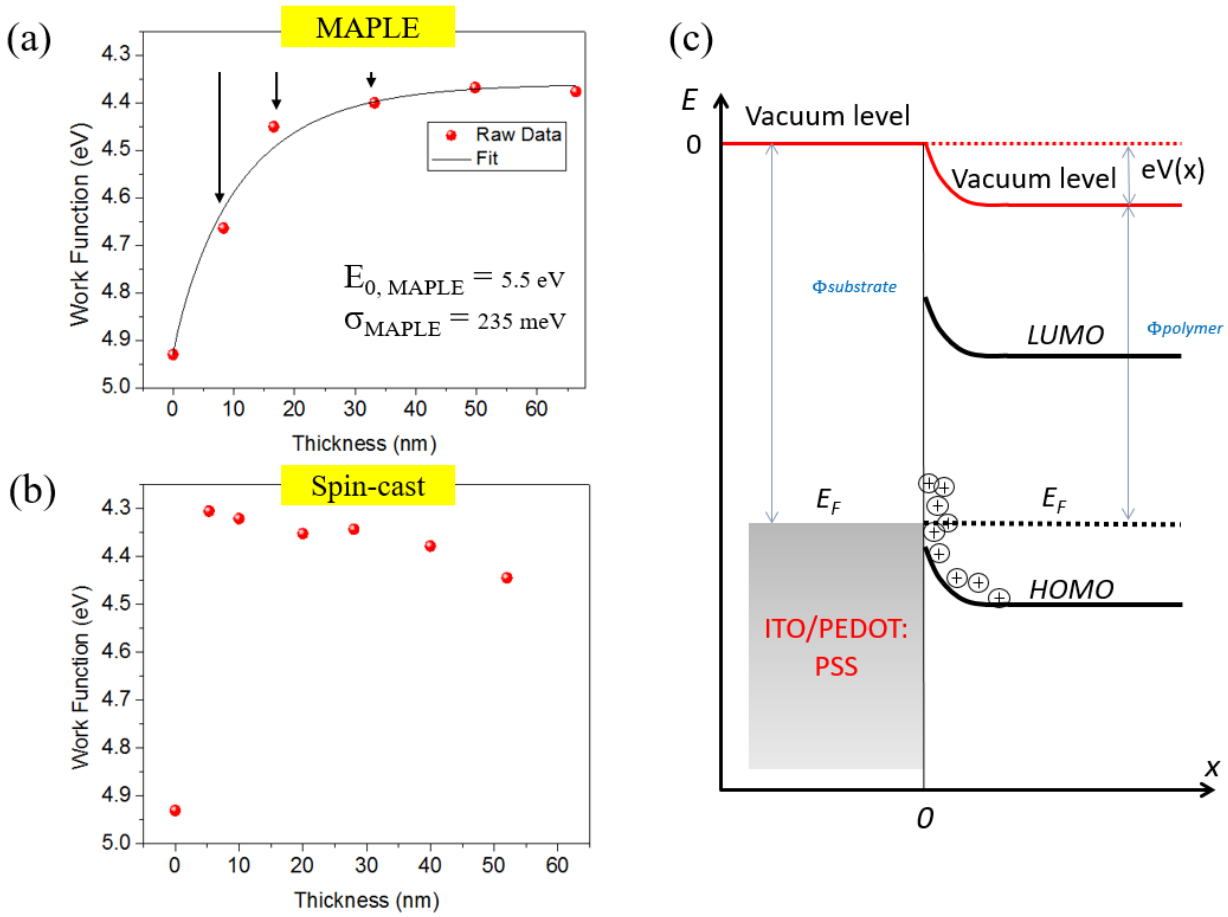

Figure 2.2. The changes to the work function of the films (with h=0 being the work function of the uncoated ITO/PEDOT:PSS substrate) with thickness indicate a much stronger band-bending effect (see arrows) in MAPLE-deposited P3HT films (a) than in spin-cast P3HT films (b), which show little to no band-bending behavior. Band bending of P3HT is illustrated (c) with vacuum level offset (eV(x)) when the Fermi levels of the substrate and polymer align. In (a) and (b), the error bars of the work functions calculated from the surface potential fluctuations are smaller than the data points and not included.

unlike macroscopic KP, KPFM is a surface and sub-surface measurement with a certain depth of probe, which depends on the characteristics of the sample. Experimental tests on P3HT films have shown this depth of probe can extend to 100 nm.[80] This depth of probe is important especially if the area of interest is located at a buried interface or if the intent is to probe a volume extending a certain thickness into the sample. More details of the principles and experimental procedures for KPFM can be found in the Experimental Section and elsewhere.[81]

The work functions measured by KPFM for both MAPLE-deposited and spin-cast P3HT samples as a function of film thickness are plotted in Figure 2.2a and 2.2b, with h=0 equalling the work function of the ITO/PEDOT:PSS substrate. In this case, the work function of the P3HT film corresponds to the vacuum energy level offset at the O/M interface after energy level alignment. It is clearly seen in Figure 2.2a that with decreasing thickness the MAPLE-deposited samples exhibit band bending, with apparent work function values of the polymer film approaching that of the substrate at thicknesses less than ~20 nm. This shift in the measured work function values of the polymer film is characteristic of charge injection into the tail states of the DOS. In stark contrast, no clear band-bending effect is observed at the thicknesses probed with KPFM for the spin-cast sample, as shown in Figure 2.2b.

The observed band-bending effect can be quantified further by fitting to find the DOS of the MAPLE-deposited sample using the equation for a spatially inhomogeneous charge distribution:

$$n(x) = \int_{-\infty}^{\infty} \frac{1}{1+\exp[\frac{E-E_F}{k_B T}]} g[E + eV(x)]dE, \qquad (2.7)$$

where $n(x)$ is the charge-carrier density at a distance x from the O/M interface, E is the energy, E_F is the equilibrium Fermi energy level, k_B is Boltzmann's constant, T is the temperature, $g(E)$ is

the model DOS, and *V(x)* is the electrostatic potential at a distance *x* from the O/M interface. *V(x)* is found by solving the 1D Poisson's equation using the boundary conditions *V(0)*=0 and $V(\infty)=\phi_{poly}$. More details for fitting are explained in detail elsewhere.[62] Extensions to the model we used have been proposed to treat organic semiconductors as layered structures[71] and to treat special cases like blended organic semiconductors.[82,83] We assume a simplified model of charge transfer into the tail states of the organic semiconductor, and we consider the work functions extracted from KPFM to be generally representative of the full electrostatic potential, *V(x)*, as the technique is sensitive to the surface and sub-surface. In our case, a Gaussian model DOS was fitted, which takes the form:

$$g(E) = \frac{N_0}{\sigma\sqrt{2\pi}} \exp\left[-\frac{(E-E_0)^2}{2\sigma^2}\right], \tag{2.8}$$

where N_0 is the integrated state density, σ is the width of the Gaussian DOS and E_0 is the center of the distribution. The Gaussian fit to the DOS has been commonly used,[84,85] but there is still debate whether a Gaussian, exponential or a combination of both is best.[86,87] While no analytical solution is available, E_0 and σ were varied to find a numerical fit to the KPFM data for the MAPLE-deposited P3HT films. The best fit is shown in Figure 2.2, and the corresponding values for the best fit are $E_{0,MAPLE}$=5.5 eV and σ_{MAPLE}=235 meV. This corresponds to the HOMO level of P3HT at the ITO/PEDOT:PSS surface. The KPFM data for the spin-cast P3HT films could not be fit to find the DOS because no band-bending effect is observed for the thicknesses probed. It is not known whether there is no band bending in the spin-casted P3HT films or if the effect is seen at thicknesses less than 5 nm. In previous studies of band bending in conjugated polymer films, very small to no band-bending effect, corresponding to a very narrow DOS, was seen in films that were well-ordered or had high carrier mobilities.[62] Nevertheless, it may be inferred

from our findings that the DOS of the MAPLE-deposited P3HT film is wider than that of the spin-casted P3HT and the effect in MAPLE-deposited samples extends ~20 nm into the film.

Indeed, knowing the width of the DOS of organic semiconductors is prudent as prior work points to the DOS as a key factor, even referring to it as the central quantity,[71] for optimizing energy level alignment at the O/M interface. Since we have seen that the width of the DOS differs between films fabricated by the two techniques, characterization of the two structures is considered. In our previous publications, using a combination of optical and X-ray characterization methods, we showed that the MAPLE-deposited P3HT films possess a higher degree of disorder than their spin-casted counterparts.[15,77] Specifically, MAPLE-deposited samples possess more random orientations of polymer crystallites along the side-chain stacking, π-π stacking and conjugated backbone directions as compared to spin-cast samples. Moreover, the conjugation length distribution, the peak width of (100) side-chain and (010) π-π stacking diffraction peaks are broader in MAPLE-deposited samples, further indicating a higher degree of disorder. With this information, we propose that the more disordered morphology of the MAPLE-deposited P3HT samples leads to greater energetic disorder, resulting in the observed broadening of the DOS as compared to the spin-cast DOS.

To study the implications of the morphology and electronic structure on charge carrier transport, the out-of-plane mobility of MAPLE-deposited and spin-cast P3HT films (h~100 nm) was measured using current extracted by linearly increasing voltage (CELIV) technique. Details of this mobility measurement are listed in the Experimental Section and reported elsewhere.[76] In order to understand the charge transport characteristics of the sample, we examined the electric field dependence of carrier mobility at different temperatures. The results are shown in Figure 2.3a for the MAPLE-deposited sample and in Figure 2.3b for the spin-cast sample. It is evident

that for both samples and at all temperatures, log of the mobility (μ) linearly scales with square root of electric field (E) as $log\mu = log\mu_{E=0} + \beta E^{1/2}$. Second, the slope β decreases with increasing temperature and becomes negative at temperatures above 160 K for both samples. In light of these observations, we reasonably assume that charge transport in the samples reported here can be described using the well-known Gaussian disorder model (GDM) proposed by Bässler.[58] The GDM describes charge hopping through an energy landscape characterized by (1) positional disorder, which originates from variation of intermolecular orientation and distance, and (2) energetic disorder, which originates from statistical distribution of energy states. The GDM proposes the following empirical equation to explain the electric field and temperature dependencies of carrier mobility:

$$\mu(T,E) = \mu_0 e^{-\frac{2}{3}(\frac{\sigma}{kT})^2} e^{C[(\frac{\sigma}{kT})^2 - \Sigma^2]E^{\frac{1}{2}}}. \quad (2.9)$$

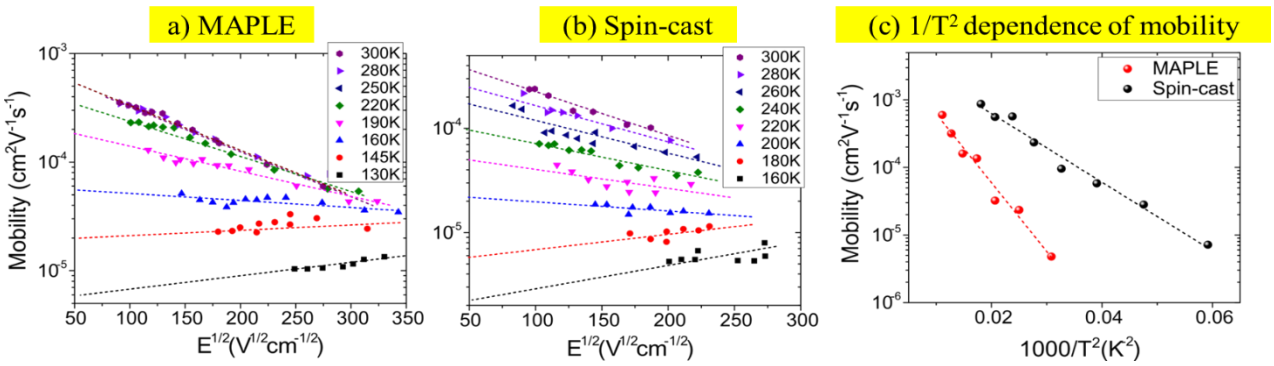

Figure 2.3. Electric field dependence of out-of-plane mobilities at different temperatures for (a) MAPLE-deposited film and (b) spin-cast film. The thickness for the films studied was ~100 nm. (c) Temperature dependence of the mobilities under conditions of field $E = 0$, log $\mu(E=0)$, plotted as a function of $1/T^2$.

Here, σ is the width of the Gaussian DOS, Σ is a parameter that describes the positional disorder, and C is a fitting parameter. To further illustrate the temperature dependence of carrier

mobility, the extracted zero field mobilities (mobility at $E = 0$) are plotted as a function of $1/T^2$ in Figure 2.3c. It is evident that the log of mobility linearly scales with $1/T^2$, in agreement with predictions of the GDM.[74] For all temperatures that were investigated, the zero-field mobility of the MAPLE-deposited sample is always lower than that of the spin-cast sample, consistent with our previous study.[77] Moreover, the slope of the mobility curve in Figure 2.3c is larger in the MAPLE-deposited sample, indicative of a wider DOS according to equation (2.9). Inserting the mobility data into equation (2.9), we find the DOS widths (σ) of the MAPLE and spin-cast sample are 52 meV and 31 meV, respectively. Here, we note that the DOS widths extracted from the GDM and from KPFM measurements are not the same. This is probably because the GDM is not as accurate as some of the newly developed correlated-GDM in which the concept of site correlation is accounted for, leading to different pre-factors for the DOS width.[88–90]

Although examining extended transport models require more sophisticated analysis beyond the scope of this study, we emphasize that based on our transport data, it is clear that the DOS of the MAPLE-deposited sample is wider than the spin-cast sample. This is in excellent agreement with the conclusion from our KPFM measurements. Our findings underpin an important point previously suggested: electronic states that contribute to band bending in conjugated polymers are also those responsible for bulk charge transport.[62] The width of the DOS is thus responsible for the effective carrier mobility, ignoring the high temperature regime.[91] Other studies have also pointed to the importance of the width of the DOS of organic semiconductors, tying its broadening to a decrease in open circuit voltage in organic photovoltaics[92] and to alterations of injection barrier height.[71] Our study illustrates that the width of the DOS can vary in a single conjugated polymer with different morphologies.

2.4 Conclusions

In conclusion, we showed that the band bending in P3HT films on ITO/PEDOT:PSS substrates varies appreciably with the morphology of P3HT. The different morphologies were achieved using two different strategies: MAPLE deposition and conventional spin-casting. A strong band-bending effect was observed in MAPLE-deposited samples in which the work functions of the samples shifted toward the work function of the substrate with decreasing sample thickness, thus indicating charge injection into the tail states of the DOS. No observable band-bending effect was measured in spin-cast P3HT films. Using a model for charge transport into the tail states of the DOS, we ascertained a broader DOS at the HOMO level of the MAPLE-deposited P3HT films than the spin-cast P3HT films, consistent with the disordered morphology of the MAPLE-deposited samples reported in our previous study. The implications of morphology on charge transport were illustrated with temperature- and electric field-dependence studies of out-of-plane mobilities, yielding results suggesting that the electronic states responsible for the band-bending effect in conjugated polymer films are the same as those that dictate bulk transport. The use of KPFM to observe band bending in conjugated polymers on a variety of substrates, which allows for the extraction of the DOS, is particularly relevant now with the latest understanding regarding the significance the DOS of organic semiconductors has on energy level alignment at the O/M interface

Chapter 3: Self-Assembled Monolayers at the Conjugated Polymer/Electrode Interface: Implications for Charge Transport and Band-Bending Behavior

3.1 Introduction

The chemical constituents, electronic structure, morphology, and the highest occupied molecular orbital (HOMO) and lowest unoccupied molecular orbital (LUMO) levels influence the performance of organic semiconductors in various device applications, including solar cells and field-effect transistors.[93–95] Additionally, developing methods to tailor the work functions (WFs) of conductive substrates contribute to an effective design strategy. Reducing the WF of the substrate can improve charge injection at the interface, thereby improving device performance. Surface modification of the conductive substrate is the most common method employed to change the WF of a substrate. For example UV ozone[96] or oxygen plasma[97] surface treatment of indium tin oxide (ITO), commonly used for its transparency and high conductivity

in organic electronic devices, has been used to improve charge injection in devices that rely on ITO substrates.

The addition of a molecular film,[98] surface modifiers,[99] or self-assembled monolayer (SAM)[100–103] has been shown to change the effective WFs (WF_{eff}s) of substrates. A layer of poly(3,4-ethylene dioxythiophene) (PEDOT) doped with poly(styrene sulfonate) (PSS) has been used to reduce the WF (barrier height) at the ITO anode.[104] However, the ITO/PEDOT:PSS interface has, unfortunately, been shown not to be stable.[105] The use of self-assembled monolayers (SAMs) to modify the WFs of substrates has proven to be viable for device applications because of the improved durability of the SAMs due to strong adherence to the substrate via chemical bonding.[100,106] Whether the new effective work function of the SAM-modified substrate, WF_{eff}, engenders the same behavior as a substrate with an equivalent WF is unclear, as shifts in WF_{eff} were sometimes observed to not result in the expected shift in the organic semiconductor energy levels.[107] Because the utilization of solution-based SAMs to modify the substrate WF is procedurally-simple and cost-effective, greater understanding of how precisely the SAM influences energy level alignment and carrier transport properties at the organic semiconductor (O)/conductor (metal – M) interface is warranted.

Although it is known that the addition of a SAM to a substrate can increase or decrease its WF_{eff}, the overall effect on the electronic properties at the O/M interface is not well understood. For instance, the interfacial interaction between the substrate and the organic semiconductor is necessarily changed in the presence of the typically highly polar SAM. With regard to the overall device performance, the additional role that the morphology of the organic semiconductor has in affecting the in- and out-of-plane carrier mobilities within the organic semiconductor is important. In supported thin film organic semiconductors, structurally

disordered by nature, the charge transfer at the O/M interface can be strongly influenced by the morphology – we showed how different fabrication methods enabling different morphologies can be achieved.[66] Moreover, poly(3-hexylthiophene) (P3HT), supported by ITO/PEDOT:PSS substrates, exhibited varied out-of-plane carrier mobilities (μ) because of the fact that μ is sensitive to details of the morphology. The extent of the influence of the morphology on carrier transport is significant, as band bending was observed. Specifically, the HOMO and LUMO levels of organic semiconducting polymer shift as charge is transferred from the electrode at the O/M interface upon contact, as the Fermi levels of the two materials to equilibrate. It is noteworthy that the P3HT films with more-disordered morphologies – increased paracrystallinity in the π-π stacking directions and increased distribution of crystallite (aggregate) orientation distributions – exhibited more band-bending behavior, extending tens of nanometers into the films, as well as slower out-of-plane carrier mobilities. The extent of band bending due to the morphology is more significant than that previously anticipated, as it was comparable to that observed in semiconducting polymers of very different chemistries. Our findings were rationalized within the framework of the Gaussian disorder model (GDM), which describes the behavior of charge carriers migrating throughout a landscape characterized by energetic disorder and structural disorder. The structural disorder naturally originates from the disordered, amorphous and crystalline phases, of the sample and the energetic disorder from the fact that the charged carriers interact with an environment in which the local polarization fluctuates spatially and randomly.

In this study, the influence of two different SAM-modified substrates, trichloro (1H, 1H, 2H, 2H-perfluorooctyl)-silane (FTS)/ITO and octadecyltrichlorosilane (OTS)/ITO, on the electronic properties, specifically the band bending effect, of P3HT is investigated. Band

bending is known to be dependent on the WF of the substrate and the electronic structure of the conjugated polymer, so probing the band-bending behavior of P3HT on substrates with SAMs enables a better understanding if the WF_{eff} of the SAM/ITO is alone responsible for the band bending observed or if the SAM also impacts the electronic structure of P3HT. Two distinct morphologies of P3HT are studied: (1) that arising from typical spin-casting from dichlorobenzene (DCB) and (2) that fabricated using matrix-assisted pulsed laser evaporation (MAPLE), a technique used for depositing conjugated polymer films for a number of applications, including organic photovoltaics (OPVs) and thin-film transistors, among others.[15,66,75,77,108–117] Although the role of the morphology on band bending is now understood in this system, it would be important to gain insight into the combined effect of morphology and interfacial SAMs (SAMs modify the interfacial interactions and WFs) on band bending. What effect would interfacial SAMs have on transport and charge transfer at the interface under these circumstances? Our prior research showed that in-plane carrier transport in MAPLE-deposited films on OTS treated silicon substrates,[77,115] is superior to those of non-treated substrates. However, the out-of-plane transport is yet to be investigated; it would be necessary to know this information in order to develop a better understanding of the carrier transport characteristics. Such an understanding would enable the design of more versatile organic electronic devices. To this end, the combined effects of morphology, achieved using different fabrication methods, and interfacial modification using SAMs on are investigated to understand: (1) the strength of band bending, as determined by the depth into the film the behavior extends; (2) the width of the density of states (DOS) distribution, and (3) the out-of-plane carrier transport across the bulk of the films are presented.

Our findings reveal that the degree of band bending in the P3HT/SAM/ITO system may not be understood solely in terms of the SAM-engendered shift of the WF of ITO. The MAPLE-deposited films, which are more disordered and possess broader DOSs, exhibited stronger degrees of band bending than the spin-cast films supported by the same SAM/ITO substrates. Notably, though the degree of band bending in P3HT/OTS/ITO was smaller than that of P3HT/ITO, OTS/ITO has a larger WF_{eff} than bare ITO. In light of this, the additional role of the SAMs beyond modification of the WF was implicated.

3.2 Experimental Section

3.2.1 Conjugated Polymer Film Preparation: Spin-Cast and MAPLE-Deposited Samples

All substrates of ITO/glass were cleaned via ultrasonication in Alconox detergent solution, deionized water, acetone, hot Hellmanex solution, and 2-propanol for 5 min each, followed by UV-ozone treatment for 20 min. SAMs, either octadecyltricholosilane (OTS) (Gelest Inc.) or trichloro (1*H*,1*H*,2*H*,2*H*-perfluorooctyl)silane (FTS), were prepared on the cleaned substrates in a nitrogen glovebox environment. OTS was formed by immersing substrates in a mixture of OTS and hexadecane (1:250 by volume) for 14 h while stirring. FTS deposition was carried out in the vapor phase by placing substrates in a closed vessel together with 200 µL FTS in a small glass container and heating to 150 °C for 2 h.[118,119] The chemical structures for OTS and FTS are shown in Appendix B. Details of the characterization and quality of the SAMs, including dipole moment calculations, are also included in Appendix B. It is noted that the quality of the SAMs on ITO, despite the roughness of the substrate, is high.

Solutions of P3HT (Reike Metal, ~95% regioregular, M_w = 50,000 g/mol) were prepared by dissolving P3HT in 1,2-dichlorobenzene (DCB) and shaken overnight prior to filtering with a 0.45 µm filter. For spin-cast films, the filtered P3HT solution was spin-casted onto the OTS- or FTS-treated substrates at 600 rpm for 2 min. Specifically, for the FTS-treated substrates, the P3HT solution was allowed to rest on the substrate for 15 s prior to spinning because of the very low surface energy of the substrates.

MAPLE deposition (PVD products) was performed with a system containing a Er:YAG laser (Quantel) of 2.94 µm wavelength. The P3HT solutions in DCB were mixed with benzyl alcohol and DI water containing 0.0005 wt % dodecyl sulfate surfactant at a ratio of 1:0.3:3. An emulsion, based on a previous approach,[75] was created by ultrasonicating the mixture until visibly homogeneous. The emulsion was placed into a liquid nitrogen-cooled (-170 °C) target cup, and the ITO and SAM/ITO substrates were placed 5.5 cm above the target cup. The entire chamber was pumped down to high vacuum (< 2 x 10^{-5} Torr). During deposition, both the target cup and substrates were constantly rotated, and the laser fluence incident on the frozen emulsion was kept at ~1.3 J/cm^2 at a repetition rate of 5 Hz while rastering across the surface. Varying deposition times (typically 5, 30 min, 1, 3, 5, 8 hr) were chosen to achieve different thicknesses of the P3HT films, which were confirmed using atomic force microscopy (AFM) and spectroscopic ellipsometry.

3.2.2 WFs Measured via Kelvin Probe Force Microscopy (KPFM) and Surface Topography Measured with Atomic Force Microscopy (AFM)

Topography and the WFs of spin-cast and MAPLE-deposited P3HT films were both measured with an Asylum Research MFP-3D stand-alone AFM in intermittent contact mode. Surface topography was measured using a CT300 probe (Aspire) with a spring constant of ~40

N/m and a resonant frequency of ~300 kHz. Kelvin probe force microscopy (KPFM) measurements were performed using Pt-coated Si probes (Nanosensors) with a spring constant of ~0.5-1 N/m and resonant frequency of ~75 kHz.

KPFM is a double-pass technique, with the first pass measuring topography of the sample while the tip is driven at its first harmonic resonance frequency. During the second pass, the tip follows the same path as the first and an ac bias at the first harmonic is applied to the tip to generate oscillating electrical forces between the tip and sample. The tip is lifted to a set height ("nap height") between 10 and 20 nm, and the mechanical oscillations of the tip are set to zero. Under these conditions, the surface potential between the tip and sample can be extracted, which can be then used to find the WF of the sample after calibrating the tip. This relation is shown in equation (3.1),

$$V_{CPD} = \frac{\varphi_{tip} - \varphi_{sample}}{-e} \quad (3.1),$$

where V_{CPD} is the surface potential, or contact potential difference, ϕ_{tip} is the WF of the tip, ϕ_{sample} is the WF of the sample, and e is the elementary charge. ϕ_{tip} can be found by calibrating the tip on a surface with a well-known WF, like highly ordered pyrolytic graphite (HOPG) (WF=4.6 eV).

WFs of the spin-cast and MAPLE-deposited samples at varying thicknesses on varying substrates were recorded to reveal the band bending effect in these samples. More details regarding KPFM may be found in the Chapter 2 – Experimental Section, Appendix A, and elsewhere.[81,120]

3.2.3 Surface Energy Measurements of Substrates

Surface energies of substrates were calculated by measuring static contact angles of two liquids, one with purely dispersive (or nonpolar) and one with a combination of dispersive and

non-dispersive (or polar) contributions to the surface tension, using a contact angle goniometer (ramé-Hart 200 F1). The liquids chosen were hexadecane (purely dispersive) and water (dispersive and non-dispersive), which both have well-known surface tension components. Contact angle measurements were repeated five times for each liquid at various positions on the substrates to account for local variations. Fowkes theory[121] was applied to determine the surface energy of the substrate, as shown in equation (3.2),

$$(\sigma_L^D)^{1/2}(\sigma_S^D)^{1/2} + (\sigma_L^P)^{1/2}(\sigma_S^P)^{1/2} = \frac{\sigma_L(cos\theta+1)}{2} \quad (3.2),$$

where σ^D_L is the dispersive surface tension component of a liquid, σ^D_S is the dispersive surface energy component of the solid substrate, σ^P_L is the polar surface tension component of the liquid, σ^P_S is the polar surface energy of the solid substrate, and σ_L is the total surface tension of the liquid. By testing first a liquid with purely dispersive surface tension (i.e. σ^P_L=0 so that $\sigma^D_L = \sigma_L$), the dispersive component of the substrate's surface energy can be solved. This allows for the polar component of the substrate's surface energy to be found when a liquid with both polar and dispersive surface tension components is used. The overall surface energy of the solid substrate was then calculated as the sum of these two components.

3.3 Results and Discussion

Charge transfer into the tail states of an organic semiconductor is responsible for band bending at the O/M interface upon energy level alignment. This effect may be quantified using KPFM. Charge transfer was investigated in films prepared using spin-casting and MAPLE deposition on bare ITO, ITO modified with a FTS monolayer (FTS/ITO), and ITO modified with an OTS monolayer (OTS/ITO). Charge transfer, and thus band bending, at the O/M interface investigated via KPFM measurements of two morphologies of P3HT on various substrates is

shown in Figure 3.1. Each data point in this figure corresponds to the WF of the P3HT film at a certain thickness, with h=0 denoting the WF (or WF_{eff}) of the substrate. The WFs of P3HT films were determined by measuring several areas across the sample surface with KPFM in order to identify an area representative of the sample for measurement. Additionally, in the thinnest films measured that did not correspond to completely continuous films, the surface potential maps were masked to exclude the substrate surface potential in order to ensure only the contributions to surface potential from the films were included. The error bars due to WF fluctuations in the representative areas were found to be smaller than the data points and were therefore not included in Figures 3.1 and 3.2.

It is evident from Figure 3.1 that band bending extends ~20 nm into the film in all MAPLE-deposited P3HT samples. This degree of band bending is larger than that which occurs in spin-cast P3HT films. In these spin-cast films, the band-bending effect in P3HT/FTS/ITO and P3HT/ITO occurs over a small thickness range, less than 10 nm into the film. This small

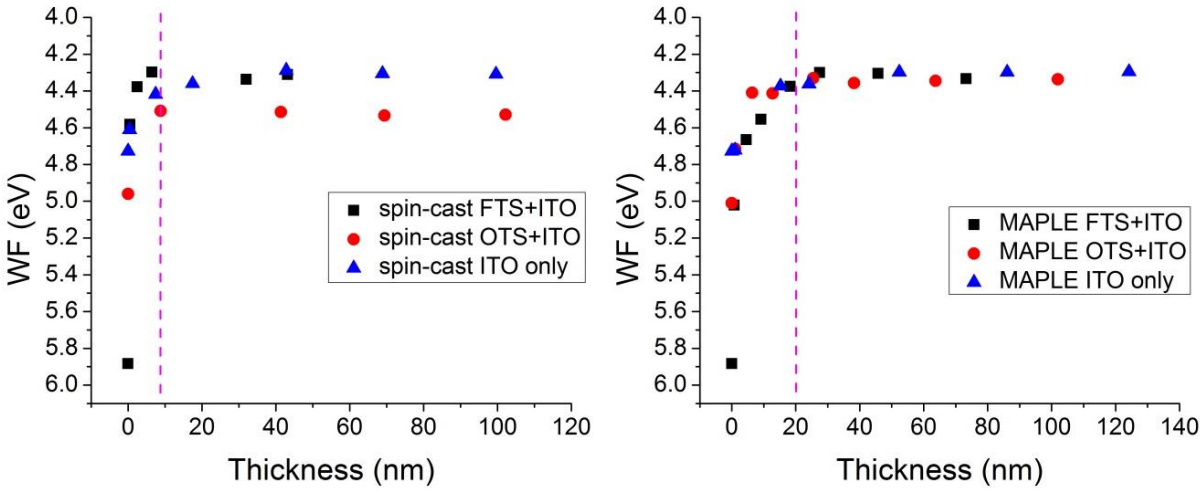

Figure 3.1. Measurements of the WF as a function of film thickness, manifesting band-bending behavior of spin-cast P3HT films (left) and MAPLE-deposited films (right) on several substrates, are shown here. The band-bending effect is seen to extend farther into the MAPLE-deposited films (~20 nm) than the spin-cast films (~10 nm). The pink dashed lines are guides to the eyes showing roughly where band-bending behavior is noted in these films. Error bars for each point are contained within the points and are thus not shown.

thickness range over which band bending extends points to a notable difficulty in using KPFM to determine band bending in all samples. In these cases, very few if any samples are within this small thickness range, so care had to be taken to ensure that the data points within this window are representative of the system. No band bending was observed for the spin-cast P3HT supported by OTS/ITO, not unlike similar observations in the P3HT/PEDOT:PSS/ITO samples previously investigated.[66] Weak band bending, or that extending a short distance (<10 nm) into the film, or no observable band bending has previously been attributed to well-ordered or high carrier mobility films.[62] The discrepancy between the strong and weak band bending extending into the MAPLE-deposited and spin-cast films, respectively, is likely due to local morphological structure, because there are no other intrinsic differences between the two samples. This is consistent with prior studies illustrating morphological differences between the spin-cast and MAPLE-deposited P3HT films, with MAPLE-deposited films possessing a greater degree of disorder than spin-cast films.[15,77,122] The results in Figure 3.1 reveal that across a range of substrates with varied WF and WF_{eff}s, the disordered morphology of MAPLE-deposited P3HT films consistently leads to a stronger measurable band bending effect than that discernible in the more well-ordered spin-cast P3HT films. While this is not necessarily surprising, this finding shows that film fabrication via MAPLE regardless of substrate choice or substrate modification consistently exhibits a stronger degree of band bending than its spin-cast analogues, a point not known prior to this study.

To further quantify the strength of the band bending observed in the MAPLE-deposited samples and assess finer differences between the substrates that were investigated, the following equation (3.3) describing the charge carrier density $n(x)$ at a distance x from the O/M interface was used to fit the KPFM data to extract the DOS $g(E)$,

$$n(x) = \int_{-\infty}^{\infty} \frac{1}{1+\exp[\frac{E-E_F}{k_B T}]} g[E + eV(x)]dE \quad (3.3),$$

where E is the energy, E_F is the equilibrium Fermi energy level, k_B is the Boltzmann constant, T is the temperature, and $V(x)$ is the electrostatic potential at a distance x from the O/M interface. This equation describes a spatially inhomogeneous charge distribution. The function $g(E)$ is

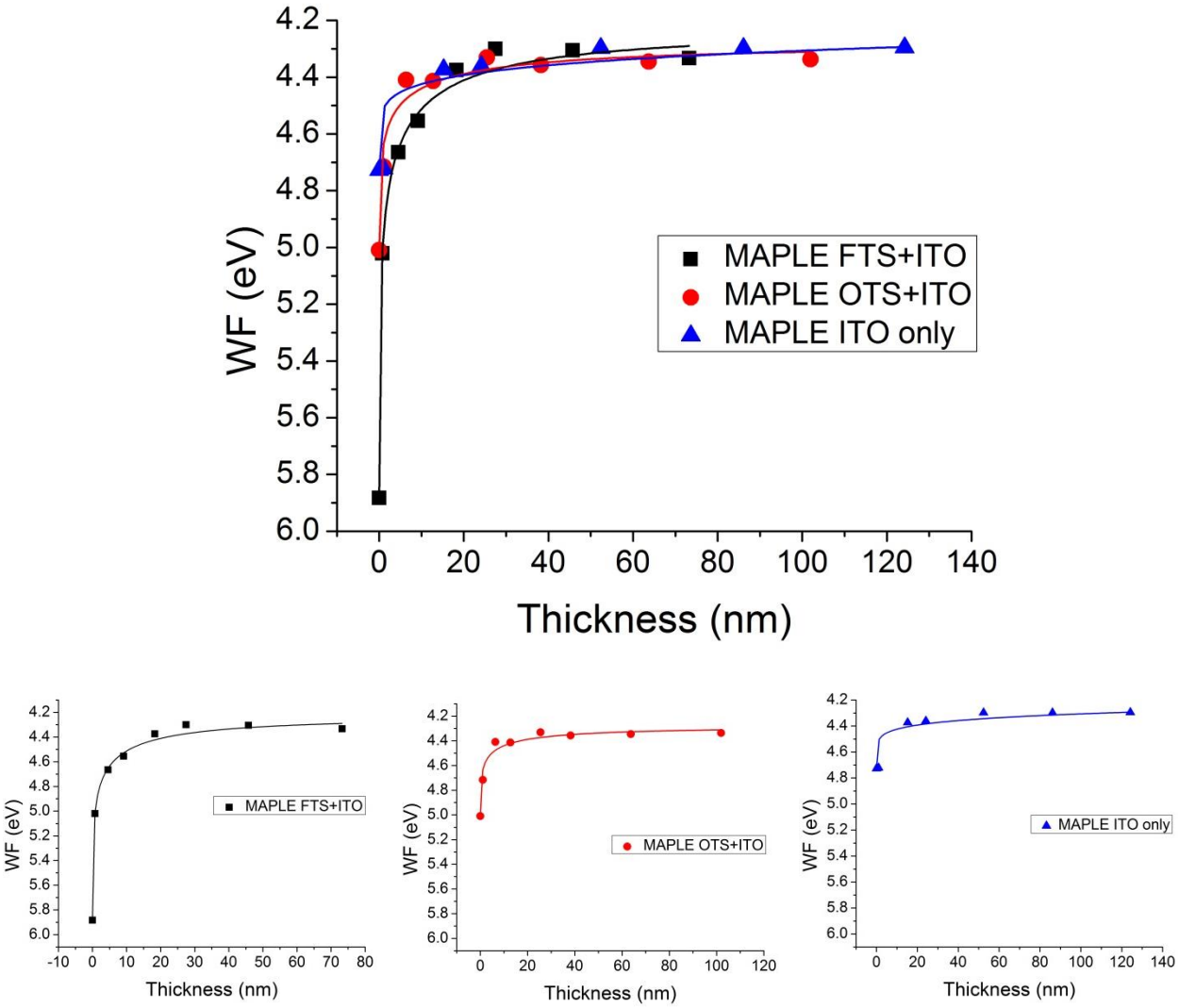

Figure 3.2. Numerical fits to the band bending of MAPLE-deposited P3HT on FTS/ITO, OTS/ITO, and bare ITO substrates shown together (above) and separately (below). Error bars for each data point are contained within the points and are thus not shown. The extracted Gaussian DOS widths are largest for the films on FTS/ITO (311-267 meV), followed by bare ITO (209-177 meV), and OTS/ITO (160-142 meV).

assumed to be Gaussian,[87] and the center of the Gaussian distribution and the Gaussian DOS were varied to find the best numerical fit. The best fits to the KPFM data are shown in Figure 3.2. Further details for this fitting may be found elsewhere.[62,66]

The ranges of values for the Gaussian DOS widths for the MAPLE-deposited P3HT samples on bare ITO, OTS/ITO, and FTS/ITO are 209-177, 160-142, and 311-267 meV,

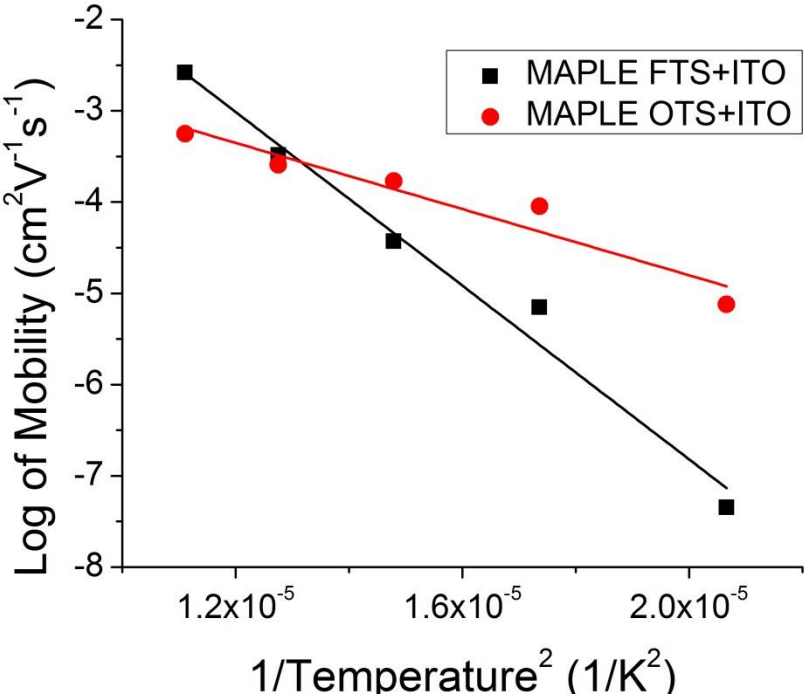

Figure 3.3. Zero-electric field mobilities across a range of temperatures for MAPLE-deposited P3HT films atop FTS/ITO and OTS/ITO. Error bars for each data point are contained within the points and are thus not shown.

respectively. The ranges of values are found by varying the numerical fit to the data points. To be complete, fits for the Gaussian DOS widths for the spin-cast samples on a range of substrates were also attempted (Appendix C). Though the band bending effect is notably less pronounced in the spin-cast P3HT films, the ranges of values for the Gaussian DOS widths for the spin-cast samples on bare ITO and FTS/ITO were found to 80-50 and 80-70 meV, respectively. It should

be noted that the data on OTS/ITO could not be fit because no band bending was observed at the film thicknesses probed.

Because the degree of band bending differs between the P3HT/OTS/ITO and P3HT/FTS/ITO systems, it would be important to understand the impact on the P3HT film carrier mobilities in these systems containing an interfacial SAM. To this end, the out-of-plane mobilities of the MAPLE-deposited films (~100 nm) on OTS/ITO and FTS/ITO were measured using current extracted using linearly increasing voltage (CELIV). More information regarding the CELIV procedure and the raw data extracted from CELIV may be found in Chapter 2 – Experimental Section and Appendix D. It is apparent when comparing the CELIV data of P3HT/FTS/ITO and P3HT/OTS/ITO that the slopes of the zero-electric field mobilities, over a range of temperatures, were significantly different. Notably, the slope of the MAPLE-deposited films on FTS-modified ITO is comparatively large, revealing a wide variation of zero-field mobilities with temperature (Figure 3.3). This finding underscores the notion that the effect of interfacial SAMs can extend well beyond the interface and influence out-of-plane mobility and the variation of that mobility with temperature.

The slopes of the zero-electric field dependencies of the mobilities over a range of temperatures may also be used to extract the width of the Gaussian DOS using the well-known GDM mentioned previously.[58] The linear dependence of $\log\mu$ on $E^{(1/2)}$, such that $\log\mu = \log\mu_{E=0} + \beta E^{1/2}$ where μ is the mobility and E is the electric field, shown in Figure 3.3, suggests that the model provides an appropriate description of the behavior of this system. The width of the DOS determined for the MAPLE-deposited P3HT on OTS/ITO is less than that of the film on FTS/ITO ($\sigma_{P3HT/OTS/ITO} \approx 68$ meV vs $\sigma_{P3HT/FTS/ITO} \approx 110$ meV); this is consistent with the trends of the DOS widths measured using KPFM and serves as a useful check on the DOS widths

extracted using KPFM. It is noted that the numerical DOS values extracted from the CELIV data differ from those extracted from KPFM data. This is because a simplified GDM equation that does not account for correlations between hops or other complexities.

The differences between the DOSs of the MAPLE-deposited films, measured with KPFM and CELIV, suggest a substrate-related effect. There is a range of values of WFs, or WF_{eff}s, for the substrates investigated: 4.73 eV for bare ITO, 5.0 eV for OTS-modified ITO and 5.88 eV for FTS-modified ITO. Recall that the degree of band bending depends on the differences between

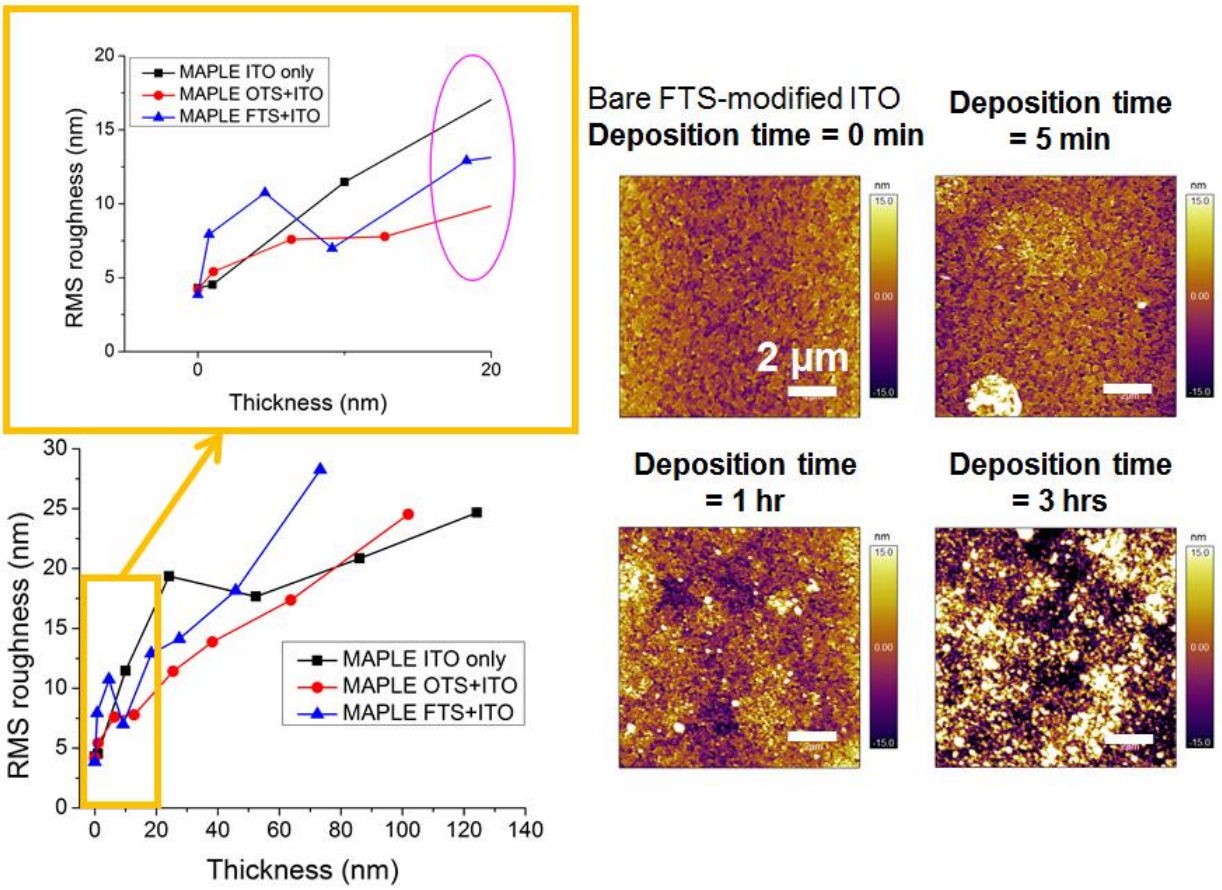

Figure 3.4. rms roughness versus thickness for MAPLE-deposited films on several substrates. Inset shows the rms roughness range from 0-20 nm, the extension of the band-bending effect in these films, with a pink circle around the rms roughnesses for each film at ~20 nm film thickness. Error bars for each roughness data point are contained within the point and are thus not included in the plot. AFM topography images (right) (all same scale as shown with 2 µm scale bar) are shown for MAPLE-deposited films on FTS/ITO to show the progression of topography with deposition time.

WFs.[62] Interestingly, the DOS widths of the films do not directly scale with the changes to WF or WF_{eff}, as it is observed that P3HT/OTS/ITO samples exhibited the narrowest DOSs. As noted earlier, a potential contributor to the increase in energetic disorder responsible for a wider DOS arises from an increase of structural disorder. This was evident by comparing DOS widths of MAPLE-deposited and spin-cast P3HT films on ITO/PEDOT:PSS substrates.[66]

In order to understand differences between morphologies of thin films on various substrates, the surface topographies of MAPLE-deposited films of several thicknesses were measured using AFM. It is well known that MAPLE-deposited films have more disordered morphological structures than spin-casted films; MAPLE-deposited films also have topographies with larger root mean square (rms) roughnesses as determined by AFM. The topographical scans of the MAPLE-deposited films on FTS/ITO substrates (shown as an example) and plots of rms roughness as a function of thickness for all of the MAPLE-deposited films are shown in Figure 3.4. It is evident from Figure 3.4 that the exact values for rms roughnesses for the films are not the same for P3HT films across all substrates, and there exists a minor spread in the RMS roughnesses measured for all of the samples. However, there are observations that can be made by examining the data in Figure 3.4. The rms roughness of the MAPLE-deposited films on bare ITO at a thickness of ~20 nm, which corresponds to the thickness at which the band-bending effect is observed in these MAPLE-deposited samples, is notably the most pronounced (rms roughness ~ 19 nm). This rms roughness is large, but as seen in Figure 3.4, the rms roughness values below film thicknesses of ~20 nm are all somewhat similar to the actual thickness of the "films". This suggests a mechanism of MAPLE film formation, which does not provide thin uniform films. Our previous studies have shown that a fully continuous film develops on the surface when a film of average thickness of ~20-25 nm is deposited (approximately ~60 min of

deposition).[115] Prior to this time, patchy globular islands of polymer are deposited on the substrate surface, and these islands begin to coalesce as deposition time increases. After a continuous film is formed, rms roughness values of the MAPLE-deposited films generally all increase with thickness, which is consistent with our previous reports.[115]

For the MAPLE-deposited films on bare ITO and FTS/ITO the rms roughness values for a film of thickness ~20 nm are ~17 and ~13 nm, respectively. These values are both higher than the rms roughness value of the ~20 nm film on OTS/ITO, which is approximately ~9 nm. These numbers reveal a possible effect of the substrate on which the globular islands form. When comparing the trends of DOS widths with the trends observed in roughnesses for thin (~20 nm) MAPLE-deposited films, it is observed that, in general, larger roughnesses are associated with wider DOSs, and the smaller roughness of the thin film on the OTS/ITO substrate matches with the narrowest DOS. The rougher thin films on both the bare ITO and FTS/ITO could signify an increase in morphological disorder, which is associated with wider DOSs. Moreover, it has been previously shown that for OTS-modified Si substrates, highly oriented interfacial P3HT crystals form with sizes larger than those on oxidized Si substrates.[115] On the basis of the mechanism of formation of the MAPLE-deposited films, the rms measurements point to potential differences in the morphologies of the thin films. Because of the mechanism by which the MAPLE deposited films are formed – deposition of globules on a substrate – the rms can serve as a crude manifestation of disorder, with larger rms values associated with more structural disorder. Increased structural disorder is responsible for broader DOSs.

For these reasons it is unsurprising that the correlation between rms roughnesses and the DOS widths would not be perfect; the ~20 nm MAPLE-deposited film on ITO has a larger rms roughness than the ~20 nm MAPLE-deposited film on FTS/ITO, though it is the films on

FTS/ITO that possess the widest DOSs of the three substrate conditions tested. Having noted this point, it is compelling to also consider that the uncertainty of the correlation between rms roughness and the width of the DOS of the MAPLE-deposited films supported by FTS/ITO and bare ITO could be reconciled by the fact that band bending depends on both the electronic structure of the conjugated polymer, affected by structural disorder, *and* the WFs of the substrate and the polymer. The DOS width is extracted from the band-bending data. In attempting to correlate the rms roughness of thin MAPLE-deposited films with the DOS widths, only the influence of morphological disorder on the electronic structure of the conjugated polymer is considered. Our prior studies have implicated morphological disorder as strongly influencing band bending behavior (carrier transport is also changed appreciably), but it is recognized that the WFs of the FTS/ITO and bare ITO substrates are distinctly different, which further contributes to band bending.

While the thin-film trends of surface roughness seem to be generally related to the DOS widths measured with KPFM, the question of what leads to the change to surface roughness, and consequently film structure, remains. The mechanism of film formation in MAPLE-deposited films is responsible for larger rms roughnesses as compared to those of spin-cast films, but the variation of rms roughnesses in MAPLE-deposited thin films may be related to the substrate. To investigate this further, the surface energies of various substrates were measured using a contact angle goniometer. The surface energy was extracted using Fowkes' theory, which requires contact angle measurement using two liquids, one with purely dispersive surface tension and one with both dispersive and polar surface tension components. The surface energies of the substrates are shown in Table 3.1, which reveals the MAPLE-deposited films with the higher peak rms roughness values correspondingly have the lower substrate surface energies. These substrate

surface energies can be compared with the DOS widths, as seen in Table 3.1, and a trend with lower surface energies of substrates associated with wider DOS values for films on such substrates is observed. This trend highlights a key finding: substrate surface energy influences MAPLE-deposited thin film morphology which impacts the P3HT DOS widths measured by KFPM and CELIV.

Substrate	DOS width ranges (meV)	rms roughness of ~20 nm film (nm)	Surface energy (mJ/m^2)
FTS/ITO	311-267	~13	14.76 ± 0.75
Bare ITO	209-177	~17	22.19 ± 2.25
OTS/ITO	160-142	~9	25.51 ± 0.40

Table 3.1. Values of DOS width and peak RMS roughness in thin MAPLE-deposited films and surface energy of substrates.

In fact, drastic changes to the morphology of organic material dependent on the surface energy of its substrate has been previously recorded.[123] In this case, the pentacene grain size was notably reduced when deposited on low surface energy substrates. It should be noted that in this case the decrease to grain size did not necessarily mean a detriment to device performance behavior. In fact, it was found that the smaller grains deposited on the low surface energy substrate led to higher in-plane carrier mobilities of a fabricated transistor than when using pentacene deposited on a higher surface energy substrate. Unfortunately, out-of-plane mobility and DOS width were not provided in this study, but these results indicate the complexity of the problem at hand. The effect of morphology on in- versus out-of-plane carrier mobility is not always the same.[77] Furthermore, crystallization mechanisms between conjugated polymer and

small molecule films may differ, meaning that the effect of the substrate surface energy on crystallite formation may necessarily differ as well.

The proposed crystallization schematic for the behavior observed in this present study is shown in Figure 3.5. This schematic builds on the idea presented in the pentacene study,[123] in which larger crystals grow on substrates with higher surface energies (i.e. OTS/ITO) and smaller crystals grow on substrates with lower surface energies (i.e. FTS/ITO). Building on our group's

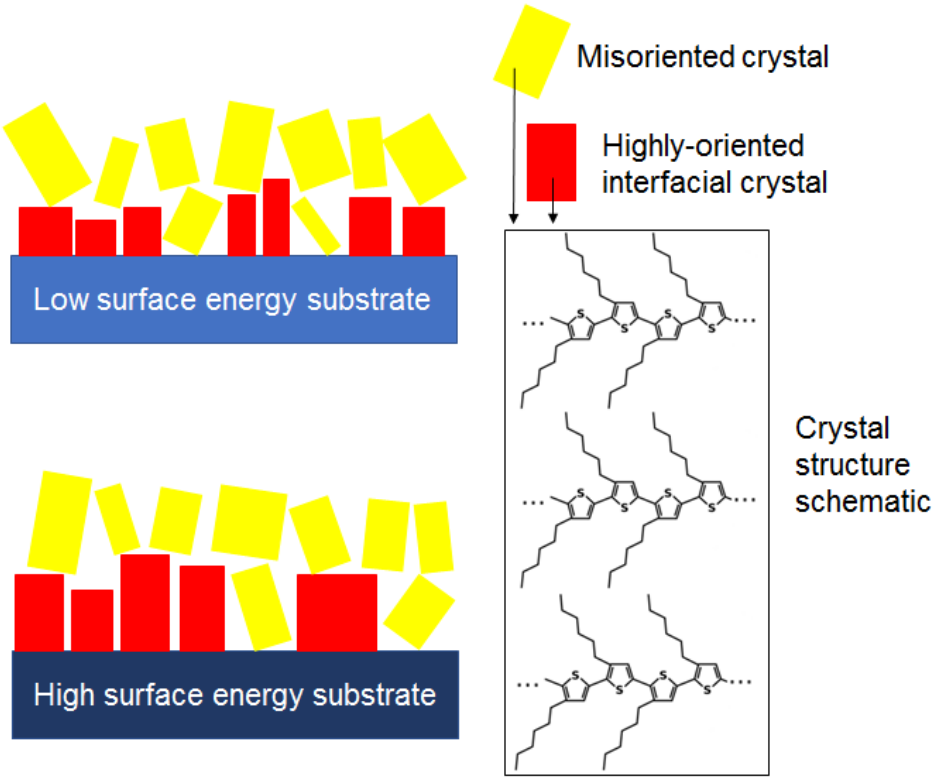

Figure 3.5. Crystallization schematic for MAPLE-deposited films on high and low surface energy substrates.

previous study of the MAPLE crystallization mechanism,[115] these interfacial crystals, regardless of specific substrate chemistry, are more highly oriented than those growing from the bulk, which tend to be more misoriented. The highly-oriented crystallites primarily stack in the edge-on configuration with polymer side chains oriented in the out-of-plane direction and π-π stacking

in the in-plane direction. In our case, then, the highly-oriented interfacial crystals grown on OTS/ITO are larger than those on FTS/ITO, because the surface energy of OTS/ITO is larger than that of FTS/ITO. This provides a further explanation for the improvement to in-plane mobilities[77,115] exhibited by OTS-modified substrates in other studies.

The effect of the interfacial interaction on the DOS width of the MAPLE-deposited films is now discussed. As the width of the DOS of organic semiconductors has implications for open circuit voltage in OPVs[92] and barrier injection height,[71] the wide variation of DOS width for the MAPLE-deposited P3HT reported here has potential implications for device performance. The DOS width of a conjugated polymer changes with the morphological structure of the polymer, and these morphological changes are influenced by SAMs, which alter the interfacial interaction between the conjugated polymer and the substrate.

3.4 Conclusions

This study showed that P3HT/SAM/ITO devices exhibit a range of electronic properties, different from those of P3HT/ITO devices, because of variations in the morphological structure of P3HT. SAMs not only alter the WF of ITO, but also they modify the surface energy of ITO. By virtue of the manner in which the P3HT films were deposited (solution spin-cast and MAPLE deposition) onto the SAM/ITO substrates, their morphologies varied, manifesting effects of the surface energy differences between ITO, FTS/ITO, and OTS/ITO substrates. Therefore, devices with varying P3HT morphologies, with the same WF differences between P3HT and the substrates, enabled new insights into the combined role of WF differences and morphological disorder of the organic semiconductor on the electronic properties of these devices.

The following is now evident. Regardless of the substrate, MAPLE-deposited P3HT films exhibited stronger band-bending behavior than the spin-cast P3HT films on the same substrate. This is because these P3HT films are more structurally disordered, with an associated broader distribution of DOSs. Additionally, the DOS widths of the MAPLE-deposited films, extracted from the band-bending data, were larger on substrates with lower surface energies (FTS/ITO) than those deposited on substrates with higher surface energies (OTS/ITO). This is because more structurally disordered films were formed on substrates with lower surface energies.

Chapter 4: Solvent Annealing: Post-Processing Unique Morphologies of Conjugated Polymers and Bismuth-Based Perovskites

The use of post-processing solvent annealing to create more stable and improved morphologies of both organic and inorganic films has been successfully demonstrated in both a conjugated polymer [poly(3-hexythiophene) (P3HT)] and a lead-free, bismuth-based hybrid perovskite [methylammonium bismuth iodide (MBI)]. In addition to the creation of unique morphologies, enhancements to electronic properties in both P3HT and MBI films have been observed. The implications of the post-processed morphologies on properties is discussed in the following subchapters.

4.1 Band-Bending Behavior of Solvent-Annealed Conjugated Polymer Films

Unpublished data from Wenderott, J. K.

4.1.1 Introduction

Precise control of the nanostructure of organic materials using low-cost, scalable, and procedurally-simple fabrication and processing techniques is of great interest for the development of organic electronic devices. In organic materials, both polymers and small molecules, nanoscale structure and long-range order are influential to electronic properties, such

as charge carrier transport, and varying the architecture of organic materials can lead to orders of magnitude changes to such properties.[66,74,77] Conjugated polymer films are typically processed from solution via spin casting or drop casting. In general, the structure of the films following solution casting is dependent on several parameters, including the interaction between all species present: polymer chains, solvent molecules, and substrate surface.[124] Spin-casting produces planar films of reproducible thicknesses, though often stresses can be present in the final films due to the fast solvent evaporation.[125,126]

To alleviate the issue of stresses in as-spin-casted films, a variety of processing conditions after fabrication, so called post-processing, have been implemented to lead to more stable film morphologies. Thermal annealing is an often-utilized post-processing technique in organic materials,[127–129] but there exists a risk of degradation to the organic material and substrate at elevated temperatures. Alternatives to thermal annealing are super critical CO_2 annealing[65] and solvent vapor annealing. In solvent annealing, organic films are subjected to an environment containing solvent vapors, and the vapors can penetrate the film by re-solubilization of the organic material.[130,131] The solvent molecules allow for greater mobility of the organic material, so species such as molecules or polymer chains are able to rearrange into more stable, often more ordered,[132] final structures during the course of annealing.

In this study, solvent annealing as a post-processing tool was utilized to influence the morphology of spin-cast poly(3-hexylthiophene) (P3HT) films. During the spin-casting of P3HT films, the final structures formed are very sensitive to the precise spin speeds and times associated with drying.[133,134] In our lab's experience, sample-to-sample variation in as-cast P3HT films is present, especially in films >20 nm in thickness, further indicating the sensitivity of the structure to spinning conditions and randomized formation of stresses in the films. Investigation

of the as-cast P3HT films spun from two different solvents was performed using Kelvin probe force microscopy (KPFM). KPFM allows for probing of the band-bending behavior of the P3HT films, which we have shown to be influenced by morphology of the polymer film.[66] Bending of the energy bands of the polymer (both the highest occupied molecular orbital (HOMO) and lowest unoccupied molecular orbital (LUMO) levels) results when charge is transferred between the conductive electrode and the semiconducting polymer. More information about band bending can be found in Chapters 1-3. The degree of band bending is dependent on the work function of the substrate and the electronic structure of the polymer, which is sensitive to polymer morphology. The KPFM data reflected the variation in as-cast P3HT film structure, yielding a spread in the P3HT work function at varying thicknesses. After post processing with solvent annealing, this sample-to-sample variation of work function as measured with KPFM was greatly reduced. The band-bending data was further interpreted with modelling to discuss the energetic disorder present in these films. Our results indicate the usefulness of solvent annealing as a simple and effective post-processing tool to lead to more uniform morphologies, and thus electronic properties, of spin-cast P3HT films.

4.1.2 Experimental Section

Materials and Film Preparation

All indium tin oxide (ITO) substrates were cleaned by ultrasonication for 5 minutes each in (1) Alconox® detergent solution, (2) DI water, (3) acetone, (4) hot Hellmanex® solution, and (5) 2-propanol, followed by exposure to UV-ozone for 20 minutes. After the cleaning of ITO, the substrates were coated with a layer of poly(3,4-ethylenediosythiophene): polystyrene sulfonate (PEDOT:PSS). Poly(3-hexylthiophene) (P3HT) (Reike Metal, ~95% regioregularity, M_w = 50,000 g/mol) solutions were prepared by dissolving the polymer in 1,2-dicholorbenzene (DCB)

or chloroform (CF). Solutions mixed overnight before being filtered with 0.45 μm polytetrafluoroethylene (PTFE) filter. Spin-cast films were fabricated by spinning filter solutions of varying concentrations on ITO/PEDOT:PSS substrates at 600 rpm for 2 minutes in a glove box environment. Following spinning, films were directly measured (as-cast) or then placed on a hot plate at 50 °C next to a small amount of CF in an open vial and covered with a glass dish that also enclosed the CF. The films were allowed to remain for 3 hours to complete the solvent annealing of the films, which were then measured.

Band-bending Characterization of Solvent-Annealed and As-Cast Films

Kelvin probe force microscopy (KPFM) measurements were performed using Pt-coated Si probes made by Nanosensors (stiffness ~0.5-1 N/m, resonant frequency ~75 kHz) on an Asylum Research MFP3D atomic force microscope. Most measurements were made in air with 10-30% humidity. KPFM acts as a double-pass, intermittent contact technique. First, the sharp metallic tip raster-scans across the surface of interest, measuring the topography. During the first pass, the cantilever is driven at its first harmonic resonance frequency, and the amplitude of this mechanical oscillation is used as the feedback signal. In the second pass, which follows the same path as the first pass, an AC bias at the first harmonic resonance frequency of the cantilever is applied to the tip that generates oscillating electrical forces between the tip and sample. The mechanical oscillations of the cantilever are set to zero and the tip is lifted to a set height ("lift height"). This distance is between 10-20 nanometers, which captures the electrostatic interactions but remains far removed from short-range VDW forces. A lock-in amplifier is employed to extract the electrical force component with the first harmonic frequency and apply a DC bias until this oscillation is nullified. These oscillations are continually nullified as the tip

follows the second pass, providing a local map of the surface potential. More details for the KPFM technique can be found in Chapter 2 – Experimental Section and Appendix A.

4.1.3 Results and Discussion

The work functions as measured by KPFM of the as-cast P3HT films spun from DCB and CF both prior to and after solvent annealing in CF are shown in Figure 4.1. In this figure, the

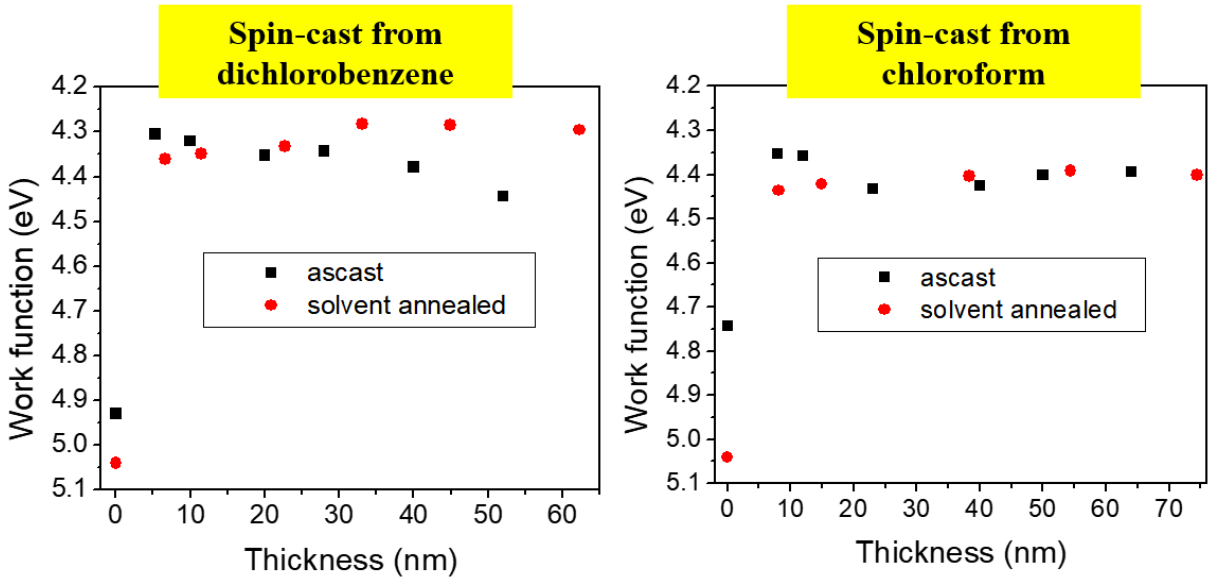

Figure 4.1. Band-bending data of spin-cast P3HT films spun from DCB (left) and CF (right) before (black) and after solvent annealing in CF (red).

thickness *h=0* corresponds to the work function of the ITO/PEDOT:PSS substrate, which interestingly enough also shows a change to its value upon solvent annealing, perhaps owing to some change to the PEDOT:PSS layer. In both solvent-annealed film data sets, the work function values of the P3HT films appear to level off at consistent values at thicknesses greater than 20 nm for films spun from DCB and 10 nm for films spun from CF. In both data sets, there appears to be a slight signature of bending of the work function values of the polymer toward that of the substrate in the thinnest P3HT films, but it is clearly less pronounced than band bending of film

morphologies fabricated from matrix-assisted pulsed laser evaporation (MAPLE), as shown in Chapters 2 and 3. As noted from Figure 4.1, the work function of the thinnest solvent-annealed film spun from DCB measured (~5 nm) is only ~50 meV different than the bulk films. In the films spun from CF, this difference is even smaller, about ~10-20 meV.

It should be noted that the band-bending data of as-cast films spun from DCB were previously shown in Chapter 2 as a comparison to the MAPLE-deposited films. In that work, it was concluded that the DOS of the MAPLE-deposited films was wider than that of the spin-cast films, even though the band-bending data of the spin-cast films could not be fit. With more uniform work function values of the spin-cast P3HT films now available after solvent annealing, it is possible to fit the band-bending data to confirm this point. As in Chapters 2 and 3, the band-bending data can be fit to find the DOS using the equation for a spatially inhomogeneous charge distribution:

$$n(x) = \int_{-\infty}^{\infty} \frac{1}{1+\exp[\frac{E-E_F}{k_B T}]} g[E + eV(x)]dE \qquad (4.1)$$

where $n(x)$ is the charge-carrier density at a distance x from the O/M interface, E is the energy, E_F is the equilibrium Fermi energy level, k_B is Boltzmann's constant, T is the temperature, $g(E)$ is the model DOS and $V(x)$ is the electrostatic potential a distance x from the O/M interface. $V(x)$ is given by solving the 1D Poisson's equation using the boundary conditions $V(0)=0$ and $V(\infty) = \phi_{poly.}$ This simplified model assumes charge transfer into the tail states of the P3HT.

The best fits to the band-bending data are shown in Figure 4.2. A Gaussian DOS is assumed, and numerical fitting was applied to yield DOS widths for the two sets of solvent-annealed spin-cast films. For both sets of films, the DOS width range is between 5-30 meV, with a slightly smaller DOS width fitted for the films spin-cast from DCB. These values for the DOS width that correspond to both sets of spin-cast films are clearly smaller than the DOS width

extracted for the MAPLE-deposited sample on ITO/PEDOT:PSS of Chapter 2, which was 235 meV. This further points to the decreased level of energetic disorder in spin-cast P3HT films, as opposed to the MAPLE-deposited films. Furthermore, it is observed that the solvent annealing does not seem to significantly affect the degree of band bending observed, but it does lead to the creation of more uniform P3HT films with more uniform work functions. This is indicative of more well-ordered films. Another indication of the well-ordered spin-cast P3HT films is that the window for band bending is quite small (<10 nm).

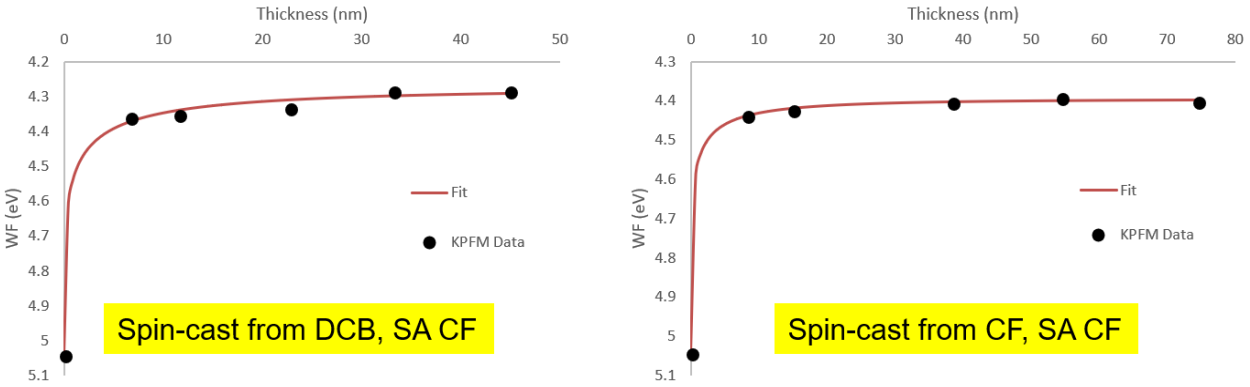

Figure 4.2. Fits to band-bending data of spin-cast P3HT films spun from DCB (left) and CF (right) after solvent annealing in CF. The DOS widths extracted for both sets of films were in the range of 5-30 meV.

4.1.4 Conclusions

In conclusion, we have shown that solvent annealing is a viable tool for post-processing spin-cast P3HT films to lead to more uniform and stable morphologies, especially those of thicknesses <20 nm. This was shown by comparing band-bending behavior of as-cast P3HT films spun from two different solvents to the same films after undergoing solvent annealing for 3 hours. In both cases, solvent annealing lead to stable work function values of the spin-cast P3HT films and revealed very narrow windows into which band bending is observed. The band-

bending data was fit to reveal narrow DOS widths (5-30 meV) for the two data sets. This study underscores the use of solvent annealing as a useful post-processing technique for spin-cast conjugated polymer films, especially to improve film uniformity across a series of samples.

4.2 Local Optoelectronic Characterization of Solvent-Annealed, Lead-Free, Bismuth-Based Perovskite Films

4.2.1 Introduction

Organic-inorganic perovskites (with crystal structure ABX_3, where A is the organic cation, B is the inorganic metal and X is the halogen) have recently gained widespread attention because of their rapidly improving efficiencies,[135] low-temperature solution-based fabrication,[136] tunable band-gap[137] and high absorption coefficients,[138] and long carrier diffusion lengths[139–141] leading to power conversion efficiencies (PCEs) as high as 20%.[142,143] Whereas the high PCE holds potential for significant economic impact, emerging perovskite technology typically use lead (Pb), a toxic element,[144] as the inorganic metallic component. Mixed-metal tin (Sn)-Pb perovskites that allowed the tunability of the band gap indicated Sn as a promising replacement metal[145] but suffered rapid degradation because of the propensity of Sn^{2+} to oxidize to Sn^{4+}, requiring hermetic sealing of devices in an inert atmosphere before exposure to air.[146] Lead

substitutes such as iron (Fe), manganese (Mn) and bismuth (Bi), among others, have been used,[147–151] with great improvement in stability being observed in Bi-based perovskites.

Methylammonium bismuth iodide (MBI), a Bi-based perovskite with the chemical structure $(CH_3NH_3)_3Bi_2I_9$ has been shown to be stable in air for up to ten weeks.[152] MBIs, like many other perovskites, are fabricated using simple, low-temperature solution processes.[152–154] PCEs of devices made with these MBI films, however, usually fall between 0.1 and 0.2%,[152,154] attributed in part to the inconsistent morphology of the thermally annealed films. Solvent annealing, during which solvent vapor is exposed to the material bulk or thin film during crystallization, is an effective technique for improving the crystallinity of organic-inorganic hybrid semiconductors such as organometal halide perovskites.[155–157] It has been proposed that solvent annealing leads to a liquid or quasi-liquid phase on the surface of the perovskite film, which subsequently leads atoms to recrystallize where grains are not close or in contact, thus contributing to improved crystallinity with larger grains being formed.[157] Recently, solvent annealing of MBI films in dimethylformamide (DMF) has been reported to increase crystallite size and PCE of devices,[158] but significant improvement is still needed for these lead-free films to replace perovskites containing lead. Realizing these improvements requires a deeper understanding of how solvent annealing affects the film structure and properties from a nanoscale perspective.

Conductive atomic force microscopy (c-AFM) is an often-utilized technique for simultaneous local mapping of conductivity and topography for inorganic and organic semiconducting films, among other types of samples. c-AFM on perovskite films has been used to compare the conductivity of grains versus grain boundaries (GBs), investigate carrier transport pathways, and establish a correlation between topography and conductivity. In particular,

understanding how carrier transport differs between grains and GBs is of great interest, as currently there is no clear consensus on whether GBs act as a recombination site or as a pathway for carrier transport. Although several researchers have used c-AFM to probe lead-based perovskites,[159] few studies exist in which lead-free perovskites are highlighted. Thus, a detailed study of the effect of solvent annealing on the lead-free perovskite film structure and optoelectronic properties is warranted.

In this study, X-ray diffraction (XRD), scanning electron microscopy (SEM), and cross-sectional SEM were used to clarify structural changes after thermal annealing and annealing with DMF solvent. SEM micrographs showed an increase in the size of hexagonal MBI grains after solvent annealing, and XRD data were used to confirm this semi-qualitatively with the Scherrer equation. Local characterization of lead-free MBI films after thermal annealing and DMF solvent annealing using c-AFM in the dark and under illumination [(photo)c-AFM (pc-AFM)] was also performed. We found larger conductivity and photoconductivity in the MBI film that has undergone DMF annealing than that of the MBI film that has only been thermally annealed, perhaps related to the increase in grain size and crystallinity because of solvent annealing we observe with XRD and SEM. Additionally, we observe that photoconductivity increases primarily within grains of both the solvent-annealed and thermally annealed films, with little change in the photoconductivity at the GBs. This leads to a better understanding of charge transport in lead-free MBI films, which is vital for their successful implementation in devices. The findings of this study implicate the larger grain size, decreased film roughness, and increased crystallinity of MBI films resulting from solvent annealing as key to optoelectronic property enhancement.

4.2.2 Experimental Section

Materials and Device Preparation

All the perovskite precursors, including methylammonium iodide (CH_3NH_3I – MAI) and BiI_3 (purity 99%), poly(3,4-ethylenedioxythiophene):polystyrene sulfonate (PEDOT:PSS), [6,6]-phenyl-C_{61}-butyric acid methyl ester (PCBM), and solvents (purity 99%) were obtained from Sigma-Aldrich and used as received. $MA_3Bi_2I_9$ precursor solution was prepared by mixing MAI and BiI_3 in a molar ratio of 1.5:1 in 1 mL of DMF and stirred overnight at 70 °C. The indium tin oxide (ITO)-coated glass samples (sheet resistance ≤10 Ω/cm^2, Mater Win) were cleaned consecutively in detergent, acetone, isopropanol, and ethanol ultrasonic bath for 15 min each, dried under a nitrogen flow, and treated with UV-ozone for 15 min before use.

PEDOT:PSS/deionized water (v/v = 1/3) solutions produced by sonication and filtering were first spin-coated (Laurell WS-650-Hzb-23b) onto the ITO-coated substrate at 4000 rpm for 50 s and annealed for 20 min at 150 °C. The MBI precursor solutions were then spin-coated onto PEDOT:PSS/ITO/glass substrates at 3000 rpm for 40 s in the sequence (1) BiI3 and (2) MAI. The stacked film was annealed at 100 °C with (solvent-annealed sample) or without (thermally annealed sample) DMF vapor for 15 min. For the devices, following annealing, a PCBM (Sigma-Aldrich) layer was spin-coated at 1000 rpm for 30 s. Silver (Ag) at a thickness of 120 nm was deposited onto the material stack to complete the device preparation.

Characterization of MBI Films

XRD (Bruker DA advanced XRD equipped with Cu Kα radiation at room temperature) was performed at room temperature using graphite monochromatic Cu Kα radiation at a scanning rate of 0.1°/s over the Bragg angle range of 5.0°-70.0° (2θ). The morphologies of the MBI films on PEDOT:PSS/ITO substrates were studied through SEM images obtained using a field-

emission scanning electron microscope with a high tension of 10 kV and magnification of 5k and 10k. Topography and conductivity maps were obtained in the contact mode using an Asylum MFP3D atomic force microscope (AFM) using platinum-iridium (Pt/Ir) coated-Advanced TEC tips (Nanosensors) with a resonance frequency between 7 and 25 kHz and a spring constant between 0.02 and 0.75 N/m. The UV–visible (UV–vis) absorption of the MBI films deposited on PEDOT:PSS/ITO substrates was recorded using a Shimadzu UV–vis spectrophotometer with the signal of the PEDOT:PSS/ITO substrate as the calibration background. Photocurrent density–voltage (J–V) curves of the unsealed devices were measured in air (Hr ≤ 30%) on a Keithley 2400 unit with a sweep speed of 0.02 V/s under AM 1.5G, achieved using the simulator at 100 mW/cm^2, calibrated with a calibrated-Si reference cell. To minimize the influence of device degradation caused by moisture corrosion, J–V characterization was performed immediately after device fabrication.

4.2.3 Results and Discussion

MBI films were fabricated using a facile, low-temperature solution process. The MBI precursor solution was prepared by mixing MAI and BiI_3 in DMF separately. The solutions were then spin-coated in the sequence (1) BiI_3 and (2) MAI. The thin film made from the two-step approach is superior to the film made from the conventional one-step spin-coating method, especially the one made on a PEDOT:PSS/ITO/glass substrate, where the crystallization process of the $MA_3Bi_2I_9$ crystal is fast, leading to non-uniform films with island morphology. It has also been reported in literature that interdiffusion of two layers (BiI_3 and MAI) often leads to more uniform and compact films than those from one-step approaches.[160] The stacked film was annealed with (solvent-annealed sample) or without (thermally annealed sample) DMF vapor as shown in Figure 4.3. Because both precursors (BiI_3 and MAI) have high solubility in DMF,

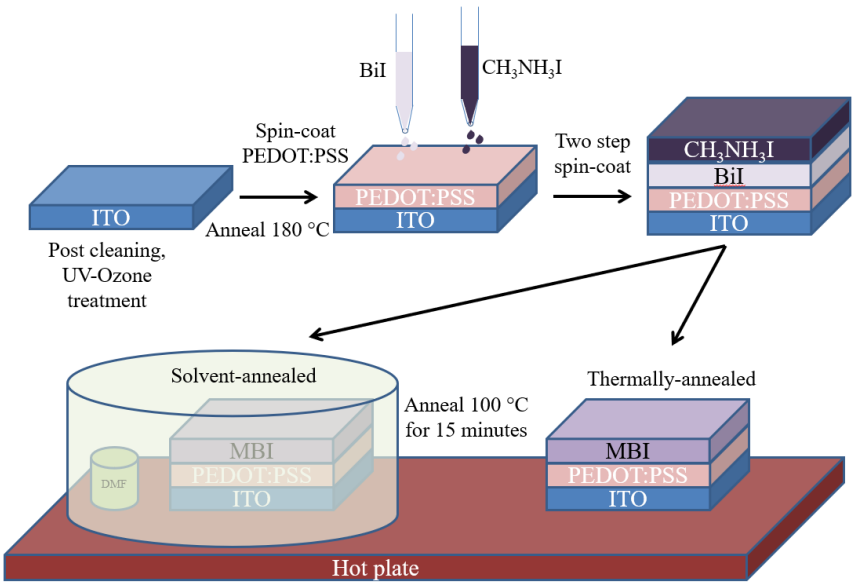

Figure 4.3. Schematic of MBI film fabrication and annealing procedures.

which also has a high dielectric constant, the precursor ions and molecules may diffuse further in the presence of saturated DMF vapor than without, which should lead to a larger grain size and a more crystalline morphology of the MBI film.

As anticipated, micrographs in Figure 4.4 obtained using field-emission SEM (FE SEM) show that the average grain size in the solvent-annealed MBI film (Figure 4.4c,e) (~7.5 μm across the hexagonal grain) was larger than that of the thermally annealed film (Figure 4.4d,f**)** (~5.5 μm across the hexagonal grain) by ~35%. This improvement is attributed to DMF vapor exposure, which enhances grain size and uniform surface coverage of the film. Cross-sectional SEM micrographs in Figure 4.4 also show a decreased roughness of the film surface after solvent annealing (Figure 4.4a**)**. Both the decreased surface roughness and increased grain size are

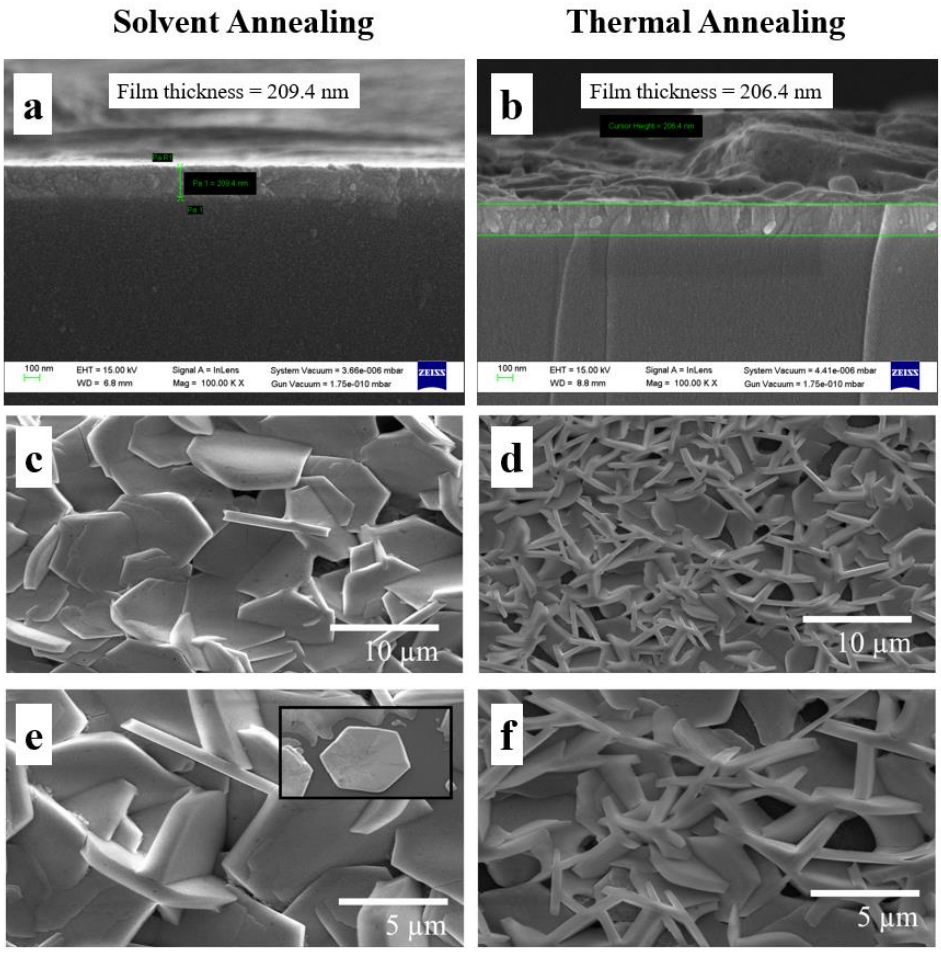

Figure 4.4. Cross-sectional SEM images and FE-SEM images of solvent-annealed MBI films (a,c,e) and thermally annealed MBI films (b,d,f) [inset in (e) to show larger size]. The grains increase in size following solvent annealing as seen in the FE-SEM images. The orientation of grains appears to be different between the thermally annealed and solvent-annealed films as seen in the cross-sectional SEM images.

influential on device performance. Uniform coverage will lead to consistent properties across the device and ease the stacking or growth of materials atop the perovskite film, and larger grain sizes will improve pathways for charge conductivity.

The cross-sectional SEM micrographs also reveal an interesting subtlety hinted at in the FE-SEM micrographs. As seen in Figure 4.4b, the thermally annealed MBI film grains seem to have a preferential orientation in which the grains are aligned such that the grain edges are in the out-of-plane direction of the film (grain edge-on configuration). This observation is reinforced by Figure 4.4d,f, as more grain edges are visible in the micrograph of the thermally annealed MBI film than that of the solvent-annealed film. The cross-sectional SEM micrograph of the solvent-annealed sample (Figure 4.4a), on the other hand, does not show this preferential orientation of the grains to be stacked edge-on. It is inferred, based on the FE-SEM micrographs

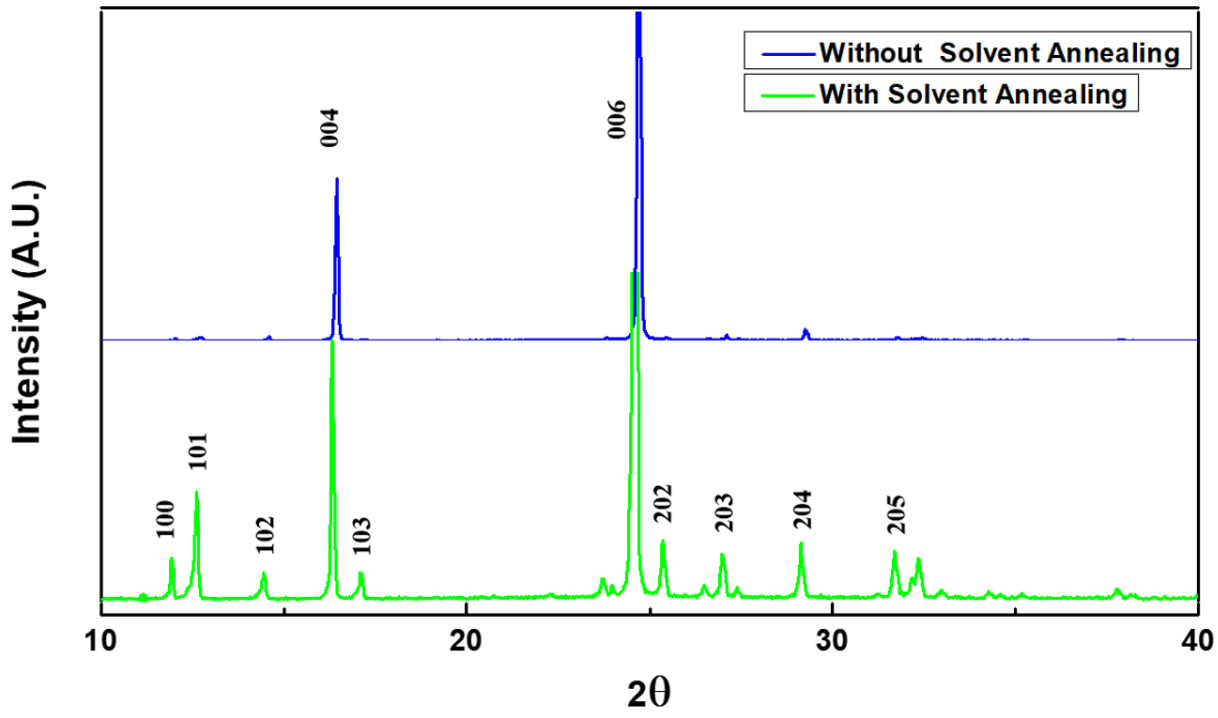

Figure 4.5. XRD patterns of solvent-annealed and thermally annealed (without solvent annealing) MBI films.

of the solvent annealed film (Figure 4.4c,e), though, that the preferred orientation of these grains is in the grain face-on configuration, as many more hexagonal grain faces are visible than grain edges.

To assess structural changes after solvent annealing of the MBI films, XRD was performed (Figure 4.5). We note very little to no shift in the XRD peaks between the thermally annealed and solvent-annealed MBI films, which signifies that there is little to no change in the unit cell of the MBI (or no solvent incorporation in the unit cell). A larger grain size (with less scattering of GBs) and/or increased crystallinity[156] of the solvent-annealed MBI film is qualitatively reflected in the XRD patterns, with the diffraction peaks of the solvent-annealed film being sharper than those of the thermally annealed films. To determine the crystal size qualitatively, Scherrer's equation[161] and the full-width at half-maximum values of the (004) peaks were used to calculate an average crystal size of ~85.9 nm for the solvent-annealed film and ~82.4 nm for the thermally annealed sample, which supports the finding that solvent annealing increases the crystallinity of the MBI films. Furthermore, the ratio intensities of the (004) to the (101) peaks were calculated for both the solvent-annealed and thermally annealed MBI films from the XRD patterns. The thermally annealed MBI film has a notably larger ratio, almost 20×, of the (004) peak to the (101) peak than the solvent-annealed MBI film. This indicates that there is some change in the preferred orientation of the crystals in the thermally annealed MBI film as compared to the solvent-annealed MBI film. In fact, this conclusion from the XRD data supports the previous observation made from the cross-sectional and FE-SEM micrographs.

The improved crystallinity as determined by the XRD of the solvent-annealed MBI films is responsible for the increase in the band-edge of optical absorption near 550 nm (Appendix E).

These absorption features match well with literature data.[152,162] Details and figures regarding these characterizations of the films, including absorption spectra, energy-dispersive X-ray analysis (EDAX; Appendix F**)**, and compositional mapping (Appendix G**)**, are also reported.

To further study the effect of improved crystallinity, increased grain size, and more uniform films due to solvent annealing on the optoelectronic properties of the MBI films, c-AFM and pc-AFM measurements were carried out for solvent-annealed and thermally annealed films of identical sample geometry. c-AFM and pc-AFM are both performed in the contact mode,

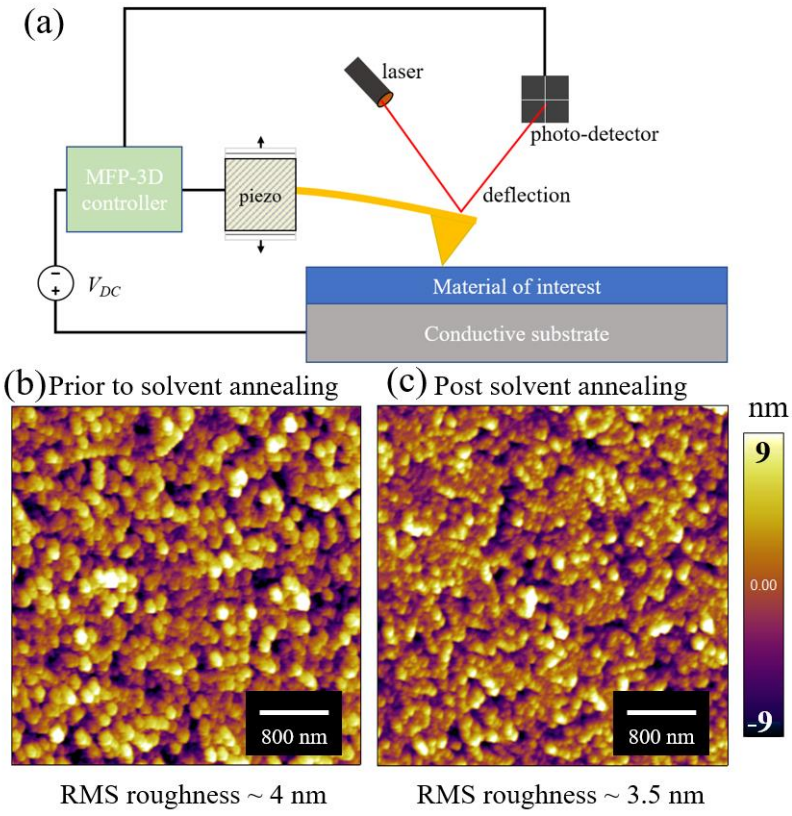

Figure 4.6. Schematic of the c-AFM set-up (a). AFM topography scans of films thermally annealed (b) and post-DMF annealing (c). A reduction in rms roughness is observed after solvent annealing.

which means that the AFM tip is touching the surface of the film as it raster scans. Bias voltages are applied to the base of the sample, and current is recorded through the tip. The schematic of the c-AFM technique is shown in Figure 4.6a. The surface morphologies of solvent-annealed and

thermally annealed films are also shown. We observe that solvent annealing reduces the surface roughness of the MBI film, with the root-mean-square (rms) roughness of the MBI film changing from ~4 to ~3.5 nm (Figure 4.6b,c). This finding of reduced rms roughness of the solvent-annealed MBI film qualitatively confirms the observation made from the cross-sectional SEM data.

Figures 4.7b,e shows example regions of the films in which the current is greatly enhanced at a very small applied bias voltage (1 mV) applied via the substrate in the solvent-annealed films as compared to the thermally-annealed films. It should be noted here that the

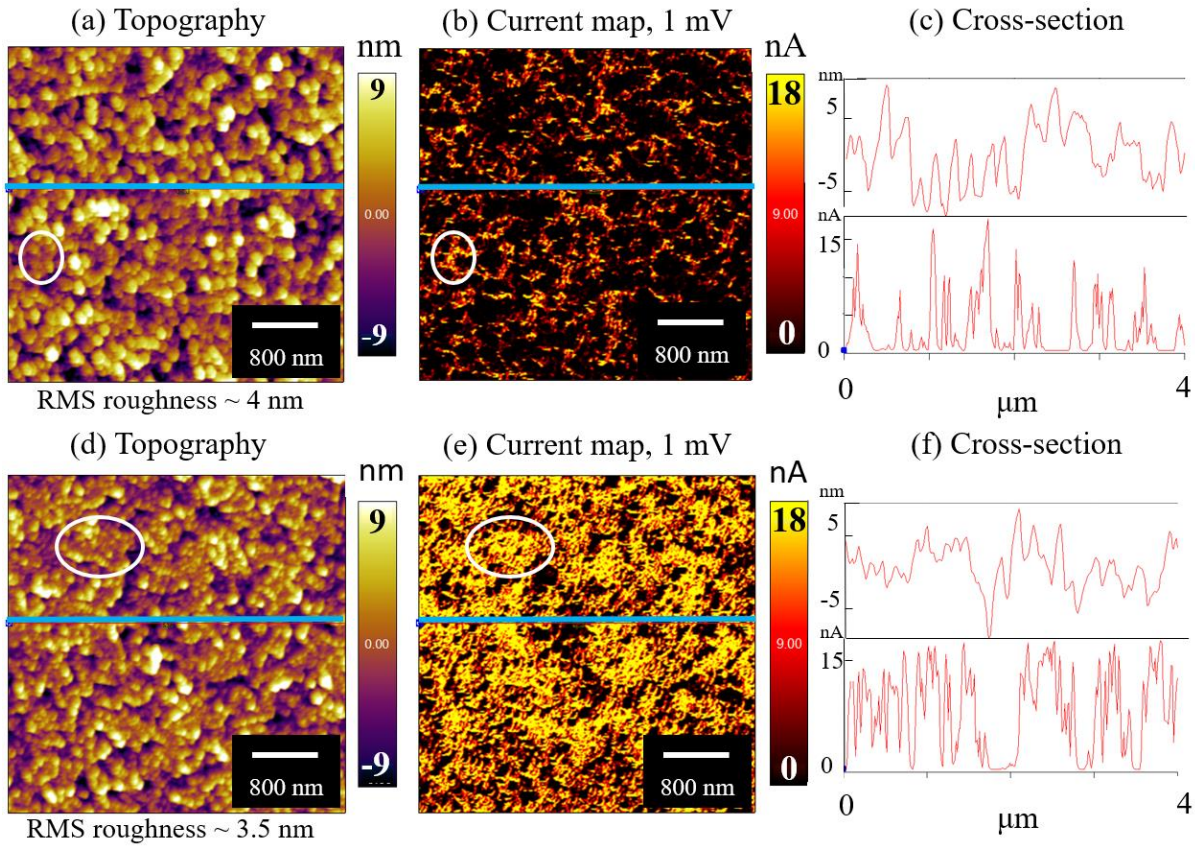

Figure 4.7. Topography and conductivity are compared before (a-c) solvent annealing and after (d-f) solvent annealing. Topography and current channels are shown on the same scale, respectively, before and after solvent annealing. The blue line on the topography and current maps corresponds to the cross-sections shown (c,f). The white circles in the topography and current maps contain what is believed to be a grain. A clear enhancement in conductivity is seen after solvent annealing.

measurements were taken in the dark (Figure 4.7). Line scans (Figure 4.7c,f) are provided to show the comparison between the topography and current channels, where a clear correlation between conductivity in the dark and sample height or GBs is not readily observed. We can note, however, in the solvent-annealed sample, that the current reaches the ~20 nA detection limit of our instrument (specifically our AFM cantilever holder) consistently across the sample surface, whereas in the thermally annealed sample, the maximum reached is around 15 nA and the peaks in current are much less frequent across the sample surface. This finding illustrates the importance of larger grain size and fewer GBs for improving conductivity in MBI films.

To probe more closely the role that grains and GBs play in the transport of charge in the

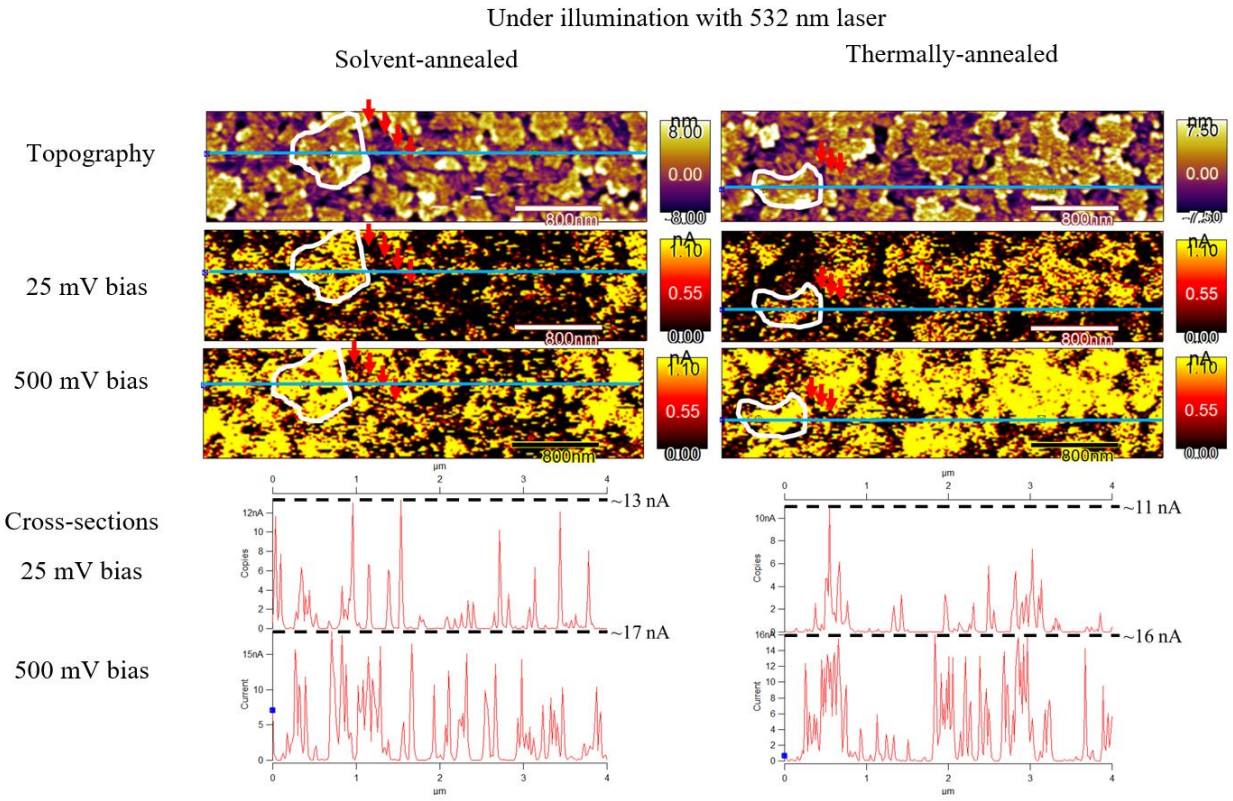

Figure 4.8. Comparison of solvent-annealed and thermally annealed MBI films in the illuminated condition (532 nm laser). From top to bottom: topography, photoconductivity at 25 and 500 mV applied bias, and cross-sections of the photoconductivity at 25 and 500 mV applied bias, and cross-sections of the photoconductivity at 25 and 500 mV applied bias. Grains are enclosed in white; GBs are indicated with red arrows; cross-section lines are shown in blue.

MBI films, we investigated the solvent-annealed and thermally annealed films both in the dark and under illumination of a 532 nm (green) laser with several bias voltages. The area of interest was smaller than that examined in Figure 4.7 to better discern conductivity changes in the grains and GBs. A new region other than that shown in Figure 4.7 was also chosen in which more visible grains were observed. Regarding the photocurrent differences across the film, there is currently no consensus in the literature regarding whether there should be a change in photocurrent between the grains and GBs, and studies have shown conflicting results owing to various contributions to photocurrent that can exist.[163] Although the GB is believed to behave like a recombination center because of defect sites and possess a lower photocurrent than inside the grain, the band bending around GBs, because of the interstitials and vacancies, forms a potential that favorably separates photogenerated carriers.[164]

Figure 4.8 compares a small area of the solvent-annealed and thermally annealed films at a small (25 mV) and a large (500 mV) bias voltage under illumination. Representative grains, enclosed in white, and GBs, indicated by red arrows, show differing behavior in both the solvent-annealed and thermally annealed films with increased bias voltage. The grains, with increasing bias voltage, show an increase in conductivity with higher current values being measured through the AFM tip. This appears to be consistent across the films, as other grains exhibit the same behavior. The GBs in both samples appear to be less affected by the increase in bias voltage, as a modest improvement to conductivity is readily observed at the GBs.

When the cross-sections (blue lines) of the conductivity maps are compared in Figure 4.8, the peak current value (~17 nA) across the representative grain in the solvent-annealed film is larger than that of the thermally annealed film (~16 nA). This is perhaps not unexpected, but it should be carefully noted as the peak current values between the two grains are much closer than

those in Figure 4.7 would lead us to expect, indicating some variation in film photoconductivity, particularly in the thermally annealed film. This could, in part, be attributed to the non-uniformity of the film thickness and surface roughness we observe in these films. The increase in peak current values between biases in the solvent-annealed film corresponds to a ~31% increase from ~13 nA at 25 mV to ~17 nA at 500 mV. The increase in the peak current values between biases in the thermally annealed film, on the other hand, is slightly larger, corresponding to a ~45% increase.

It was previously seen that photocurrent more readily flows through grains than GBs in DMF-annealed lead-containing perovskites in the applied bias range of 0.2-0.4 V,[159,164] and this observation was attributed to the GBs acting as a recombination center. Conversely, this same report found higher photocurrent in GBs than in grains in the thermally annealed counterpart at biases exceeding 0.3 V, which is not consistent with what we observe in our thermally annealed MBI film. This difference highlights the idea that solvent annealing is not the only factor that dictates whether GBs act as channels for current flow or recombination sites. Rather, it seems that several factors, including processing like solvent annealing or perovskite elemental composition, could be responsible for the role GBs play in photocurrent pathways. Additionally, it is possible in our material that the bias needed to overcome the GB barrier is greater than the 0.3 eV noted for organolead halide perovskites.[164] Although we investigated up to 0.5 V biases in both the solvent-annealed and thermally annealed samples, we still did not note intergrain carrier transport, and instead saw only the grains in both samples to be more effective in transporting charge.

This finding from pc-AFM underscores an important point: for photovoltaic (PV) devices containing MBI films, regardless of the annealing procedure, photocurrent prefers to flow intragrain at applied bias voltages up to 0.5 V. This is a subtle but important distinction from other reports on organolead halide perovskites, as noted previously. For best device performance, then, the grain size of the MBI films should be maximized so that charge extraction processes in PV devices are optimized. This points to the vital importance of developing processing conditions, such as solvent annealing, to maximize the grain size in MBI films. Attention should also be paid to the effect these processing conditions have on the orientation of the crystals in the MBI films. We have seen from SEM micrographs that solvent annealing seems to lead to MBI films with hexagonal grains preferentially oriented in the face-on configuration, whereas thermal

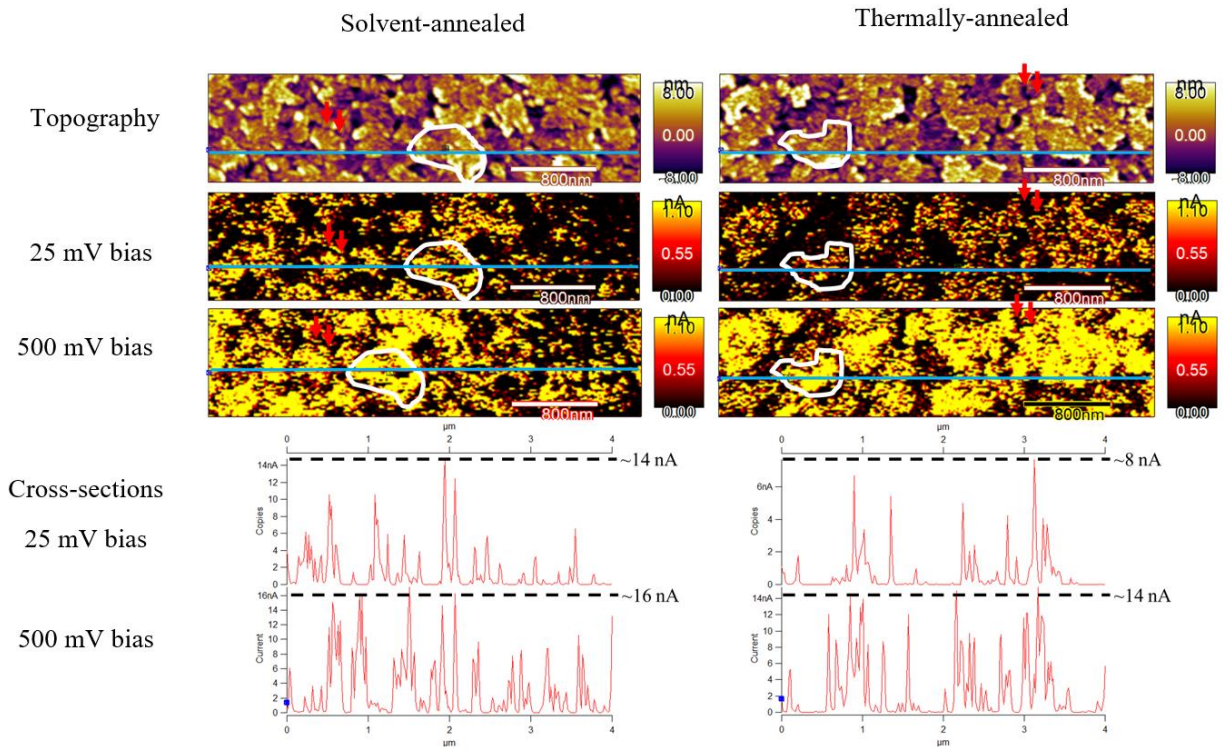

Figure 4.9. Comparison of solvent-annealed and thermally annealed MBI films under the dark condition. From top to bottom: topography, photoconductivity at 25 and 500 mV applied bias, and cross-sections of the photoconductivity at 25 and 500 mV applied bias. Grains are enclosed in white; GBs are indicated with red arrows; and cross-section lines are shown in blue.

annealing generates MBI films with the grains preferentially oriented in the edge-on configuration. Potential landscapes of hexagonal MBI grains extracted via Kelvin probe force microscopy have shown a potential boundary existing at the grain edge, with the grain interior having a lower potential value.[153] This observation combined with the c-AFM results we have that show suppressed intergrain transport suggests that the orientation of the grains could be quite important to device performance. In PV devices, with charges being extracted in the out-of-plane direction, this orientation effect, in tandem with grain size and crystallinity, could play a role in how efficiently charges are transported through the films.

To see the variation from the pc-AFM data of illuminated MBI films, we also compared the solvent-anneald and thermally annealed films at a small (25 mV) and a large (500 mV) bias under the dark condition. These results are shown in Figure 4.9. As with the illuminated condition, in both films, we see an increase in the conductivity within the grains (enclosed in white) and a negligible change in the GBs (indicated by red arrows) between the two biases. More notably, in both films, we observe decreased conductivity in the dark case as compared to the illuminated case in Figure 4.8, which is expected if the MBI films are respondent to green light. The UV absorption spectra of the MBI films indicate that this should be the case, and in fact, pc-AFM measurements under illumination confirm it. We also observe some differences between the illuminated (Figure 4.8) and dark cases (Figure 4.9) when comparing the cross-sections of the conductivity.

The increase in peak current values between biases in the solvent-annealed film corresponds to a ~14% increase from ~14 nA at 25 mV to ~16nA at 500 mV. In the thermally-annealed case, though, the increase is quite dramatic, corresponding to a ~75% increase from ~8 nA at 25 mV to ~14 nA at 500 mV. This finding points toward the greater significance of

illumination with a laser on the thermally annealed film in the transport of charges, particularly at small bias voltages.

Finally, we investigated the performance of PV devices based on the solvent-annealed and thermally annealed MBI films. Table 4.1 shows the short circuit current (J_{sc}), open circuit voltage (V_{oc}), and PCE resultant for prototype PV devices based on the two MBI films. The device structure was ITO/PEDOT:PSS/MBI/PCBM (10 nm)/aluminum (Al: 100 nm). The device area was 4.5 mm^2, as determined by the overlap of the cathode and anode. The current density-voltage (J-V) curves (Appendix H) for the MBI-based devices are available. It was observed that the champion device made from the solvent-annealed MBI film had a higher PCE than the device containing the thermally annealed MBI film. This is consistent with previous reports on this material.[158] Moreover, the improved PCE in the device containing the solvent-annealed MBI film supports our conclusion that solvent annealing improves crystallinity, increases grain size, and decreases MBI film roughness, which leads to enhanced optoelectronic properties.

device	**Eff (%)**	**V_{oc} (V)**	**J_{sc} (A)**	**FF**
thermally annealed	0.068	0.64	0.25	42.75
solvent-annealed	0.137	0.87	0.43	36.88

Table 4.1. Percentage Efficiency (Eff), Open Circuit Voltage (V_{oc}), Short Circuit Current (J_{sc}), and Fill Factor (FF) for the Two Devices, Thermally Annealed and Solvent-Annealed.

4.2.4 Conclusions

In summary, we investigated the optoelectronic properties of a lead-free perovskite MBI film at the nanoscale using pc-AFM after thermal and solvent annealing with DMF. Using XRD

and SEM, we confirm that DMF annealing increases the grain size and improves the crystallinity of the MBI films, which also contributes to an improvement of optoelectronic properties and device efficiency. We observe that photoconductivity and conductivity are higher in the solvent-annealed films than the thermally annealed films across the varying bias voltages tested. Furthermore, we demonstrate that the photoconductivity and conductivity increases in both films between a small and a large bias voltage are contained mostly within the grains, with no to very little increase seen at the GBs of the two films. This suggests that the barrier height of the GBs in this lead-free perovskite is larger than that of previously studied lead-containing perovskites (0.3 eV), as our largest applied bias of 0.5 V was not enough to promote intergrain carrier transport. This understanding of barrier height of the GBs, combined with improvements to photoconductivity with DMF annealing, is useful for further optimization of devices containing MBI films.

Chapter 5: Interfacial Interactions: Probing Strength of Interaction at Interface and its Effect on Polymer Structure

Manuscript in preparation by Wenderott, J. K.; Dong, B. X.; Amonoo, J.; Green, P. F.

5.1 Introduction

The thickness-dependent physical properties of dielectric polymer films, such as glass transition temperature (T_g),[165–168] segmental dynamics,[169–171] and mechanical response,[172] have been the focus of intense research in the past few decades. The effect of external interfaces, subsequently leading to confinement of the polymer film, has been discussed as the potential cause for many of these thickness-dependent properties, and was covered again recently in a detailed review.[173] Local packing of polymer chains near the substrate and free interfaces is different from the film interior depending on the short-range intermolecular interactions. At a free surface, for instance, an enhancement in the free volume as compared to the bulk leads to a liquid-like layer responsible for faster observed dynamics. This is not the case at the hard substrate interface, where often suppressed dynamics are measured. The T_g is often used as an example of a physical property that changes depending on the specific confinement of the polymer film. In free-standing thin films of linear polymer chains, the T_g is lower than that of the bulk, indicative of two "mobile" layers of chains at the two free surfaces. For identical supported

films, however, a competition arises between intermolecular forces at the substrate and those at the unconstrained free surface. In the case of polymers that interact strongly with the substrate (e.g. hydrogen bonding), T_g enhancement in thin films is observed, as is the case with tetramethyl bisphenol-A polycarbonate (TMPC) films on silicon substrates with a native oxide layer (SiO_x/Si).[167] On the other hand, weakly interacting polymer/substrate interfaces give rise to T_g suppression in thin films, indicative of the dominating effects of the free surface.

The length scales generally associated with the deviations of T_g of thin films are on the order of ~10s of nms, while other property changes have either comparable or larger length scales: effective modulus ~100s of nms, segmental dynamics ~several times the radius of gyration, viscosity ~10s of nms.[174] Simulations show packing density deviations on the order of ~1-2 nms,[175,176] creating a discrepancy that must be addressed utilizing long-range cooperativity coupled with short-range fluctuations to account for experimental evidence of long-range interface-induced property changes. Several models, including one described by Long and coworkers using percolation theory[177,178] and another by Schweizer and coworkers visualizing chain segments as "caged"[179], have attempted to marry these two concepts. The impact that confinement and interfacial interactions have on the physical properties in thin films and the long-range length scales associated with many of these property changes are both areas of active research.

One property that has not been investigated rigorously in terms of its thickness-dependence is surface potential, which is also referred to as contact potential difference (CPD) if the value is comparative between two materials. The CPD between two materials, lending information about the vacuum level shift, interface dipoles, and band bending behavior, has been measured and interpreted for organic semiconductor/metal (O/M), organic

semiconductor/organic semiconductor (O/O) and organic semiconductor/insulator (O/I) interfaces. Electronic polarization at these interfaces affects energy level alignment, ultimately influencing the function of numerous electronic devices containing such interfaces, like organic field effect transistors (OFETs), organic solar cells (OSCs), and organic light-emitting diodes (OLEDs). For example, at the O/M interface, band bending due to charge transfer influences the semiconductor density of states (DOS).[62,66,71,82,91] At the O/I interface where the number of free carriers in the insulating material is quite small, the CPD, or difference in surface potentials (work functions) of the two materials, depends on several factors including the polarity of dielectric material and processing conditions like deposition temperature.[180,181]

Less attention has been paid to what affects the CPD at the insulator/metal (I/M) interface, because the interpretation can be convoluted by several potential sources including interface dipoles, interfacial electronic polarization and/or a combination of surface and/or interior charges that can all contribute to the overall Coulombic interaction.[182] Efforts to attribute the CPD to one dominant factor, especially at O/I, I/M or I/I interfaces where there is no charge transfer, has indicated that in materials with strong dipole moments, like self-assembled monolayers (SAMs), surface potential as measured by KPFM could be related to the strength and orientation of the dipole.[183] As shown with SAMs, the potential, ΔV, could be related to the vertical component of the dipole relative to the substrate by the Helmholtz equation (5.1):

$$\Delta V = \frac{\mu_z}{A\varepsilon_0\varepsilon}, \tag{5.1}$$

where μ_z is the average vertical component of the molecular dipole $\vec{\mu}$, A is the given molecular area, ε_0 is the relative permittivity of the void, and ε is the relative permittivity of the film in question. Depending on the orientation of the dipole, a contrast can either be seen in the negative or positive direction.

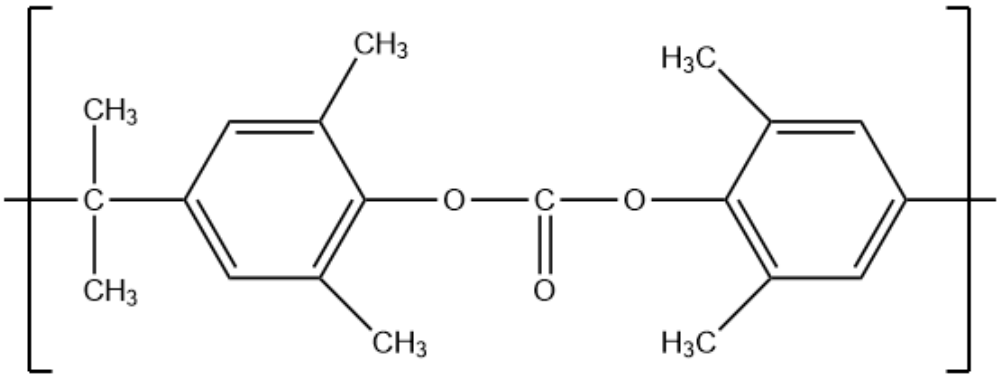

Figure 5.1. TMPC monomer structure. Dipole moment of monomer calculated to be ~1.6 D due to C=O bond.

At the buried interface of a thin polar polymer film and conductive substrate, an example of a special I/M interface, the effect of interfacial interactions on the average polymer dipole orientation can lend information about the polymer chain configurations[184] and film structure near the substrate. This assessment is valuable to better understand if and how morphological changes occur due to interfacial interactions. In other words, a link between chain dipole alignment, thin film structure, and interfacial interactions can be formulated, which to date has not been extensively explored. Information exists about the chain dynamics near interfaces with interactions of varying strength, but at temperatures well below T_g of polymers, after processing and/or quenching, it would be useful to probe the structure of polymer films near this buried interface. Film structure influences a host of insulating polymer properties, including gas transport and sorption[185] and mechanical toughness,[186] and the ability to monitor how structure is affected by interfacial interactions is especially pertinent to thin film applications in which an I/M interface exists.

To this end, KPFM was utilized to measure the CPD of the insulating polar polymer TMPC (μ_{TMPC} ~3.5 D for monomer) on gold and doped SiO_x/Si. The TMPC monomer structure is shown in Figure 1. TMPC has vastly different interfacial interactions with SiO_x/Si and Au

substrates, with hydrogen (H-) bonding occurring on the SiO_x/Si substrate and only van der Waals interactions at play on the Au substrate. CPD trends revealed a sharp increase in the thin TMPC films on SiO_x/Si, which was attributed a change to the average dipole orientation of the TMPC polymer chains near the buried interface. This CPD trend was in distinct contrast to that of TMPC on Au, which was measured to be nearly flat across a range of TMPC film thicknesses. To quantify the average bond orientation of the TMPC chains on SiO_x/Si, several signature bonds of TMPC were monitored with polarized Fourier transfer infrared spectroscopy (p-FTIR) at different TMPC film thicknesses. The effects of the interfacial interactions at the buried I/M interface can be monitored non-destructively using KPFM, and our findings show interfacial interactions alter the local chain morphology near the substrate.

5.2 Experimental Section

All substrates used in this study were cleaned via ultrasonication in deionized water, acetone and 2-propanol for 10 minutes each. TMPC (Bayer, Mw=38 kg/mol, PDI=2.75) was dissolved in toluene and allowed to mix in solution overnight prior to filtering. Solutions for KPFM measurements were spin-casted onto either (1) doped Si substrates (Wafer World) with a doping concentration of at least 5x1018 cm-3 with a native oxide layer of ~1.5 nm or (2) Si substrates (Wafer World) with a gold layer (~100 nm) deposited on top. For p-FTIR measurements, films were spun onto double-sided polished Si wafers. Varying thicknesses of each film were made from tens to hundreds of nanometers by adjusting spin rates and solution concentrations. Thicknesses were verified both with spectroscopic ellipsometry (JA Woolam, M-2000) and with atomic force microscopy (Asylum Research, MFP-3D). Each film was annealed at Tg+10 °C in a vacuum oven for 4 hours.

Prior to KPFM measurements, a scratch was made across the polymer films with a blunted needle or sharp wooden stick to expose the Au or SiOx/Si substrate. At this scratch location, simultaneous electrical potential and topography measurements were made, allowing for the assessment of the thickness and CPD of the film. Figure 5.2 shows an example of a scratched region measured of a ~200 nm TMPC film on SiOx/Si. To extract values for the CPD

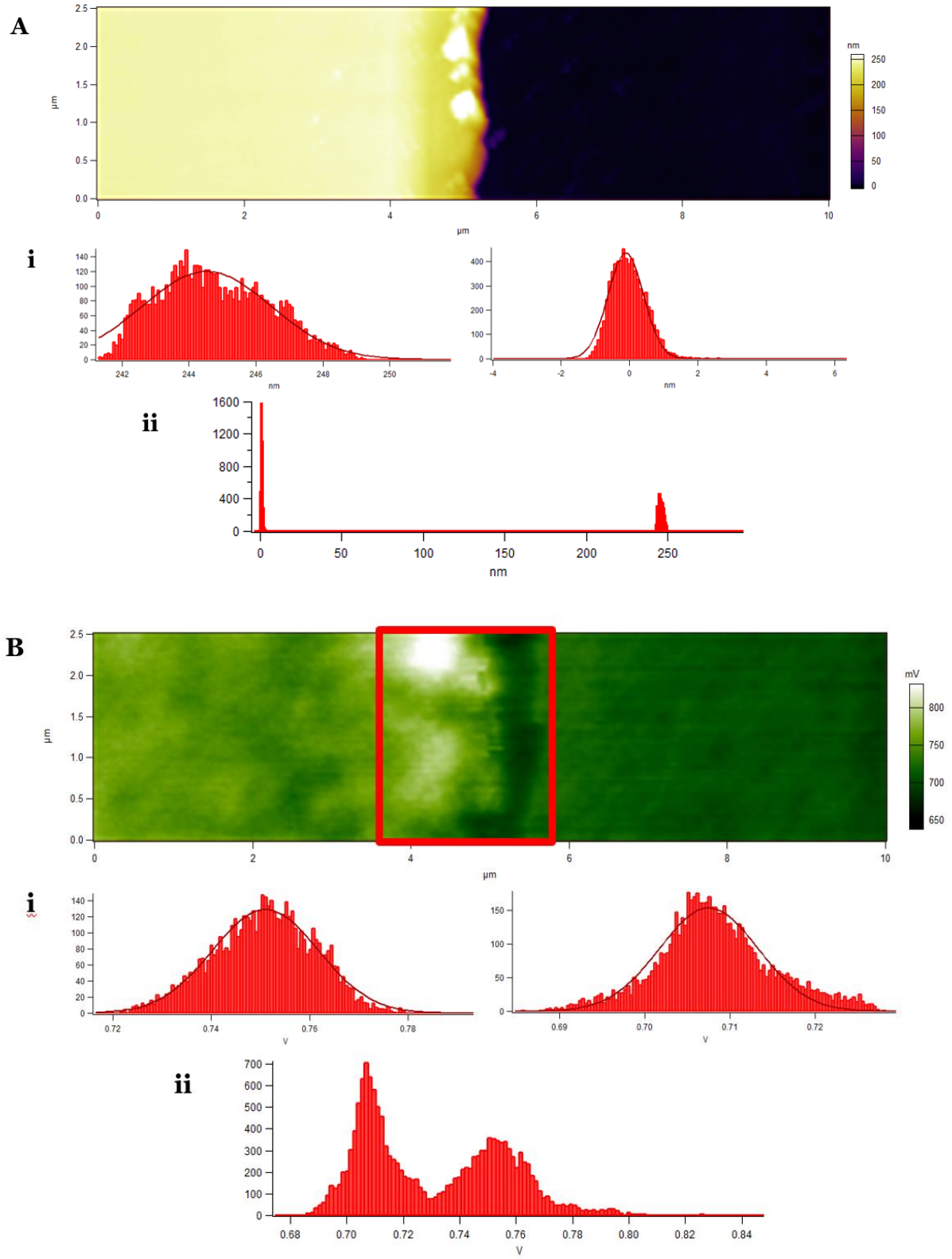

Figure 5.2. Example of 10 x 2.5 µm topography (A) and surface potential (B) scan of scratched TMPC film region. Histograms from each region (i) were fitted with Gaussian curves and subtracted to find thickness and CPD. The surface potential region at the polymer/substrate interface was excluded (boxed in red) was excluded from analysis. Histograms of the full image (ii) are provided for reference.

and thickness, each region (polymer and substrate) was binned in a histogram and the average value was found with a Gaussian fit. These values were then subtracted from one another to find the CPD between TMPC and the substrate and thickness. It should be noted that the region at the interface of the scratch was excluded from the surface potential averaging. This was because such a sharp interface has capacitive "edge effects" caused by the finite probe size,25 and to ensure no artefact contributed to the average surface potential value, this area was excluded altogether.

The sample was earthed to a metal disk with silver paste, which was electrically connected to the AFM with a wire. KPFM measurements were performed using Pt-coated Si probes made by Nanosensors (stiffness ~0.5-1 N/m, resonant frequency ~75 kHz) on an Asylum Research MFP3D atomic force microscope. Most measurements were made in air with 10-30% humidity. KPFM acts as a double-pass, intermittent contact technique. First, the sharp metallic tip raster-scans across the surface of interest, measuring the topography. During the first pass, the cantilever is driven at its first harmonic resonance frequency, and the amplitude of this mechanical oscillation is used as the feedback signal. In the second pass, which follows the same path as the first pass, an AC bias at the first harmonic resonance frequency of the cantilever is applied to the tip that generates oscillating electrical forces between the tip and sample. The mechanical oscillations of the cantilever are set to zero and the tip is lifted to a set height ("lift height"). This distance is between 10-20 nanometers, which captures the electrostatic interactions but remains far removed from short-range VDW forces. A lock-in amplifier is employed to extract the electrical force component with the first harmonic frequency and apply a DC bias until this oscillation is nullified. These oscillations are continually nullified as the tip follows the second pass, providing a local map of the surface potential. A schematic of the

KPFM technique is shown in Figure 5.3 and Appendix A and a control study on a Bi:Sn alloy to ascertain the validity of our technique is shown in Appendix I.

p-FTIR measurements were performed using a Thermo Scientific Nicolet 6700. The sample stage consists of a variable angle goniometer that is utilized to position the sample at the Brewster's angle (Θ=16.3°) with respect to the incident IR beam. The Brewster's angle is used because an electric field oscillating perpendicular to the substrate incident at this angle has no internal reflection. This condition is known as p-polarized, and this p-polarized absorption spectrum is necessary for clean fitting of the spectra. Spectra transmitted are subtracted from the spectra of a blank Si substrate that has experienced the same surface treatment as other substrates. An average of 256 scans produce each spectrum, and the spectra are baseline-corrected before analysis. The absorbance amplitudes A_s and A_p of the s- and p-polarized spectra at frequencies corresponding to specific bonds on the polymer chain are used to find the dichroic

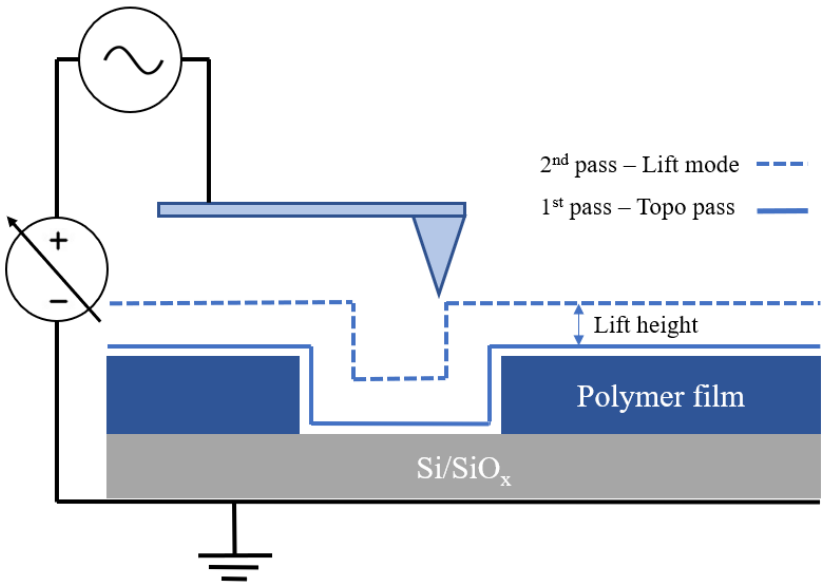

Figure 5.3. Schematic of relative surface potential measurement using KPFM. First pass is topography scan, probe is lifted to set height and potential mapping occurs on second pass.

ratio A_p/A_s. As the p-polarized beam is mostly absorbed by functional groups having out-of-plane transition dipoles and the s-polarized beam is absorbed by those groups having in-plane transition dipoles, this ratio yields information regarding the in-plane or out-plane orientation of the bond relative to the substrate. More information about this technique can be found elsewhere in literature.[187,188]

The dipole moment for TMPC was found using the MOPAC interface within Chem3D 16.0. The structure was first drawn in ChemDraw and then imported into Chem3D in which the dipole moment calculation was made.

5.3 Results and Discussion

To better understand if KPFM can probe the static dipole orientation of a thin polar polymer film, and thus yield information about the film structure, varying thicknesses of TMPC were measured on two substrates: doped silicon (SiO_x/Si) and one-hundred-nanometer gold on silicon (Au(100)/SiO_x/Si). These different substrates were chosen because the TMPC monomer has a C=O bond, which interacts quite differently with substrates depending on their surface chemistry. If a substrate has dangling hydroxyl groups (like the native oxide, SiO_x, on top of silicon), the C=O bonds of the TMPC will participate in H-bonding. If a substrate is anatomically clean, like deposited gold, no H-bonding of the TMPC will take place. In this way, the potential dipole orientation of TMPC, and whether it is affected by the substrate and interfacial interactions, was explored using KPFM.

As mentioned previously, KPFM has been used successfully to probe the strength and static dipole orientation of SAMs.[183] There are points of caution to be made when comparing CPDs of SAMs and polymer films. Since the SAM is only made up of one layer of molecules,

there is minimal confusion where the contrast in CPD comes from. In a polymer film with a certain thickness, though, there is a question regarding which part of the film is responsible for the CPD. KPFM has generally been labelled as surface technique, a local analog to macroscopic Kelvin probe and ultraviolet photoemission spectroscopy (UPS), each designed to probe the first one or two nanometers of a sample. As was shown by Liscio and coworkers, though, KPFM has an effective sampling depth (h_{eff}) associated with it of around 70 nm.[80] This finding indicates that both the surface and sub-surface dipoles, among other potential sources, of a polymer film could contribute to the CPD signal measured with KPFM. Indeed, the sampling depth affects how much of the sample KPFM "sees", whether that is the entirety of the film if it is thinner than the sampling depth ($h_{film}<h_{eff}$), or if it is a portion of the film if it is thicker than the sample depth ($h_{film}>h_{eff}$).

Figure 4 shows how the CPD measured of several TMPC thicknesses changed on the substrates mentioned above. Interestingly, the trends of the CPD are different depending on the substrate. Atop both the SiO_x/Si, as the thickness of the TMPC decreases, the relative surface potential increases. This increase begins at thicknesses of TMPC films less than 100 nm, which is commensurate with KPFM picking up polymer/substrate interactions at its observed depth of probe. The behavior of CPD with thickness of TMPC films is very different on the Au(100)/SiO_x/Si. Instead of seeing an increase in the CPD in thinner films, little change is observed across all thicknesses of TMPC films. Interestingly, there may even be a slight decrease in CPD as the thickness decreases.

The trends observed in Figure 4 are noteworthy, as the CPD is not constant for TMPC films across thicknesses. Changes to surface potential with thickness of polymer films has been observed in semiconducting polymers, but this is attributed to band bending behavior, with

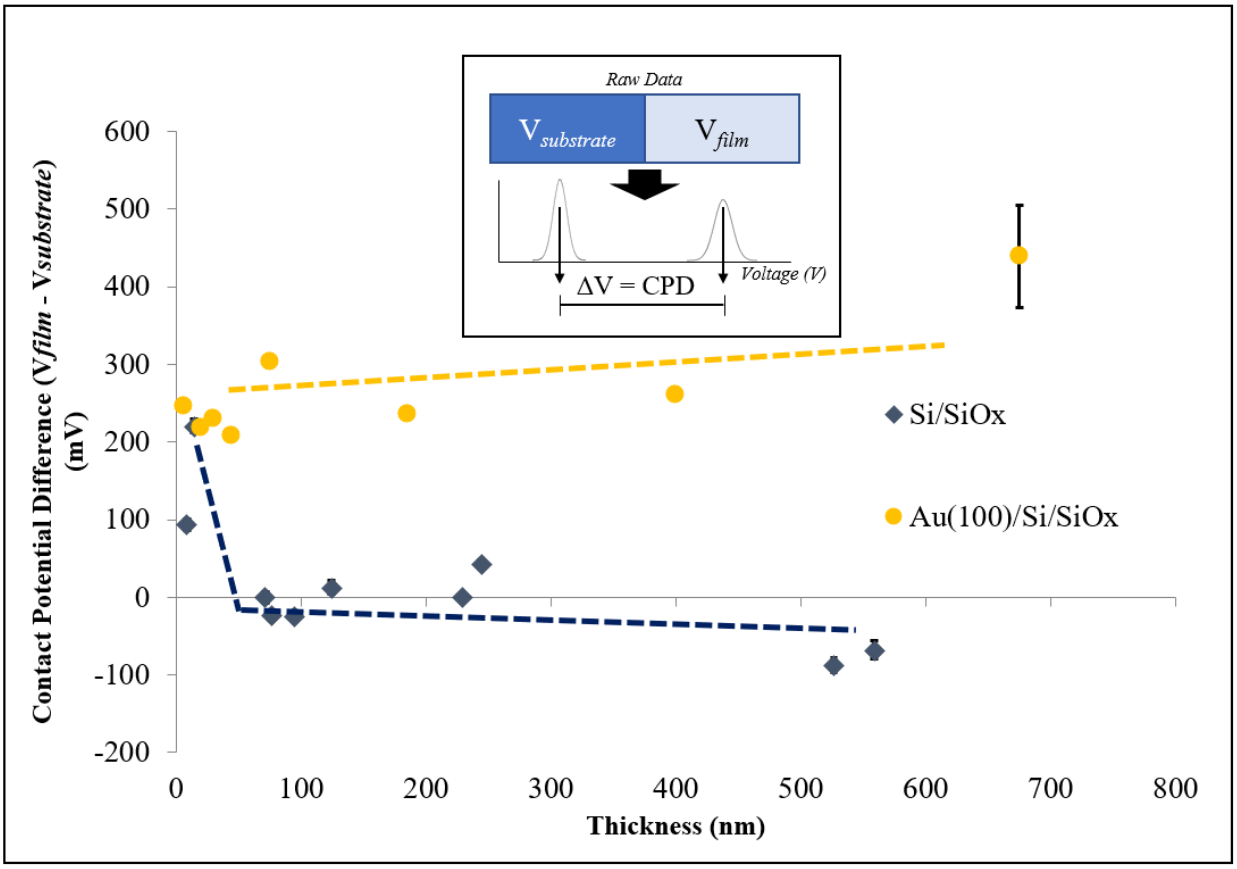

Figure 5.4. Relative surface potential over range of thicknesses for TMPC films on two different substrates. TMPC films on SiOx/Si show an increase in CPD in the thinnest films, while TMPC films on Au(100)/SiOx/Si show little change to CPD across the film thicknesses. Dotted lines are provided as guides to the eye.

charge transfer occurring between the conductive substrate and film. This is not the case with TMPC, with its very low charge carrier concentration. Thus, the change to CPD with film thicknesses must originate from a different mechanism. As alluded to previously, because of the polarity of the TMPC monomer, a large contributor to the CPD could arise from the average vertical orientation of the dipole moment. Theoretically, using the Helmholtz equation (1), an expected value for ΔV can be calculated. The molecular area of the TMPC monomer and dipole moment were found through Chem3D to be 155.38 $Å^2$ and ~3.5 D. Using $\varepsilon = 2.9$ as the relative

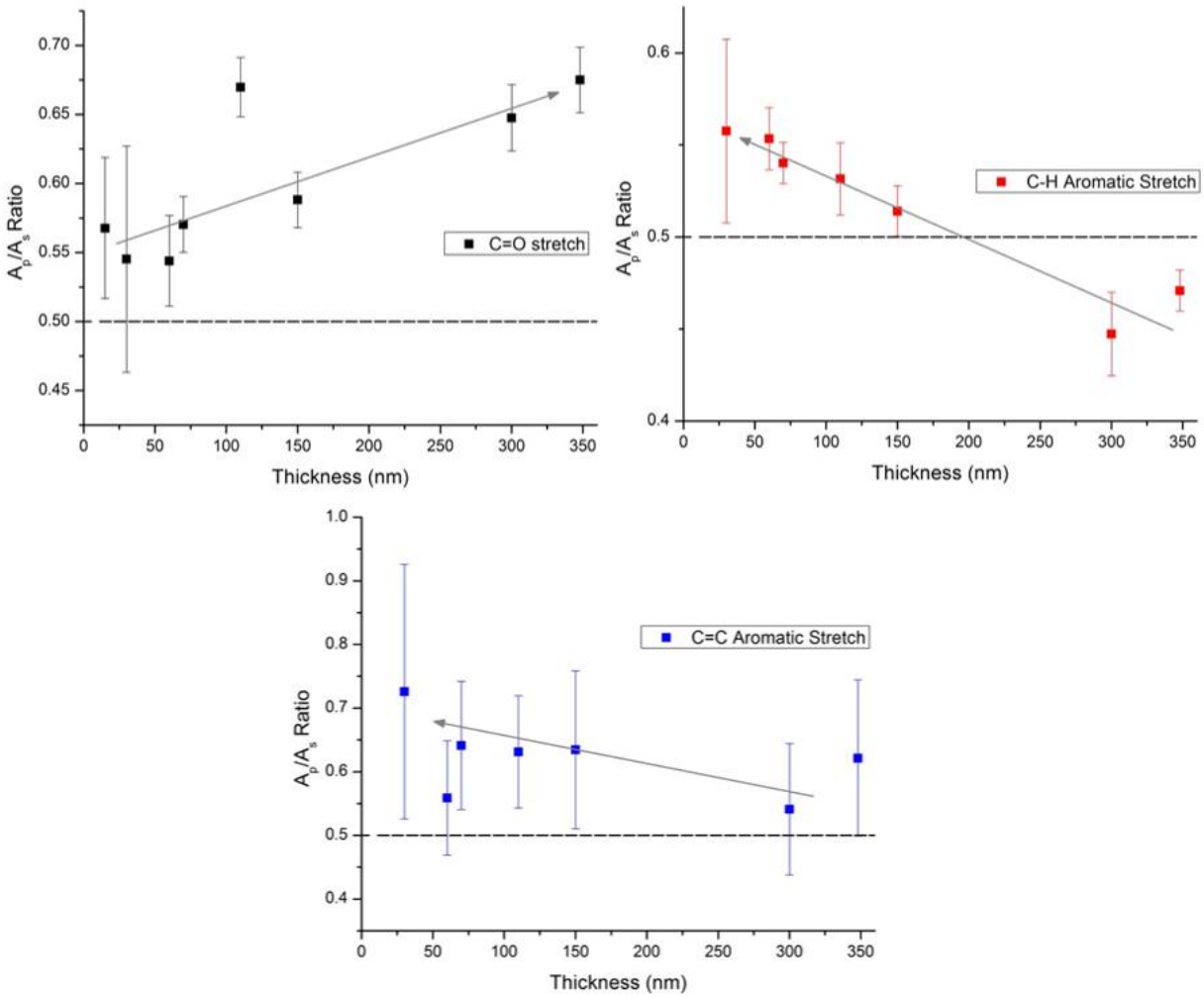

Figure 5.5. A_p/A_s ratios for three signature TMPC bonds measured via p-FTIR. The black dashed line denotes Ap/As=0.5, which indicates no preferred in- or out-of-plane orientation of the bonds.

permittivity, the expected (or "ideal") value for ΔV if the average orientation of the dipole moment is in the vertical direction was calculated to be 0.124 V, or 124 mV. The spike seen experimentally in the CPD in the thin TMPC films is about ~200 mV, which indicates that the average orientation of the dipole moment is primarily in the vertical direction in these films. It should be noted that because there can be additional contributions (trapped and/or surface charges) to the CPD, it is prudent to look at the change in CPD as opposed to the absolute CPD value. This way, information about the changes to the polymer chain orientation, and thus film

structure, can be isolated. Furthermore, contributions to the CPD measured, for example from an additional dipole contribution from hydrogen bonding oriented in the vertical direction, existing in the TMPC/SiO_x/Si system could be present. These contributions would be additive to the CPD.

With the hypothesis that varying interfacial interactions are influencing the TMPC dipole moment orientation and thin film structure near the interface, an attempt to quantify this change to structure further was made. Because of the polarity of the C=O bond in TMPC, p-FTIR was used to monitor the orientation of this signature bond, as well as others present in TMPC, in several film thicknesses. For each signature bond, trends of the ratio A_p/A_s with film thickness were recorded. If A_p/A_s=0.5 (isotropic), there is no preferred orientation of the functional groups being probed. If A_p/A_s>0.5, the *p*-polarized electric field, which oscillates almost perpendicular to the substrate, is being mostly absorbed by the out-of-plane transition dipoles of the functional groups. Thus, the high A_p/A_s ratio infers out-of-plane orientation of the functional group dipoles.[187] Conversely, if A_p/A_s<0.5, the *s*-polarized electric field, which oscillates almost parallel to the substrate, is being absorbed by the functional groups having in-plane transition dipoles. The low A_p/A_s ratio indicates in-plane orientation of the functional group dipoles.

The results from the p-FTIR and KPFM studies combined present a consistent picture. TMPC polymer chains near to substrates with which they interact strongly (*e.g.* H-bonding) tend to be more preferentially aligned than those chains near substrates with which they interact weakly (e.g. VDW interactions). In the case of TMPC on SiO_x/Si substrates, where H-bonding between TMPC and the substrate occurs, this alignment of the chains near the substrate results in a preferred orientation of the average dipole moment of the monomers in the thin film near the substrate. The preferred orientation of the average dipole moment is indicated by the spike in the

CPD measured with KPFM of the thinnest TMPC films atop SiO_x/Si substrates. In thin TMPC films atop gold substrates, with which the chains interact only via weak van der Waals interactions, there is no distinct change to the CPD across the range of TMPC thicknesses tested. This finding suggests the weak VDW interactions are not responsible for any ordering of the average dipole moment of the TMPC monomers nearest to the substrate. Using p-FTIR, the signature C=C and C-H bonds are seen to be more preferentially oriented in the out-of-plane direction in the thinnest TMPC films atop SiO_x/Si than thicker TMPC films on SiO_x/Si. Furthermore, the C=O bonds of TMPC on average are oriented in the out-of-plane direction across a range of TMPC thicknesses. Together, the information from p-FTIR lends weight to the results from KPFM, showcasing that together these tools can provide a wealth of information about thin film polymer structure at buried I/M interfaces.

5.4 Conclusions

In conclusion, the effects of interfacial interactions on the surface potential of a polar polymer, TMPC, were studied with KPFM. It was found, remarkably, that the trends of the CPDs of the TMPC were very different depending the interfacial interactions between TMPC and the underlying substrate. Thin TMPC films atop substrates with which they interact strongly *via* H-bonding, like SiO_x/Si, are seen to have a preferred orientation of their average monomer dipole moment, which is manifested in a spike in the CPD as measured with KPFM. CPD measurements of thin TMPC films atop substrates with which they interact weakly *via* VDW interactions, like Au, show no significant changes across a range of film thicknesses. The orientation of several signature TMPC bonds on films atop SiO_x/Si are probed with p-FTIR, and the results highlight trends of the bonds to be oriented more in the out-of-plane direction in thin

TMPC films, thus validating the KPFM measurement of such films. As studies of highly polar SAMs have shown, assessing the average dipole orientation using KPFM is distinctly achievable. To date, though, this has not been shown with polymer thin films. Our results indicate that KPFM, beyond its widespread use to investigate conductors and semiconductors, is also a useful tool for probing insulating polymer films and the buried I/M interface between the film and underlying substrate. Furthermore, we find that interfacial interactions at the I/M interface affect the morphology of thin polymer films, which is important for thin film properties and applications that employ I/M interfaces.

Chapter 6: Conclusions

6.1 Summary

Morphological design of polymer thin film systems allows for the manipulation of polymer properties. Whether the polymer is primarily semi-crystalline or amorphous, the nano- and microstructure of the polymer is responsible for properties that can vary orders of magnitude, showcasing the extrinsic nature of many polymer properties. The control of polymer morphology affords great challenges and opportunities, as precise adjustment of polymer properties for advanced applications from field-effect transistors to organic photovoltaics is extremely appealing for successful implementation. This dissertation demonstrates several ways that polymer and hybrid morphologies can be designed from film fabrication and post-processing of films to modification of the polymer/substrate interface. The focus of Chapters 2-4 is the morphology-electronic property relationship of semiconducting, or conjugated, polymer thin films, with an additional study in Chapter 4 on bismuth-based perovskite films. Chapter 5 concentrates on insulating polymer thin films and the influence of interfacial interactions on their morphology. Each design tool discussed offers a range of tunability to the material properties, and these changes to material properties are examined when possible with theoretical frameworks that shed light on what is occurring at the nanoscale. The work in this dissertation provides greater understanding of the complex morphology-property relationships in polymer thin films, especially with regards to the wide range of properties accessible for a single polymer,

which promises improvements to current device fabrication processes as well as for the informed design of future organic and hybrid devices.

The morphological design tool of Chapter 2 was film fabrication, specifically the creation of a unique globular morphology using a laser deposition technique called matrix-assisted pulsed laser evaporation (MAPLE). Both spin-casting and MAPLE-deposited poly(3-hexylthiophene) (P3HT) films were investigated, and the morphologies due to fabrication influenced the electronic properties of P3HT as much as the differences noted between two conjugated polymers with different chemistries. Specifically, the density of states (DOS) width of the MAPLE-deposited film was larger than that of the spin-cast film, signifying an increase to energetic disorder due to an increase in the structural disorder. The DOS width was extracted from band-bending data, which probes the degree to which the energy levels of the polymer shift close to the polymer/electrode interface as charge is transferred between the two materials after Fermi level alignment. Out-of-plane carrier transport of the MAPLE-deposited P3HT film was suppressed as compared to the spin-cast counterpart. This suppression was also attributed to the more-disordered film morphology of the MAPLE-deposited films.

In Chapter 3, the effect of interfacial self-assembled monolayers (SAMs) on the morphology and electronic properties of P3HT was studied. The substrates and modified substrates tested in this chapter were bare ITO, ITO modified with trichloro(1H, 1H, 2H, 2H-perfluorooctyl)-silane (FTS) (FTS/ITO) and ITO modified with octadecyltrichlorosilane (OTS) (OTS/ITO). SAMs modify both the work function (WF) and surface energy of the substrate. As band bending at the polymer/electrode interface depends on the substrate WF and electronic structure of the polymer, this study allowed for the probing of the combined influence of interfacial SAMs on the overall electronic properties of the P3HT. As found in Chapter 2, the

MAPLE-deposited films, regardless of substrate, had more pronounced band bending than the spin-cast films, which corresponded to larger DOS widths. When assessing the finer differences to properties of the MAPLE-deposited films on various substrates, it was noted that substrate surface energy altered by the SAMs affected thin film P3HT morphology. Specifically, P3HT films atop higher surface energy substrates were less structurally-disordered than those atop lower surface energy substrates. While WF of the substrate was also responsible for the band bending observed, the change to the surface energy of the substrates was implicated as the main contributor to the structural disorder that influenced energetic disorder of the P3HT films.

Chapter 4 focused on the use of post-processing to create distinctive morphologies of P3HT and bismuth-based perovskite films. Spin-cast P3HT films, previously seen in Chapter 2 to have some sample-to-sample variation in their measured WF, were subjected to solvent annealing with chloroform. Upon solvent annealing, the spin-cast P3HT films spun from two different solvents were seen to have more uniform WFs across a range of film thicknesses, which indicated more stable morphologies formed. Furthermore, DOS widths extracted from band bending were much narrower than those of MAPLE-deposited films, which confirmed quantitatively the decreased energetic disorder present in these more well-ordered spin-cast films. Solvent annealing with dimethylformamide was also used as a post-processing technique on lead-free perovskite methylammonium bismuth iodide (MBI) films. A comparison between thermally and solvent-annealed MBI films revealed that solvent annealing increased grain size, reduced film roughness, and preferentially orientated the grains in the face-on direction in the MBI films. Along with changes to film morphology, the solvent-annealed MBI films also had improved intra-grain conductivity over thermally annealed films. Additionally, photovoltaic devices fabricated with solvent-annealed MBI films had increased power conversion efficiency.

Finally, Chapter 5 explored how interfacial interactions altered thin film morphology of tetramethyl bisphenol-A polycarbonate (TMPC), an insulating polar polymer. TMPC is known to hydrogen bond with silicon substrates that possess a native oxide, and this strong interfacial interaction influences the TMPC thin film properties, including glass transition temperature. To investigate the role of interfacial interactions on the thin TMPC film morphology, films were spun atop silicon (with a native oxide) and gold substrates. TMPC chains interact weakly with the gold substrate via primarily van der Waals (VDW) interactions. A comparison of TMPC surface potential trends on the two substrates revealed a spike in the surface potential of thin TMPC films atop silicon with a native oxide. With the surface potential of polar species being related to the vertical component of the dipole moment, this spike indicated a positive contribution to the vertical component of the dipole moment from the TMPC chains near the interface. This finding showed that interfacial interactions can contribute to the ordering of insulating polymer chains near the interface, and this structural change can be probed with surface potential measurements. To corroborate the ordering of the chains, polarized Fourier transform infrared spectroscopy was used to assess TMPC signature bond orientation in the in- and out-of-plane directions.

6.2 Future Outlook

The morphological design strategies discussed in this dissertation provide many launching points for future research on organic, inorganic, composite, and hybrid materials. Regarding film fabrication with MAPLE, much work remains not only on neat polymer films, but also on polymer composite films and multi-layer films. MAPLE deposition, as noted in

Chapters 2 and 3, allows for creation of films with increased energetic and structural disorder. While our studies have noted some connection between the two, with increased structural disorder leading to increased energetic disorder, full understanding of how the two terms of disorder affect each other and polymer properties is still required.

Additionally, a couple of distinct advantages MAPLE deposition offers over traditional spin-casting is noted in the fabrication of polymer composite films and multi-layer films. While spin-casting of polymer composite films from solution can lead to significant aggregation of the inorganic component, MAPLE deposition allows for the composite solution to be frozen in place prior to deposition, thus leading to films with less aggregation of the inorganic component. To study the influence of MAPLE fabrication on polymer composite morphology and properties, P3HT/carbon nanotube composites are currently being fabricated and investigated. It is expected that depressed aggregation of components could be applied to fabricate polymer composite films with a wide variety of inorganic components including graphene, graphene oxide, and metal nanoparticles. This idea of limited aggregation in a two (or greater) component polymer system could further be used to fabricate polymer blend films. Current fabrication of multi-layer polymer films, often from spin-casting, requires the use of orthogonal solvents to successively spin layers of polymer. MAPLE deposition circumvents the use of orthogonal solvents, as multiple frozen polymer targets can be used during the same deposition. For all of these reasons, the use of MAPLE as a fabrication tool to design unique and technologically-relevant polymer systems is attractive.

As discussed in Chapters 3, 4, and 5, post-processing and interfacial modification also serve as morphological design tools with a lot of promise. While solvent annealing was the primary post-processing technique discussed in this dissertation, others exist that have their own

benefits. Super-critical carbon dioxide ($scCO_2$) has been used successfully to alter backbone orientation of P3HT chains near to a dielectric interface,[65] which has meaningful implications for applications that have charge carriers moving near this interface, like thin film transistors. Furthermore, $scCO_2$ is environmentally friendly, with CO_2 being abundant and non-flammable. It is noted that post-processing has often been used on spin-cast polymer films, but little work has been done to post-process MAPLE-deposited polymer films. With the mechanism of MAPLE deposition including processes that resemble nucleation and growth dynamics, it is possible that MAPLE-deposited films subjected to post-processing would experience increased "grain"/globule size and even preferential "grain"/globule orientation. This hypothesis is tentatively supported by the findings from Chapter 4 which showed that organometal halide perovskite grain size and orientation can be vastly changed by post-processing like solvent annealing. If MAPLE-deposited films could be altered to produce less rough and more crystalline or ordered films with improved properties through post-processing, the utilization of MAPLE to fabricate polymer films would probably increase drastically.

Interfacial modification to control film morphology includes several options that have more room for exploration. While Chapter 3 explored SAMs that increased the WF of the ITO substrates (in essence only probing the highest occupied molecular orbital (HOMO) level of P3HT), SAM-modification that allows for the probing of the lowest unoccupied molecular orbital (LUMO) level of P3HT would be quite interesting. It has been previously seen that the DOS width of the tail states at the HOMO and LUMO levels of conjugated polymers can be different, so understanding if SAM-modification alters film morphology that further influences the energetic disorder at the LUMO level would add to the current picture. There also exists a bounty of SAMs that can be used to modify substrates, allowing for continued examination of

whether or not surface energy of the substrate influences thin film morphology, and thus thin film electronic structure. Finally, the study of how interfacial interactions influence thin film morphology with the measurement of surface potential (as discussed in Chapter 5) is still very much in its infancy. There is much work to be done to assess whether (1) the strength of interfacial interactions (strong versus weak) affects all polymer chains near the interface in terms of structure and (2) the surface potential measured can afford information about the polymer chains and structure.

Appendices

Appendix A. KFPM Schematic

Reproduced with permission from Wenderott, J. K..; Green, P. F. Self-Assembled Monolayers at the Conjugated Polymer/Electrode Interface: Implications for Charge Transport and Band-Bending Behavior. *ACS Applied Materials & Interfaces.* **2018**, DOI: 10.1021/acsami.8b03624. Copyright 2018 American Chemical Society.

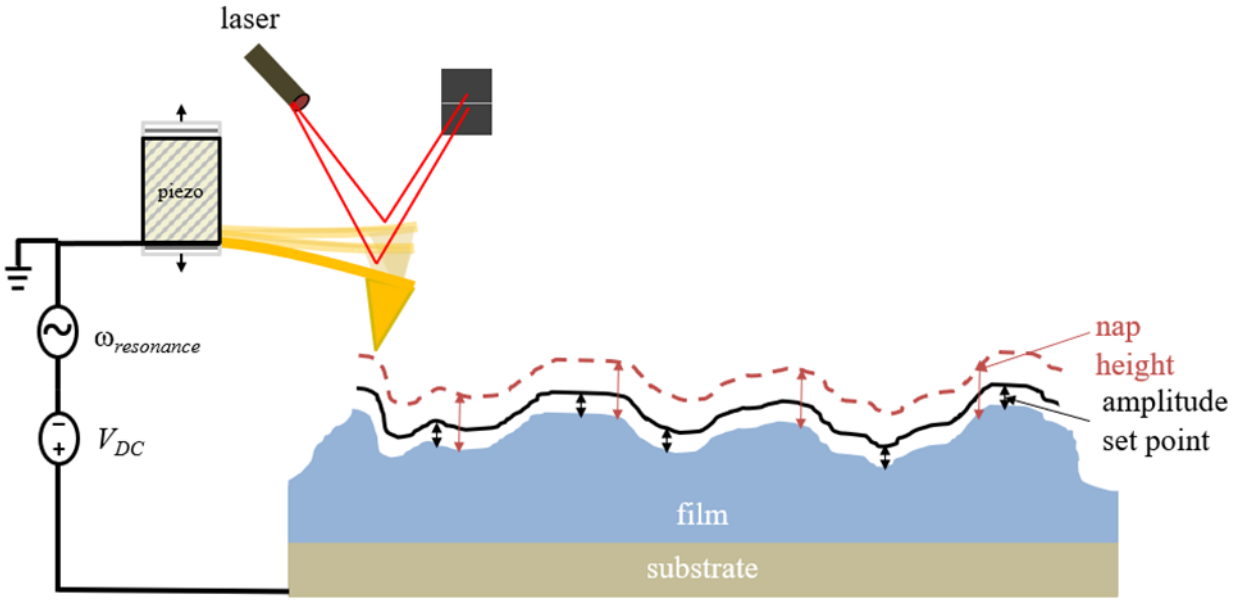

Figure A- 1. KPFM Schematic.

Appendix B. FTS and OTS Structures and Characterization of SAMs

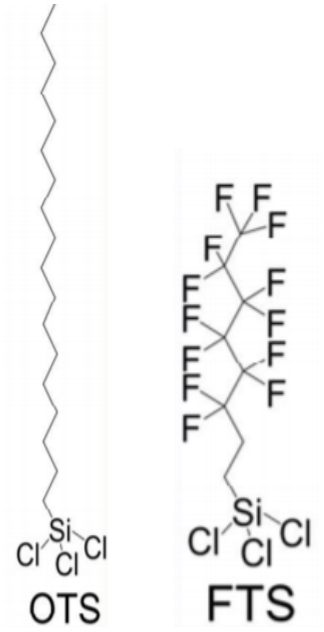

Figure A- 2. FTS and OTS chemical structures.

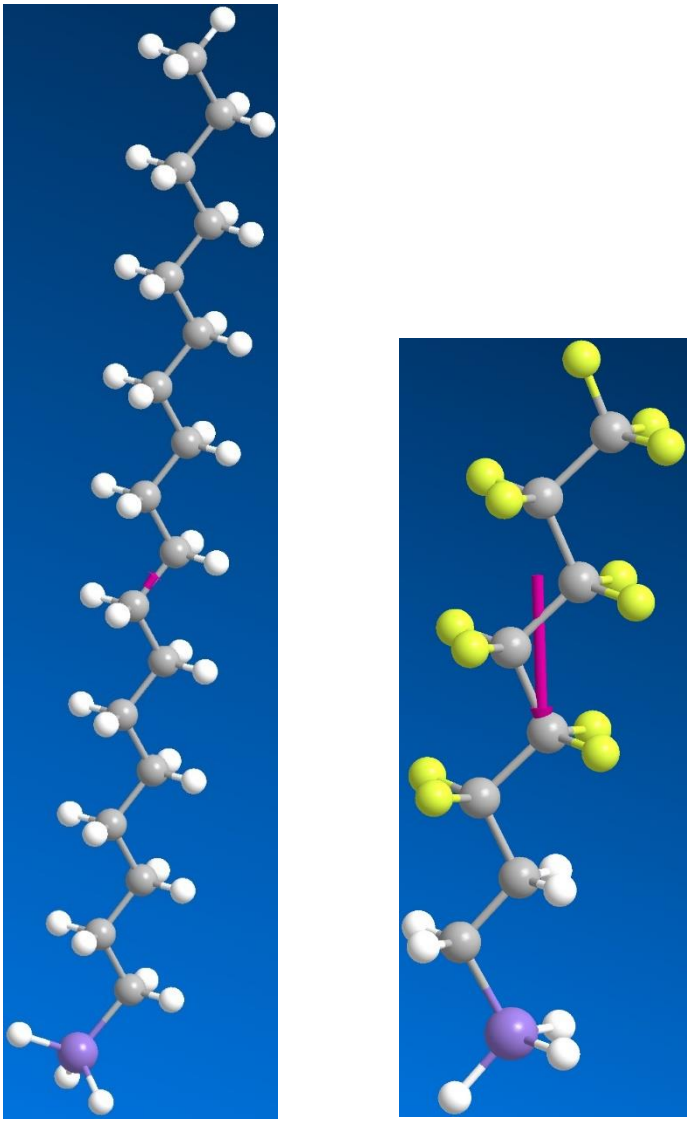

Figure A- 3. OTS (left) and FTS (right) molecules with calculated dipole moments. The magnitude and direction of the dipole moments are designated by the pink arrows.

Sample	**V_{SAM} (V)**	**Φ_{sub}- Φ_{tip} (V)**	**μ_{SAM} (C*m)**	**μ_{SAM} (D)**
FTS	-1.265	0.109	-8.9×10^{-30}	-2.67
OTS	-0.391	0.109	-2.2×10^{-30}	-0.65

Table A- 1. Values used to calculate dipole moments for FTS and OTS from KPFM surface potential maps.

Characterization of the Self-Assembled Monolayers (SAMs)

The quality of the SAMs are important for the validity of the experiments contained within the manuscript. Several methods to test and confirm the SAMs had successfully adhered to the indium tin oxide (ITO) surface's hydroxyl groups via chemical bonding were available. First, we used the surface potential value measured from Kelvin probe force microscopy (KPFM) of the SAM/ITO substrate to determine experimentally the dipole moment of the SAM and compared this with a calculated dipole moment of model molecules using Chem3D Ultra with the MOPAC interface. KPFM has been utilized to investigate organized molecular systems previously in a number of reports.[183,189,190] The surface potential, as measured by KPFM, of a SAM on a substrate is given by:

$$V_{SAM} = \frac{-(\varphi_{sub} - \varphi_{tip})}{e} + \frac{\mu}{A\varepsilon_{SAM}\varepsilon_0} + \alpha \qquad \text{(A.1)}$$

where φ_{sub} and φ_{tip} work functions of the substrate supporting the SAM and the tip, respectively, e is the elementary charge, μ is the net dipole moment directed normal to the substrate surface, A is the area occupied by each molecule, and ε_{SAM} and $\varepsilon_0 = 8.85 \times 10^{-12}\ C^2/N\ m^2$ are the permittivity of the SAM and free air, respectively, and α is additional trapped charges that can contribute to the surface potential. This equation is adapted from Sugimura, *et al.*[189], and points to the contributions to the surface potential from several sources: (1) the contact potential difference (CPD) between the tip and substrate, (2) the dipole moment of the SAM derived from the Helmholtz equation, and (3) trapped charges in oxide layers or other sources that add to the potential. In our case, there is no thick oxide layer, so the α term is assumed negligible. For simplicity, we assume both OTS and FTS have similar A and ε_{SAM}, though there will be some discrepancy between the two. The values chosen are $A = 3 \times 10^{-19} m^2$ and $\varepsilon_{SAM} = 2.9$ based on other studies.[190,191]

Table S1 shows the values used and dipole moments directed normal calculated from equation (1). We find experimentally $\mu_{OTS} = -0.65\ D$ and $\mu_{FTS} = -2.67\ D$ from KPFM. Calculated dipole moments of model molecules using Chem3D Ultra were found to be $\mu_{OTS} = 0.39\ D$ and $\mu_{FTS} = -2.84\ D$ and are shown in Figure S2. We take particular note of the experimental value of the OTS dipole moment oriented in the opposite direction of the model molecule dipole moment. This finding indicates the OTS SAM is not as close to its model orientation as the FTS SAM, which only deviates slightly from its model orientation. Both methods point to a small dipole moment for OTS and one that is smaller than that of FTS, though, which is lends support for a quality SAM on top of ITO. Deviations from the model for both FTS and OTS could arise from the fact that ITO is a fairly rough substrate as compared to pristine Si/SiO_x and the values used for calculating the experimental dipole moments (A and ε_{SAM}) were not precise.

Another verification for the quality of the SAM comes from the surface energy measurements. It has been previously shown, and is intuitive from the molecular structures, that both OTS and FTS are hydrophobic.[192,193] In our contact angle measurements using water, we measured average contact angles of $\Theta_{H20,\ OTS} = 102.6° \pm 1.4°$ and $\Theta_{H20,\ FTS} = 104.2° \pm 1.4°$, which further confirms the quality of the SAM. We measured contact angle of water over several areas on the substrate, showing the SAM does have coverage across the substrate. The small variation in the contact angles measured also shows this coverage is fairly uniform, with minor deviations in quality perhaps again due to the ITO substrate roughness.

Appendix C. Fits for Band-Bending Data of Spin-cast P3HT on FTS/ITO, OTS/ITO, Bare ITO

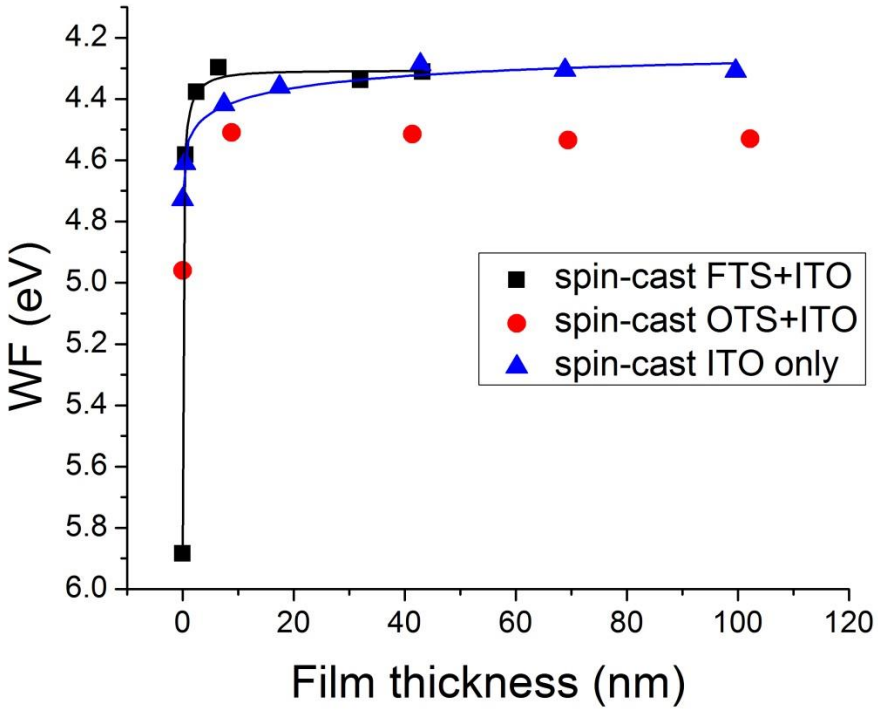

Figure A- 4. Band-bending data for spin-cast samples and fits to data.

Appendix D. Raw CELIV Data of MAPLE-Deposited P3HT on FTS/ITO and OTS/ITO

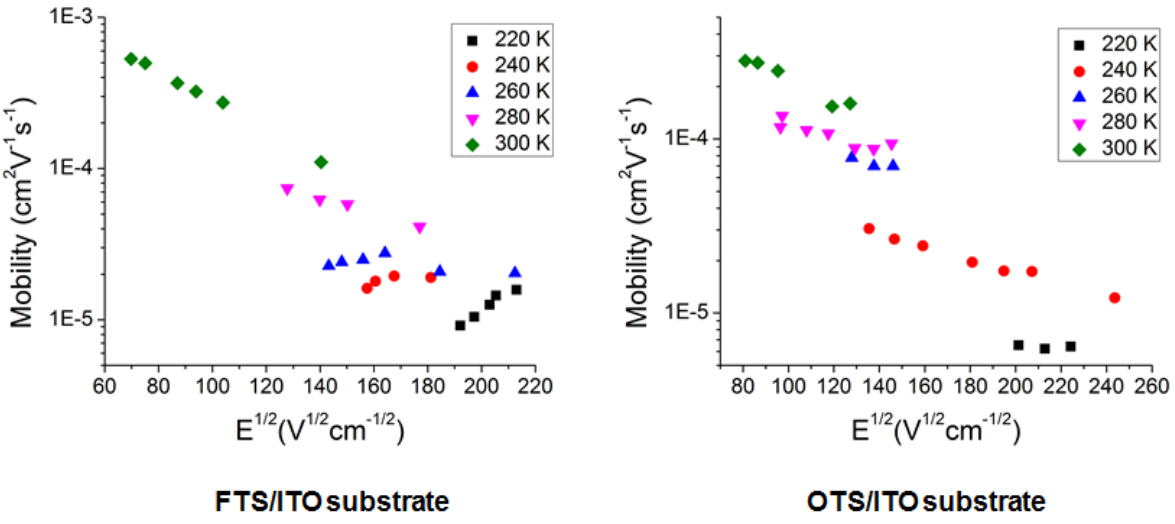

Figure A- 5. Raw CELIV data of MAPLE-deposited P3HT on FTS/ITO and OTS/ITO.

Appendix E. UV Absorption Spectra of MBI Films Before and After Solvent Annealing

Reproduced with permission from Wenderott, J. K.; Raghav, A.; Shtein, M.; Green, P. F.; Satapathi, S. Local Optoelectronic Characterization of Solvent-Annealed, Lead-Free, Bismuth-Based Perovskite Films. *Langmuir*. **2018**, DOI: 10.1021/acs.langmuir.8b01003. Copyright 2018 American Chemical Society.

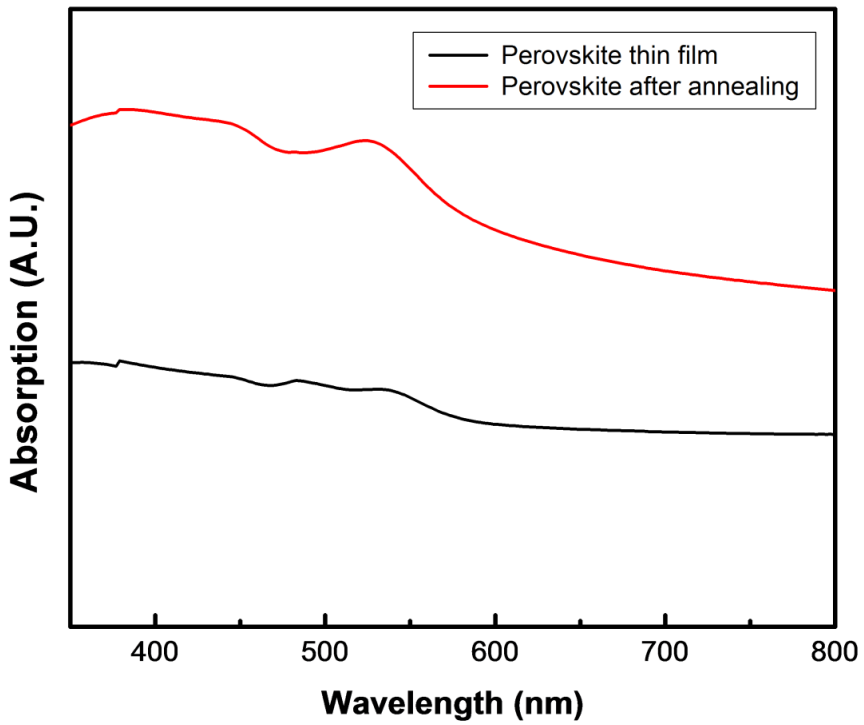

Figure A- 6. Increased band-edge absorption is seen in MBI films after solvent annealing.

Appendix F. Energy Dispersive X-ray Analysis of Perovskite Material After Solvent Annealing

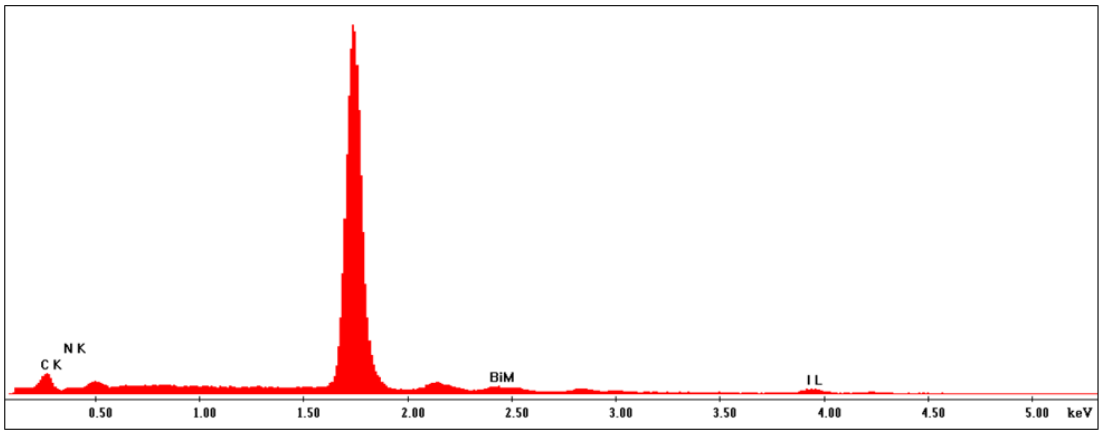

Element	Wt%	At%
CK	13.06	56.99
NL	3.16	11.84
BiM	21.22	5.32
IM	62.56	25.84
Total	100	100

Figure A- 7. EDAX analysis of solvent-annealed MBI film.

Appendix G. Compositional Mapping of Perovskite Material After Solvent Annealing

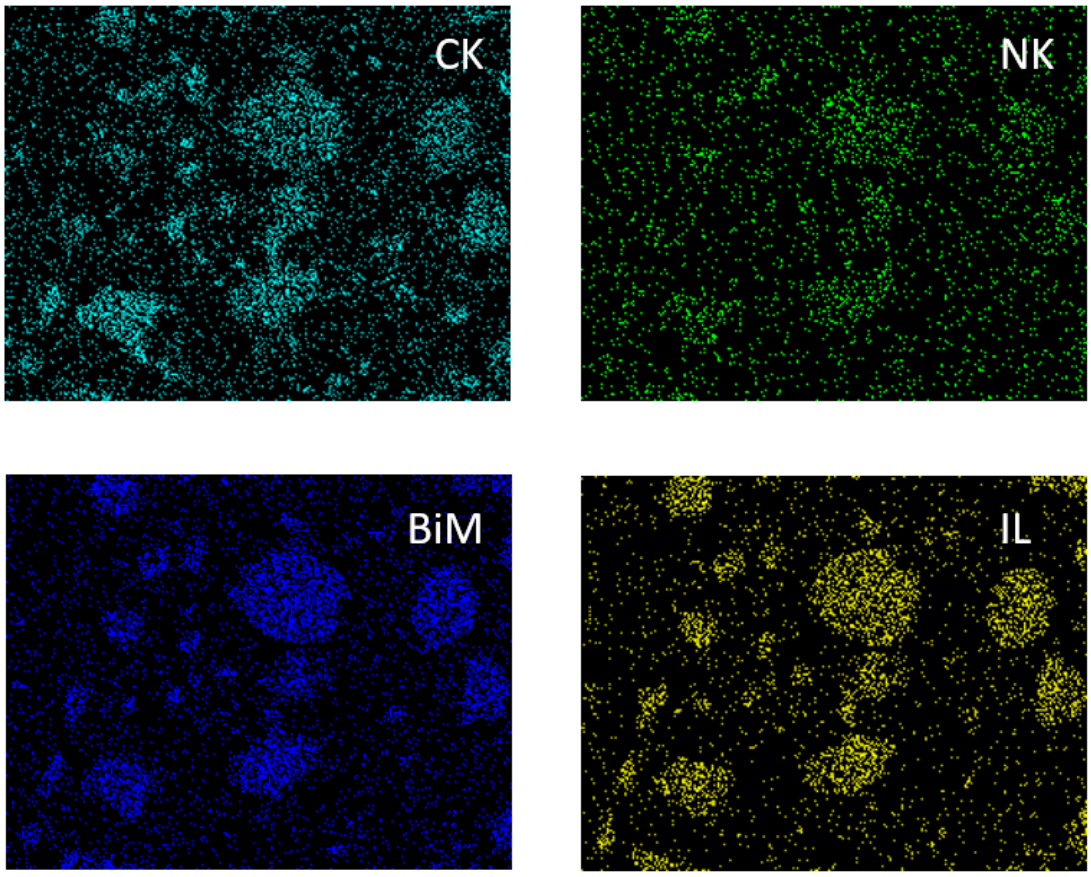

Figure A- 8. Compositional mapping of solvent-annealed MBI film.

Appendix H. J-V Curves of Devices Containing Thermally and Solvent-Annealed MBI Films

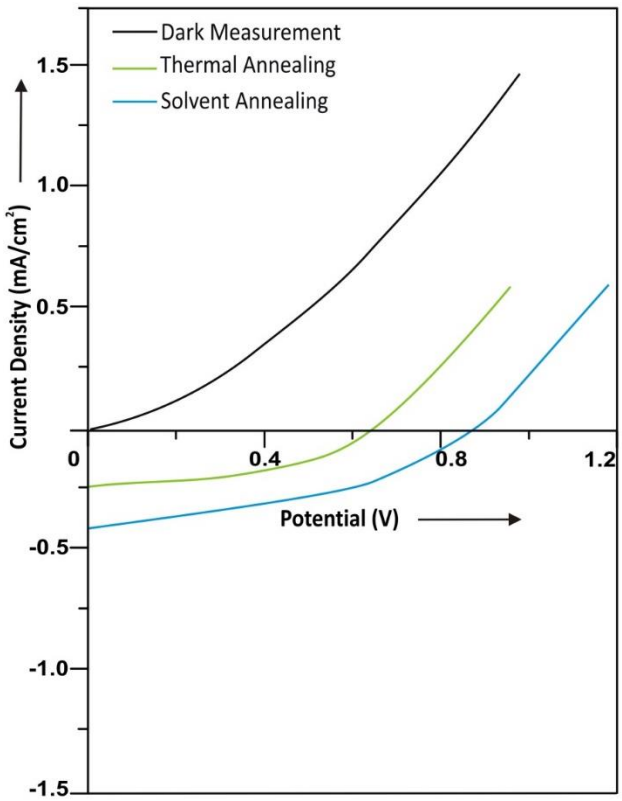

Figure A- 9. J-V cures of devices containing solvent-annealed and thermally annealed MBI films.

Appendix I. KPFM Control Studies on Bi:Sn Alloy

Manuscript in preparation by Wenderott, J. K.; Dong, B. X.; Amonoo, J.; Green, P. F.

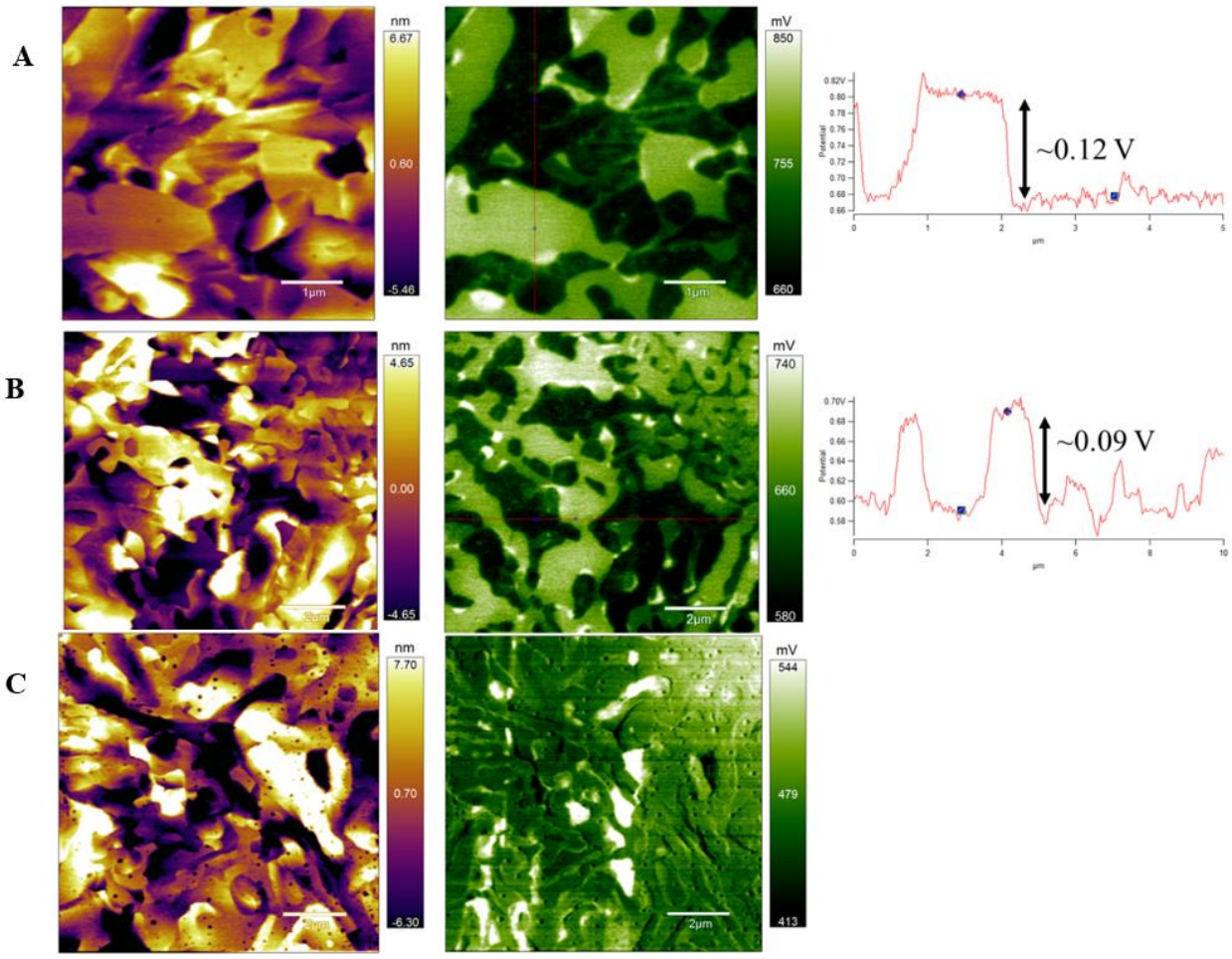

Figure A- 10. Topography and surface potential images of Bi/Sn alloy. 5x5 µm scan (A) and 10x10 µm scan (B) show relative surface potential differences between 0.08-0.13 V prior to oxidation. 5x5 µm scan (C) shows oxidation of Bi/Sn surface after being left in air for several hours.

Prior to oxidation and directly after removing the alloy from the Carver press, the values we measure for the CPD between Sn and Bi range from ~0.08-0.13 V. These values match well

with the cited CPD between Sn and Bi, which equals 0.08 V ± 0.05 V.[194] As seen below (A, B), the Bi and Sn segregate primarily into their own domains, which makes the alloy useful for a test of relative surface potential. Seen also below (C), after the alloy was left out for several hours in air, the difference in surface potential between Bi and Sn lessened and several spots of high surface potential appear. This has been attributed to oxidation of the sample, which is more apparent on Sn.[181]

There are a couple of additional observations to be made regarding the KPFM results from the model alloy study. By closely comparing the topography and surface potential, we see no consistent cross-talk between channels. Some features seen in the topography map seem to translate to features in surface potential, but clearly not all. Additionally, we can see our technique yields good lateral resolution, as seen in the contrast between domains of Bi and Sn.

Bibliography

(1) Mark, H. Macromolecules: Origin, Development, Significance. *Biophys. J.* **1964**, *4* (1, Part 2), 5–7.

(2) Bakelite First Synthetic Plastic - National Historic Chemical Landmark https://www.acs.org/content/acs/en/education/whatischemistry/landmarks/bakelite.html (accessed May 12, 2018).

(3) The Nobel Prize in Chemistry 1902 https://www.nobelprize.org/nobel_prizes/chemistry/laureates/1902/ (accessed May 12, 2018).

(4) Hildebrandt, G. The Discovery of the Diffraction of X-Rays in Crystals — A Historical Review. *Cryst. Res. Technol.* **1993**, *28* (6), 747–766.

(5) Bragg, W. H.; Bragg, W. L. The Reflection of X-Rays by Crystals. *Proc R Soc Lond A* **1913**, *88* (605), 428–438.

(6) Mandelkern, L. History of Crystalline Polymers. *J. Macromol. Sci. Part - Chem.* **1981**, *15* (6), 1211–1235.

(7) Flory, P. J. Thermodynamics of High Polymer Solutions. *J. Chem. Phys.* **1942**, *10* (1), 51–61.

(8) Huggins, M. L. Solutions of Long Chain Compounds. *J. Chem. Phys.* **1941**, *9* (5), 440–440.

(9) Kuhn, W. Über die Gestalt fadenförmiger Moleküle in Lösungen. *Kolloid-Z.* **1934**, *68* (1), 2–15.

(10) Rouse, P. E. A Theory of the Linear Viscoelastic Properties of Dilute Solutions of Coiling Polymers. *J. Chem. Phys.* **1953**, *21* (7), 1272–1280.

(11) Zimm, B. H. Dynamics of Polymer Molecules in Dilute Solution: Viscoelasticity, Flow Birefringence and Dielectric Loss. *J. Chem. Phys.* **1956**, *24* (2), 269–278.

(12) Gennes, P.-G. de; Gennes, P. P.-G. *Scaling Concepts in Polymer Physics*; Cornell University Press, 1979.

(13) Ott, E. Über die Molekülgröße von Kautschuk und Guttapercha. *Naturwissenschaften* **1926**, *14* (15), 320–320.

(14) Katz, J. R. Röntgenspektrographische Untersuchungen am gedehnten Kautschuk und ihre mögliche Bedeutung für das Problem der Dehnungseigenschaften dieser Substanz. *Naturwissenschaften* **1925**, *13* (19), 410–416.

(15) Dong, B. X.; Li, A.; Strzalka, J.; Stein, G. E.; Green, P. F. Molecular Organization in MAPLE-Deposited Conjugated Polymer Thin Films and the Implications for Carrier Transport Characteristics. *J. Polym. Sci. Part B Polym. Phys.* **2017**, *55* (1), 39–48.

(16) Erb, T.; Zhokhavets, U.; Gobsch, G.; Raleva, S.; Stühn, B.; Schilinsky, P.; Waldauf, C.; Brabec, C. J. Correlation Between Structural and Optical Properties of Composite

Polymer/Fullerene Films for Organic Solar Cells. *Adv. Funct. Mater.* **2005**, *15* (7), 1193–1196.
(17) Hill, A. J.; Tant, M. R. The Structure and Properties of Glassy Polymers: An Overview. In *Structure and Properties of Glassy Polymers*; Tant, M. R., Hill, A. J., Eds.; American Chemical Society: Washington, DC, 1999; Vol. 710, pp 1–20.
(18) Schönhals, A.; Kremer, F. Broadband Dielectric Measurement Techniques (10-6 Hz to 1012 Hz). In *Broadband Dielectric Spectroscopy*; Kremer, F., Schönhals, A., Eds.; Springer Berlin Heidelberg, 2003; pp 35–57.
(19) Sharma, R. P.; Green, P. F. Component Dynamics in Polymer/Polymer Blends: Role of Spatial Compositional Heterogeneity. *Macromolecules* **2017**, *50* (17), 6617–6630.
(20) Huang, B.; Glynos, E.; Frieberg, B.; Yang, H.; Green, P. F. Effect of Thickness-Dependent Microstructure on the Out-of-Plane Hole Mobility in Poly(3-Hexylthiophene) Films. *ACS Appl. Mater. Interfaces* **2012**, *4* (10), 5204–5210.
(21) Khulbe, K. C.; Matsuura, T.; Lamarche, G.; Kim, H. J. The Morphology Characterisation and Performance of Dense PPO Membranes for Gas Separation. *J. Membr. Sci.* **1997**, *135* (2), 211–223.
(22) Stafford, C. M.; Vogt, B. D.; Harrison, C.; Julthongpiput, D.; Huang, R. Elastic Moduli of Ultrathin Amorphous Polymer Films. *Macromolecules* **2006**, *39* (15), 5095–5099.
(23) Prabu, A. A.; Kim, K. J.; Park, C. Effect of Thickness on the Crystallinity and Curie Transition Behavior in P(VDF/TrFE) (72/28) Copolymer Thin Films Using FTIR-Transmission Spectroscopy. *Vib. Spectrosc.* **2009**, *49* (2), 101–109.
(24) Huang, B.; Glynos, E.; Frieberg, B.; Yang, H.; Green, P. F. Effect of Thickness-Dependent Microstructure on the Out-of-Plane Hole Mobility in Poly(3-Hexylthiophene) Films. *ACS Appl. Mater. Interfaces* **2012**, *4* (10), 5204–5210.
(25) Hanakata, P. Z.; Douglas, J. F.; Starr, F. W. Local Variation of Fragility and Glass Transition Temperature of Ultra-Thin Supported Polymer Films. *J. Chem. Phys.* **2012**, *137* (24), 244901.
(26) Yelash, L.; Virnau, P.; Binder, K.; Paul, W. Three-Step Decay of Time Correlations at Polymer-Solid Interfaces. *EPL Europhys. Lett.* **2012**, *98* (2), 28006.
(27) Varnik, F.; Baschnagel, J.; Binder, K. Glassy Dynamics in Thin Polymer Films: Recent MD Results. *J. Non-Cryst. Solids* **2002**, *307–310* (Supplement C), 524–531.
(28) Solar, M.; Mapesa, E. U.; Kremer, F.; Binder, K.; Paul, W. The Dielectric α -Relaxation in Polymer Films: A Comparison between Experiments and Atomistic Simulations. *EPL Europhys. Lett.* **2013**, *104* (6), 66004.
(29) Yelash, L.; Virnau, P.; Binder, K.; Paul, W. Slow Process in Confined Polymer Melts: Layer Exchange Dynamics at a Polymer Solid Interface. *Phys. Rev. E Stat. Nonlin. Soft Matter Phys.* **2010**, *82* (5 Pt 1), 050801.
(30) DeFelice, J.; Milner, S. T.; Lipson, J. E. G. Simulating Local Tg Reporting Layers in Glassy Thin Films. *Macromolecules* **2016**, *49* (5), 1822–1833.
(31) Tito, N. B.; Lipson, J. E. G.; Milner, S. T. Lattice Model of Dynamic Heterogeneity and Kinetic Arrest in Glass-Forming Liquids. *Soft Matter* **2013**, *9* (11), 3173–3180.
(32) Lin, F.-Y.; Steffen, W. Capillary Wave Dynamics of Thin Liquid Polymer Films. *J. Chem. Phys.* **2014**, *141* (10), 104903.
(33) Peter, S.; Meyer, H.; Baschnagel, J. Thickness-Dependent Reduction of the Glass-Transition Temperature in Thin Polymer Films with a Free Surface. *J. Polym. Sci. Part B Polym. Phys.* **2006**, *44* (20), 2951–2967.

(34) Dalnoki-Veress, K.; Forrest, J.; G De Gennes, P.; Dutcher, J. Glass Transition Reductions in Thin Freely-Standing Polymer Films: A Scaling Analysis of Chain Confinement Effects. *J. Phys. IV Proc.* **2000**, *10*, Pr7-221.
(35) Roth, C. B.; Dutcher, J. R. Glass Transition Temperature of Freely-Standing Films of Atactic Poly(Methyl Methacrylate). *Eur. Phys. J. E* **2003**, *12*, 103–107.
(36) Wang, J.; McKenna, G. B. Viscoelastic and Glass Transition Properties of Ultrathin Polystyrene Films by Dewetting from Liquid Glycerol. *Macromolecules* **2013**, *46* (6), 2485–2495.
(37) Ellison, C. J.; Torkelson, J. M. The Distribution of Glass-Transition Temperatures in Nanoscopically Confined Glass Formers. *Nat. Mater.* **2003**, *2* (10), 695–700.
(38) Forrest, J. A. Effect of Free Surfaces on the Glass Transition Temperature of Thin Polymer Films. *Phys. Rev. Lett.* **1996**, *77* (10), 2002–2005.
(39) Keddie, J. L.; Jones, R. A. L.; Cory, R. A. Size-Dependent Depression of the Glass Transition Temperature in Polymer Films. *EPL Europhys. Lett.* **1994**, *27* (1), 59.
(40) Boucher, V. M.; Cangialosi, D.; Yin, H.; Schönhals, A.; Alegría, A.; Colmenero, J. Tg Depression and Invariant Segmental Dynamics in Polystyrene Thin Films. *Soft Matter* **2012**, *8*, 5119.
(41) Forrest, J. A.; Dalnoki-Veress, K. The Glass Transition in Thin Polymer Films. *Adv. Colloid Interface Sci.* **2001**, *94* (1–3), 167–195.
(42) Fukao, K. Glass Transitions and Dynamics in Thin Polymer Films: Dielectric Relaxation of Thin Films of Polystyrene. *Phys. Rev. E* **2000**, *61* (2), 1743–1754.
(43) Priestley, R. D.; Broadbelt, L. J.; Torkelson, J. M.; Fukao, K. Glass Transition and $\ensuremath{\alpha}$-Relaxation Dynamics of Thin Films of Labeled Polystyrene. *Phys. Rev. E* **2007**, *75* (6), 061806.
(44) Yin, H.; Napolitano, S.; Schönhals, A. Molecular Mobility and Glass Transition of Thin Films of Poly(Bisphenol A Carbonate). *Macromolecules* **2012**, *45* (3), 1652–1662.
(45) Mirigian, S.; Schweizer, K. S. Communication: Slow Relaxation, Spatial Mobility Gradients, and Vitrification in Confined Films. *J. Chem. Phys.* **2014**, *141* (16), 161103.
(46) Hsu, D. D.; Xia, W.; Song, J.; Keten, S. Glass-Transition and Side-Chain Dynamics in Thin Films: Explaining Dissimilar Free Surface Effects for Polystyrene vs Poly(Methyl Methacrylate). *ACS Macro Lett.* **2016**, *5* (4), 481–486.
(47) Lupaşcu, V.; Picken, S. J.; Wübbenhorst, M. Cooperative and Non-Cooperative Dynamics in Ultra-Thin Films of Polystyrene Studied by Dielectric Spectroscopy and Capacitive Dilatometry. *J. Non-Cryst. Solids* **2006**, *352* (52–54), 5594–5600.
(48) Kipnusu, W. K.; Elmahdy, M. M.; Tress, M.; Fuchs, M.; Mapesa, E. U.; Smilgies, D.-M.; Zhang, J.; Papadakis, C. M.; Kremer, F. Molecular Order and Dynamics of Nanometric Thin Layers of Poly(Styrene-b-1,4-Isoprene) Diblock Copolymers. *Macromolecules* **2013**, *46* (24), 9729–9737.
(49) Mapesa, E. U.; Tress, M.; Schulz, G.; Huth, H.; Schick, C.; Reiche, M.; Kremer, F. Segmental and Chain Dynamics in Nanometric Layers of Poly(Cis-1,4-Isoprene) as Studied by Broadband Dielectric Spectroscopy and Temperature-Modulated Calorimetry. *Soft Matter* **2013**, *9* (44), 10592–10598.
(50) Kremer, F.; Tress, M.; Mapesa, E. U. Glassy Dynamics and Glass Transition in Nanometric Layers and Films: A Silver Lining on the Horizon. *J. Non-Cryst. Solids* **2015**, *407*, 277–283.

(51) Priestley, R. D.; Cangialosi, D.; Napolitano, S. On the Equivalence between the Thermodynamic and Dynamic Measurements of the Glass Transition in Confined Polymers. *J. Non-Cryst. Solids* **2015**, *407*, 288–295.
(52) Ediger, M. D.; Forrest, J. A. Dynamics near Free Surfaces and the Glass Transition in Thin Polymer Films: A View to the Future. *Macromolecules* **2014**, *47* (2), 471–478.
(53) Bao, Z.; Dodabalapur, A.; Lovinger, A. J. Soluble and Processable Regioregular Poly(3-hexylthiophene) for Thin Film Field-effect Transistor Applications with High Mobility. *Appl. Phys. Lett.* **1996**, *69* (26), 4108–4110.
(54) McCulloch, I.; Heeney, M.; Bailey, C.; Genevicius, K.; MacDonald, I.; Shkunov, M.; Sparrowe, D.; Tierney, S.; Wagner, R.; Zhang, W.; et al. Liquid-Crystalline Semiconducting Polymers with High Charge-Carrier Mobility. *Nat. Mater.* **2006**, *5* (4), 328–333.
(55) Noriega, R.; Rivnay, J.; Vandewal, K.; Koch, F. P. V.; Stingelin, N.; Smith, P.; Toney, M. F.; Salleo, A. A General Relationship between Disorder, Aggregation and Charge Transport in Conjugated Polymers. *Nat. Mater.* **2013**, *12* (11), 1038–1044.
(56) Kline, R. J.; McGehee, M. D. Morphology and Charge Transport in Conjugated Polymers. *J. Macromol. Sci. Part C* **2006**, *46* (1), 27–45.
(57) Himmelberger, S.; Salleo, A. Engineering Semiconducting Polymers for Efficient Charge Transport. *MRS Commun.* **2015**, *5* (3), 383–395.
(58) Bässler, H. Charge Transport in Disordered Organic Photoconductors a Monte Carlo Simulation Study. *Phys. Status Solidi B* **1993**, *175* (1), 15–56.
(59) Bässler, H.; Köhler, A. Charge Transport in Organic Semiconductors. In *Unimolecular and Supramolecular Electronics I*; Metzger, R. M., Ed.; Topics in Current Chemistry; Springer Berlin Heidelberg, 2011; pp 1–65.
(60) Noriega, R.; Salleo, A.; Spakowitz, A. J. Chain Conformations Dictate Multiscale Charge Transport Phenomena in Disordered Semiconducting Polymers. *Proc. Natl. Acad. Sci.* **2013**, *110* (41), 16315–16320.
(61) Bässler, H.; Borsenberger, P. M.; Perry, R. J. Charge Transport in Poly(Methylphenylsilane): The Case for Superimposed Disorder and Polaron Effects. *J. Polym. Sci. Part B Polym. Phys.* **1994**, *32* (9), 1677–1685.
(62) Lange, I.; Blakesley, J. C.; Frisch, J.; Vollmer, A.; Koch, N.; Neher, D. Band Bending in Conjugated Polymer Layers. *Phys Rev Lett* **2011**, *106* (21), 216402.
(63) Braun, S.; Salaneck, W. R.; Fahlman, M. Energy-Level Alignment at Organic/Metal and Organic/Organic Interfaces. *Adv. Mater.* **2009**, *21* (14–15), 1450–1472.
(64) Nishi, T.; Kanai, K.; Ouchi, Y.; Willis, M. R.; Seki, K. Evidence for the Atmospheric P-Type Doping of Titanyl Phthalocyanine Thin Film by Oxygen Observed as the Change of Interfacial Electronic Structure. *Chem. Phys. Lett.* **2005**, *414* (4–6), 479–482.
(65) Dong, B. X.; Amonoo, J. A.; Purdum, G. E.; Loo, Y.-L.; Green, P. F. Enhancing Carrier Mobilities in Organic Thin-Film Transistors Through Morphological Changes at the Semiconductor/Dielectric Interface Using Supercritical Carbon Dioxide Processing http://pubs.acs.org/doi/suppl/10.1021/acsami.6b08248 (accessed Nov 17, 2016).
(66) Wenderott, J. K.; Dong, B. X.; Green, P. F. Band Bending in Conjugated Polymer Films: Role of Morphology and Implications for Bulk Charge Transport Characteristics. *J. Mater. Chem. C* **2017**, *5* (30), 7446–7451.

(67) Hwang, J.; Kim, E.-G.; Liu, J.; Brédas, J.-L.; Duggal, A.; Kahn, A. Photoelectron Spectroscopic Study of the Electronic Band Structure of Polyfluorene and Fluorene-Arylamine Copolymers at Interfaces. *J. Phys. Chem. C* **2007**, *111* (3), 1378–1384.
(68) Ishii, H.; Hayashi, N.; Ito, E.; Washizu, Y.; Sugi, K.; Kimura, Y.; Niwano, M.; Ouchi, Y.; Seki, K. Kelvin Probe Study of Band Bending at Organic Semiconductor/Metal Interfaces: Examination of Fermi Level Alignment. *Phys. Status Solidi A* **2004**, *201* (6), 1075–1094.
(69) Schlaf, R.; Schroeder, P. G.; Nelson, M. W.; Parkinson, B. A.; Lee, P. A.; Nebesny, K. W.; Armstrong, N. R. Observation of Strong Band Bending in Perylene Tetracarboxylic Dianhydride Thin Films Grown on SnS2. *J. Appl. Phys.* **1999**, *86* (3), 1499–1509.
(70) Zhang, Z.; Yates, J. T. Band Bending in Semiconductors: Chemical and Physical Consequences at Surfaces and Interfaces. *Chem. Rev.* **2012**, *112* (10), 5520–5551.
(71) Oehzelt, M.; Koch, N.; Heimel, G. Organic Semiconductor Density of States Controls the Energy Level Alignment at Electrode Interfaces. *Nat. Commun.* **2014**, *5*, 4174.
(72) Heimel, G.; Salzmann, I.; Duhm, S.; Rabe, J. P.; Koch, N. Intrinsic Surface Dipoles Control the Energy Levels of Conjugated Polymers. *Adv. Funct. Mater.* **2009**, *19* (24), 3874–3879.
(73) Fabiano, S.; Yoshida, H.; Chen, Z.; Facchetti, A.; Loi, M. A. Orientation-Dependent Electronic Structures and Charge Transport Mechanisms in Ultrathin Polymeric n-Channel Field-Effect Transistors. *ACS Appl. Mater. Interfaces* **2013**, *5* (10), 4417–4422.
(74) Dong, B. X.; Huang, B.; Tan, A.; Green, P. F. Nanoscale Orientation Effects on Carrier Transport in a Low-Band-Gap Polymer. *J. Phys. Chem. C* **2014**, *118* (31), 17490–17498.
(75) McCormick, R. D.; Lenhardt, J.; Stiff-Roberts, A. D. Effects of Emulsion-Based Resonant Infrared Matrix Assisted Pulsed Laser Evaporation (RIR-MAPLE) on the Molecular Weight of Polymers. *Polymers* **2012**, *4* (1), 341–354.
(76) Juška, G.; Arlauskas, K.; Viliūnas, M.; Kočka, J. Extraction Current Transients: New Method of Study of Charge Transport in Microcrystalline Silicon. *Phys. Rev. Lett.* **2000**, *84* (21), 4946–4949.
(77) Li, A.; Dong, B. X.; Green, P. F. Influence of Morphological Disorder on In- and out-of-Plane Charge Transport in Conjugated Polymer Films. *MRS Commun.* **2015**, *5* (4), 593–598.
(78) Shepard, K. B.; Arnold, C. B.; Priestley, R. D. Transport and Stability of Laser-Deposited Amorphous Polymer Nanoglobules. *ACS Macro Lett.* **2014**, *3* (10), 1046–1050.
(79) Leveugle, E.; Zhigilei, L. V. Molecular Dynamics Simulation Study of the Ejection and Transport of Polymer Molecules in Matrix-Assisted Pulsed Laser Evaporation. *J. Appl. Phys.* **2007**, *102* (7), 074914.
(80) Liscio, A.; Palermo, V.; Fenwick, O.; Braun, S.; Müllen, K.; Fahlman, M.; Cacialli, F.; Samorí, P. Local Surface Potential of π-Conjugated Nanostructures by Kelvin Probe Force Microscopy: Effect of the Sampling Depth. *Small* **2011**, *7* (5), 634–639.
(81) Melitz, W.; Shen, J.; Kummel, A. C.; Lee, S. Kelvin Probe Force Microscopy and Its Application. *Surf. Sci. Rep.* **2011**, *66* (1), 1–27.
(82) Whitcher, T. J.; Wong, W. S.; Talik, A. N.; Woon, K. L.; Chanlek, N.; Nakajima, H.; Saisopa, T.; Songsiriritthigul, P. Investigation into the Gaussian Density of States Widths of Organic Semiconductors. *J. Phys. Appl. Phys.* **2016**, *49* (32), 325106.

(83) Whitcher, T. J.; Wong, W. S.; Talik, A. N.; Woon, K. L.; Chanlek, N.; Nakajima, H.; Saisopa, T.; Songsiriritthigul, P. Electrostatic Model of the Energy-Bending within Organic Semiconductors: Experiment and Simulation. *J. Phys. Condens. Matter* **2016**, *28* (36), 365002.
(84) Coehoorn, R.; Bobbert, P. A. Effects of Gaussian Disorder on Charge Carrier Transport and Recombination in Organic Semiconductors. *Phys. Status Solidi A* **2012**, *209* (12), 2354–2377.
(85) Dieckmann, A.; Bässler, H. An Assessment of the Role of Dipoles on the Density-of-states Function of Disordered Molecular Solids. *J. Chem. Phys.* **1993**, *99* (10), 8136–8141.
(86) Shi, X.-H.; Sun, J.-X.; Xiong, C.-H.; Sun, L. Exponential-Type Density of States with Clearly Cutting Tail for Organic Semiconductors. *Org. Electron.* **2016**, *30*, 60–66.
(87) Baranovskii, S. D. Theoretical Description of Charge Transport in Disordered Organic Semiconductors. *Phys. Status Solidi B* **2014**, *251* (3), 487–525.
(88) Tanase, C.; Meijer, E. J.; Blom, P. W. M.; de Leeuw, D. M. Unification of the Hole Transport in Polymeric Field-Effect Transistors and Light-Emitting Diodes. *Phys. Rev. Lett.* **2003**, *91* (21), 216601.
(89) Hoffmann, S. T.; Jaiser, F.; Hayer, A.; Bässler, H.; Unger, T.; Athanasopoulos, S.; Neher, D.; Köhler, A. How Do Disorder, Reorganization, and Localization Influence the Hole Mobility in Conjugated Copolymers? *J. Am. Chem. Soc.* **2013**, *135* (5), 1772–1782.
(90) Gartstein, Y. N.; Conwell, E. M. High-Field Hopping Mobility of Polarons in Disordered Molecular Solids. A Monte Carlo Study. *Chem. Phys. Lett.* **1994**, *217* (1), 41–47.
(91) Simonetti, O.; Giraudet, L.; Bugnot, D. Effective Mobility in Amorphous Organic Transistors: Influence of the Width of the Density of States. *Org. Electron.* **2014**, *15* (1), 35–39.
(92) Blakesley, J. C.; Neher, D. Relationship between Energetic Disorder and Open-Circuit Voltage in Bulk Heterojunction Organic Solar Cells. *Phys. Rev. B* **2011**, *84* (7), 075210.
(93) Wang, S.; Niu, D.; Lyu, L.; Huang, Y.; Wei, X.; Wang, C.; Xie, H.; Gao, Y. Interface Electronic Structure and Morphology of 2,7-Dioctyl[1]Benzothieno[3,2-b]Benzothiophene (C8-BTBT) on Au Film. *Appl. Surf. Sci.* **2017**, *416*, 696–703.
(94) Koch, N. Electronic Structure of Interfaces with Conjugated Organic Materials. *Phys. Status Solidi RRL – Rapid Res. Lett.* **2012**, *6* (7), 277–293.
(95) Moral, M.; Perez-Jimenez, A. J.; Sancho-Garcia, J. C. Understanding and Controlling Chemical Modifications of Rubicene for Their Envisioned Use as Molecular Organic Semiconductors. *J. Phys. Chem. C* **2017**, *121* (6), 3171–3181.
(96) Li, C. N.; Kwong, C. Y.; Djurišić, A. B.; Lai, P. T.; Chui, P. C.; Chan, W. K.; Liu, S. Y. Improved Performance of OLEDs with ITO Surface Treatments. *Thin Solid Films* **2005**, *477* (1), 57–62.
(97) Kim, J. S.; Cacialli, F. Increase of charge carriers density and reduction of Hall mobilities in oxygen-plasma treated indium–tin–oxide anodes: Applied Physics Letters: Vol 75, No 1 http://aip.scitation.org/doi/abs/10.1063/1.124263 (accessed Nov 11, 2017).
(98) Koh, S. E.; McDonald, K. D.; Holt, D. H.; Dulcey, C. S.; Chaney, J. A.; Pehrsson, P. E. Phenylphosphonic Acid Functionalization of Indium Tin Oxide: Surface Chemistry and Work Functions. *Langmuir* **2006**, *22* (14), 6249–6255.

(99) Sharma, A.; Hotchkiss, P. J.; Marder, S. R.; Kippelen, B. Tailoring the Work Function of Indium Tin Oxide Electrodes in Electrophosphorescent Organic Light-Emitting Diodes. *J. Appl. Phys.* **2009**, *105* (8), 084507.
(100) Hatton, R. A.; Day, S. R.; Chesters, M. A.; Willis, M. R. Organic Electroluminescent Devices: Enhanced Carrier Injection Using an Organosilane Self Assembled Monolayer (SAM) Derivatized ITO Electrode. *Thin Solid Films* **2001**, *394* (1), 291–296.
(101) Zehner, R. W.; Parsons, Bradley F.; Hsung, Richard P.; Sita, Lawrence R. Tuning the Work Function of Gold with Self-Assembled Monolayers Derived from X−[C6H4−C∶C−]nC6H4−SH (n = 0, 1, 2; X = H, F, CH3, CF3, and OCH3) - Langmuir (ACS Publications) http://pubs.acs.org/doi/abs/10.1021/la981114f (accessed Nov 11, 2017).
(102) Hsiao, C.-C.; Chang, C.-H.; Hung, M.-C.; Yang, N.-J.; Chen, S.-A. Self-Assembled Monolayer Modification of Indium Tin Oxide Anode Surface for Polymer Light-Emitting Diodes with Poly[2-Methoxy-5-(2-Ethylhexyloxy)-1,4-Phenylene Vinylene] for High Performance. *Appl. Phys. Lett.* **2005**, *86* (22), 223505.
(103) Wang, M.; Hill, I. G. Fluorinated Alkyl Phosphonic Acid SAMs Replace PEDOT:PSS in Polymer Semiconductor Devices. *Org. Electron.* **2012**, *13* (3), 498–505.
(104) Brown, T. M.; Kim, J. S.; Friend, R. H.; Cacialli, F.; Daik, R.; Feast, W. J. Built-in Field Electroabsorption Spectroscopy of Polymer Light-Emitting Diodes Incorporating a Doped Poly(3,4-Ethylene Dioxythiophene) Hole Injection Layer. *Appl. Phys. Lett.* **1999**, *75* (12), 1679–1681.
(105) de Jong, M. P.; van IJzendoorn, L. J.; de Voigt, M. J. A. Stability of the Interface between Indium-Tin-Oxide and Poly(3,4-Ethylenedioxythiophene)/Poly(Styrenesulfonate) in Polymer Light-Emitting Diodes. *Appl. Phys. Lett.* **2000**, *77* (14), 2255–2257.
(106) Yu, S.-Y.; Chang, J.-H.; Wang, P.-S.; Wu, C.-I.; Tao, Y.-T. Effect of ITO Surface Modification on the OLED Device Lifetime. *Langmuir ACS J. Surf. Colloids* **2014**, *30* (25), 7369–7376.
(107) Demirkan, K.; Mathew, A.; Weiland, C.; Yao, Y.; Rawlett, A. M.; Tour, J. M.; Opila, R. L. Energy Level Alignment at Organic Semiconductor/Metal Interfaces: Effect of Polar Self-Assembled Monolayers at the Interface. *J. Chem. Phys.* **2008**, *128* (7), 074705.
(108) Ge, W.; McCormick, R. D.; Nyikayaramba, G.; Stiff-Roberts, A. D. Bulk Heterojunction PCPDTBT:PC71BM Organic Solar Cells Deposited by Emulsion-Based, Resonant Infrared Matrix-Assisted Pulsed Laser Evaporation. *Appl. Phys. Lett.* **2014**, *104* (22), 223901.
(109) Pate, R.; Lantz, K. R.; Stiff-Roberts, A. D. Tabletop Resonant Infrared Matrix-Assisted Pulsed Laser Evaporation of Light-Emitting Organic Thin Films. *Ieee J. Sel. Top. Quantum Electron.* **2008**, *14* (4), 1022–1030.
(110) Ge, W.; Li, N. K.; McCormick, R. D.; Lichtenberg, E.; Yingling, Y. G.; Stiff-Roberts, A. D. Emulsion-Based RIR-MAPLE Deposition of Conjugated Polymers: Primary Solvent Effect and Its Implications on Organic Solar Cell Performance. *Acs Appl. Mater. Interfaces* **2016**, *8* (30), 19494–19506.
(111) Gutierrez-Llorente, A.; Horowitz, G.; Perez-Casero, R.; Perriere, J.; Fave, J. L.; Yassar, A.; Sant, C. Growth of Polyalkylthiophene Films by Matrix Assisted Pulsed Laser Evaporation. *Org. Electron.* **2004**, *5* (1–3), 29–34.

(112) Mariano, F.; Caricato, A. P.; Accorsi, G.; Leo, C.; Cesaria, M.; Carallo, S.; Genco, A.; Simeone, D.; Tunno, T.; Martino, M.; et al. White Multi-Layered Polymer Light Emitting Diode through Matrix Assisted Pulsed Laser Evaporation. *J. Mater. Chem. C* **2016**, *4* (32), 7667–7674.
(113) Caricato, A. P.; Cesaria, M.; Gigli, G.; Loiudice, A.; Luches, A.; Martino, M.; Resta, V.; Rizzo, A.; Taurino, A. Poly-(3-Hexylthiophene)/[6,6]-Phenyl-C-61-Butyric-Acid-Methyl-Ester Bilayer Deposition by Matrix-Assisted Pulsed Laser Evaporation for Organic Photovoltaic Applications. *Appl. Phys. Lett.* **2012**, *100* (7), 073306.
(114) Ge, W.; Atewologun, A.; Stiff-Roberts, A. D. Hybrid Nanocomposite Thin Films Deposited by Emulsion-Based Resonant Infrared Matrix-Assisted Pulsed Laser Evaporation for Photovoltaic Applications. *Org. Electron.* **2015**, *22*, 98–107.
(115) Dong, B. X.; Strzalka, J.; Jiang, Z.; Li, H.; Stein, G. E.; Green, P. F. Crystallization Mechanism and Charge Carrier Transport in MAPLE-Deposited Conjugated Polymer Thin Films. *ACS Appl. Mater. Interfaces* **2017**, *9* (51), 44799–44810.
(116) Stiff-Roberts, A. D.; Ge, W. Organic/Hybrid Thin Films Deposited by Matrix-Assisted Pulsed Laser Evaporation (MAPLE). *Appl. Phys. Rev.* **2017**, *4* (4), 041303.
(117) Bloisi, F.; Cassinese, A.; Papa, R.; Vicari, L.; Califano, V. Matrix-Assisted Pulsed Laser Evaporation of Polythiophene Films. *Thin Solid Films* **2008**, *516* (7), 1594–1598.
(118) Sugimura, H.; Ushiyama, K.; Hozumi, A.; Takai, O. Micropatterning of Alkyl- and Fluoroalkylsilane Self-Assembled Monolayers Using Vacuum Ultraviolet Light. *Langmuir* **2000**, *16* (3), 885–888.
(119) Hozumi, A.; Ushiyama, K.; Sugimura, H.; Takai, O. Fluoroalkylsilane Monolayers Formed by Chemical Vapor Surface Modification on Hydroxylated Oxide Surfaces. *Langmuir* **1999**, *15* (22), 7600–7604.
(120) Nonnenmacher, M.; O'Boyle, M. P.; Wickramasinghe, H. K. Kelvin Probe Force Microscopy. *Appl. Phys. Lett.* **1991**, *58* (25), 2921–2923.
(121) Fowkes, F. M. ATTRACTIVE FORCES AT INTERFACES. *Ind. Eng. Chem.* **1964**, *56* (12), 40–52.
(122) Xuan, D. B.; Mitchell, S.; Joseph, S.; Huanghe, L.; J, M. A.; E, S. G.; F, G. P. Molecular Weight Dependent Structure and Charge Transport in MAPLE-Deposited Poly(3-Hexylthiophene) Thin Films. *J. Polym. Sci. Part B Polym. Phys.* **2018**, *56* (8), 652–663.
(123) Yang, S. Y.; Shin, K.; Park, C. E. The Effect of Gate-Dielectric Surface Energy on Pentacene Morphology and Organic Field-Effect Transistor Characteristics. *Adv. Funct. Mater.* **2005**, *15* (11), 1806–1814.
(124) Palermo, V.; Samorì, P. Molecular Self-Assembly across Multiple Length Scales. *Angew. Chem. Int. Ed. 46* (24), 4428–4432.
(125) Reiter, G.; Gennes, P. G. de. Spin-Cast, Thin, Glassy Polymer Films: Highly Metastable Forms of Matter. *Eur. Phys. J. E* **2001**, *6* (1), 25–28.
(126) Zhang, H.; Zhang, L. Residual Stress in Spin-Cast Polyurethane Thin Films. *Appl. Phys. Lett.* **2015**, *106* (3), 033102.
(127) Liu, S.; Ma, X.; Wang, B.; Shang, X.; Wang, W.; Yu, X. Investigation of the Effect of Thermal Annealing on Poly(3-Hexylthiophene) Nanofibers by Scanning Probe Microscopy: From Single-Chain Conformation and Assembly Behavior to the Interfacial Interactions with Graphene Oxide. *ChemPhysChem* **2016**, *17* (20), 3315–3320.

(128) Verploegen, E.; Mondal, R.; Bettinger, C. J.; Sok, S.; Toney, M. F.; Bao, Z. Effects of Thermal Annealing Upon the Morphology of Polymer–Fullerene Blends. *Adv. Funct. Mater. 20* (20), 3519–3529.
(129) Li, G.; Shrotriya, V.; Huang, J.; Yao, Y.; Moriarty, T.; Emery, K.; Yang, Y. High-Efficiency Solution Processable Polymer Photovoltaic Cells by Self-Organization of Polymer Blends. *Nat. Mater.* **2005**, *4* (11), 864–868.
(130) Luca, G. D.; Treossi, E.; Liscio, A.; Mativetsky, J. M.; Scolaro, L. M.; Palermo, V.; Samorì, P. Solvent Vapour Annealing of Organic Thin Films: Controlling the Self-Assembly of Functional Systems across Multiple Length Scales. *J. Mater. Chem.* **2010**, *20* (13), 2493–2498.
(131) Vogelsang, J.; Lupton, J. M. Solvent Vapor Annealing of Single Conjugated Polymer Chains: Building Organic Optoelectronic Materials from the Bottom Up. *J. Phys. Chem. Lett.* **2012**, *3* (11), 1503–1513.
(132) Gregg, B. A. Evolution of Photophysical and Photovoltaic Properties of Perylene Bis(Phenethylimide) Films upon Solvent Vapor Annealing. *J. Phys. Chem.* **1996**, *100* (2), 852–859.
(133) Na, J. Y.; Kang, B.; Sin, D. H.; Cho, K.; Park, Y. D. Understanding Solidification of Polythiophene Thin Films during Spin-Coating: Effects of Spin-Coating Time and Processing Additives. *Sci. Rep.* **2015**, *5*, 13288.
(134) DeLongchamp, D. M.; Vogel, B. M.; Jung, Y.; Gurau, M. C.; Richter, C. A.; Kirillov, O. A.; Obrzut, J.; Fischer, D. A.; Sambasivan, S.; Richter, L. J.; et al. Variations in Semiconducting Polymer Microstructure and Hole Mobility with Spin-Coating Speed. *Chem. Mater.* **2005**, *17* (23), 5610–5612.
(135) Best Research-Cell Efficiencies https://www.nrel.gov/pv/assets/images/efficiency-chart.png (accessed Mar 9, 2017).
(136) Zhou, H.; Chen, Q.; Li, G.; Luo, S.; Song, T.; Duan, H.-S.; Hong, Z.; You, J.; Liu, Y.; Yang, Y. Interface Engineering of Highly Efficient Perovskite Solar Cells. *Science* **2014**, *345* (6196), 542–546.
(137) Noh, J. H.; Im, S. H.; Heo, J. H.; Mandal, T. N.; Seok, S. I. Chemical Management for Colorful, Efficient, and Stable Inorganic-Organic Hybrid Nanostructured Solar Cells. *Nano Lett.* **2013**, *13* (4), 1764–1769.
(138) Lee, M. M.; Teuscher, J.; Miyasaka, T.; Murakami, T. N.; Snaith, H. J. Efficient Hybrid Solar Cells Based on Meso-Superstructured Organometal Halide Perovskites. *Science* **2012**, *338* (6107), 643–647.
(139) Dong, Q.; Fang, Y.; Shao, Y.; Mulligan, P.; Qiu, J.; Cao, L.; Huang, J. Electron-Hole Diffusion Lengths > 175 Mm in Solution-Grown CH3NH3PbI3 Single Crystals. *Science* **2015**, *347* (6225), 967–970.
(140) Shi, D.; Adinolfi, V.; Comin, R.; Yuan, M.; Alarousu, E.; Buin, A.; Chen, Y.; Hoogland, S.; Rothenberger, A.; Katsiev, K.; et al. Low Trap-State Density and Long Carrier Diffusion in Organolead Trihalide Perovskite Single Crystals. *Science* **2015**, *347* (6221), 519–522.
(141) Stranks, S. D.; Eperon, G. E.; Grancini, G.; Menelaou, C.; Alcocer, M. J. P.; Leijtens, T.; Herz, L. M.; Petrozza, A.; Snaith, H. J. Electron-Hole Diffusion Lengths Exceeding 1 Micrometer in an Organometal Trihalide Perovskite Absorber. *Science* **2013**, *342* (6156), 341–344.

(142) Jeon, N. J.; Noh, J. H.; Yang, W. S.; Kim, Y. C.; Ryu, S.; Seo, J.; Seok, S. I. Compositional Engineering of Perovskite Materials for High-Performance Solar Cells. *Nature* **2015**, *517* (7535), 476–480.
(143) Green, M. A.; Emery, K.; Hishikawa, Y.; Warta, W.; Dunlop, E. D.; Levi, D. H.; Ho-Baillie, A. W. Y. Solar Cell Efficiency Tables (Version 49). *Prog. Photovolt. Res. Appl.* **2017**, *25* (1), 3–13.
(144) Simple Search | NSCEP | US EPA https://nepis.epa.gov/Exe/ZyNET.EXE?ZyActionL=Register&User=anonymous&Password=anonymous&Client=EPA&Init=1%3E%3Ctitle%3EEPA%20-%20Home%20Page%20for%20the%20Search%20site%3C/title%3E%3Clink%20rel= (accessed Apr 7, 2017).
(145) Ogomi, Y.; Morita, A.; Tsukamoto, S.; Saitho, T.; Fujikawa, N.; Shen, Q.; Toyoda, T.; Yoshino, K.; Pandey, S. S.; Ma, T.; et al. CH3NH3SnxPb(1–x)I3 Perovskite Solar Cells Covering up to 1060 Nm. *J. Phys. Chem. Lett.* **2014**, *5* (6), 1004–1011.
(146) Noel, N. K.; Stranks, S. D.; Abate, A.; Wehrenfennig, C.; Guarnera, S.; Haghighirad, A.-A.; Sadhanala, A.; Eperon, G. E.; Pathak, S. K.; Johnston, M. B.; et al. Lead-Free Organic–Inorganic Tin Halide Perovskites for Photovoltaic Applications. *Energy Environ. Sci.* **2014**, *7* (9), 3061–3068.
(147) Choi, T.; Lee, S.; Choi, Y. J.; Kiryukhin, V.; Cheong, S.-W. Switchable Ferroelectric Diode and Photovoltaic Effect in BiFeO3. *Science* **2009**, *324* (5923), 63–66.
(148) Chakrabartty, J. P.; Nechache, R.; Harnagea, C.; Rosei, F. Photovoltaic Effect in Multiphase Bi-Mn-O Thin Films. *Opt. Express* **2014**, *22* (101), A80–A89.
(149) Grinberg, I.; West, D. V.; Torres, M.; Gou, G.; Stein, D. M.; Wu, L.; Chen, G.; Gallo, E. M.; Akbashev, A. R.; Davies, P. K.; et al. Perovskite Oxides for Visible-Light-Absorbing Ferroelectric and Photovoltaic Materials. *Nature* **2013**, *503* (7477), 509–512.
(150) Yang, S. Y.; Martin, L. W.; Byrnes, S. J.; Conry, T. E.; Basu, S. R.; Paran, D.; Reichertz, L.; Ihlefeld, J.; Adamo, C.; Meville, A.; et al. Photovoltaic Effects in BiFeO3. *Appl. Phys. Lett.* **2009**, *95* (6), 062909.
(151) Brandt, R. E.; Kurchin, R. C.; Hoye, R. L. Z.; Poindexter, J. R.; Wilson, M. W. B.; Sulekar, S.; Lenahan, F.; Yen, P. X. T.; Stevanović, V.; Nino, J. C.; et al. Investigation of Bismuth Triiodide (BiI3) for Photovoltaic Applications. *J. Phys. Chem. Lett.* **2015**, *6* (21), 4297–4302.
(152) Singh, T.; Kulkarni, A.; Ikegami, M.; Miyasaka, T. Effect of Electron Transporting Layer on Bismuth-Based Lead-Free Perovskite (CH3NH3)3 Bi2I9 for Photovoltaic Applications. *ACS Appl. Mater. Interfaces* **2016**, *8* (23), 14542–14547.
(153) Lyu, M.; Yun, J.-H.; Cai, M.; Jiao, Y.; Bernhardt, P. V.; Zhang, M.; Wang, Q.; Du, A.; Wang, H.; Liu, G.; et al. Organic–Inorganic Bismuth (III)-Based Material: A Lead-Free, Air-Stable and Solution-Processable Light-Absorber beyond Organolead Perovskites. *Nano Res.* **2016**, *9* (3), 692–702.
(154) Park, B.-W.; Philippe, B.; Zhang, X.; Rensmo, H.; Boschloo, G.; Johansson, E. M. J. Bismuth Based Hybrid Perovskites A3Bi2I9 (A: Methylammonium or Cesium) for Solar Cell Application. *Adv. Mater.* **2015**, *27* (43), 6806–6813.
(155) Guarnera, S.; Abate, A.; Zhang, W.; Foster, J. M.; Richardson, G.; Petrozza, A.; Snaith, H. J. Improving the Long-Term Stability of Perovskite Solar Cells with a Porous Al2O3 Buffer Layer. *J. Phys. Chem. Lett.* **2015**, *6* (3), 432–437.

(156) Xiao, Z.; Dong, Q.; Bi, C.; Shao, Y.; Yuan, Y.; Huang, J. Solvent Annealing of Perovskite-Induced Crystal Growth for Photovoltaic-Device Efficiency Enhancement. *Adv. Mater.* **2014**, *26* (37), 6503–6509.
(157) Liu, J.; Gao, C.; He, X.; Ye, Q.; Ouyang, L.; Zhuang, D.; Liao, C.; Mei, J.; Lau, W. Improved Crystallization of Perovskite Films by Optimized Solvent Annealing for High Efficiency Solar Cell. *ACS Appl. Mater. Interfaces* **2015**, *7* (43), 24008–24015.
(158) Mali, S. S.; Kim, H.; Kim, D.-H.; Kook Hong, C. Anti-Solvent Assisted Crystallization Processed Methylammonium Bismuth Iodide Cuboids towards Highly Stable Lead-Free Perovskite Solar Cells. *ChemistrySelect* **2017**, *2* (4), 1578–1585.
(159) Li, J.-J.; Ma, J.-Y.; Hu, J.-S.; Wang, D.; Wan, L.-J. Influence of N,N-Dimethylformamide Annealing on the Local Electrical Properties of Organometal Halide Perovskite Solar Cells: An Atomic Force Microscopy Investigation. *ACS Appl. Mater. Interfaces* **2016**, *8* (39), 26002–26007.
(160) Bag, M.; Renna, L. A.; Adhikari, R. Y.; Karak, S.; Liu, F.; Lahti, P. M.; Russell, T. P.; Tuominen, M. T.; Venkataraman, D. Kinetics of Ion Transport in Perovskite Active Layers and Its Implications for Active Layer Stability. *J. Am. Chem. Soc.* **2015**, *137* (40), 13130–13137.
(161) Patterson, A. L. The Scherrer Formula for X-Ray Particle Size Determination. *Phys. Rev.* **1939**, *56* (10), 978–982.
(162) Abulikemu, M.; Ould-Chikh, S.; Miao, X.; Alarousu, E.; Murali, B.; Ndjawa, G. O. N.; Barbé, J.; Labban, A. E.; Amassian, A.; Gobbo, S. D. Optoelectronic and Photovoltaic Properties of the Air-Stable Organohalide Semiconductor (CH3NH3)3Bi2I9. *J. Mater. Chem. A* **2016**, *4* (32), 12504–12515.
(163) Lee, B.; Lee, S.; Cho, D.; Kim, J.; Hwang, T.; Kim, K. H.; Hong, S.; Moon, T.; Park, B. Evaluating the Optoelectronic Quality of Hybrid Perovskites by Conductive Atomic Force Microscopy with Noise Spectroscopy. *ACS Appl. Mater. Interfaces* **2016**, *8* (45), 30985–30991.
(164) Li, J.-J.; Ma, J.-Y.; Ge, Q.-Q.; Hu, J.-S.; Wang, D.; Wan, L.-J. Microscopic Investigation of Grain Boundaries in Organolead Halide Perovskite Solar Cells. *ACS Appl. Mater. Interfaces* **2015**, *7* (51), 28518–28523.
(165) Keddie, J. L.; Jones, R. A. L.; Cory, R. A. Size-Dependent Depression of the Glass Transition Temperature in Polymer Films. *EPL Europhys. Lett.* **1994**, *27* (1), 59.
(166) Keddie, J. L.; Jones, R. A. L.; Cory, R. A. Interface and Surface Effects on the Glass-Transition Temperature in Thin Polymer Films. *Faraday Discuss* **1994**, *98* (0), 219–230.
(167) Pham, J. Q.; Green, P. F. The Glass Transition of Thin Film Polymer/Polymer Blends: Interfacial Interactions and Confinement. *J. Chem. Phys.* **2002**, *116* (13), 5801–5806.
(168) Glynos, E.; Frieberg, B.; Chremos, A.; Sakellariou, G.; Gidley, D. W.; Green, P. F. Vitrification of Thin Polymer Films: From Linear Chain to Soft Colloid-like Behavior. *Macromolecules* **2015**, *48* (7), 2305–2312.
(169) Nguyen, H. K.; Prevosto, D.; Labardi, M.; Capaccioli, S.; Lucchesi, M.; Rolla, P. Effect of Confinement on Structural Relaxation in Ultrathin Polymer Films Investigated by Local Dielectric Spectroscopy. *Macromolecules* **2011**, *44* (16), 6588–6593.
(170) Casalini, R.; Prevosto, D.; Labardi, M.; Roland, C. M. Effect of Interface Interaction on the Segmental Dynamics of Poly(Vinyl Acetate) Investigated by Local Dielectric Spectroscopy. *ACS Macro Lett.* **2015**, *4* (9), 1022–1026.

(171) Sharma, R. P.; Green, P. F. Role of "Hard" and "Soft" Confinement on Polymer Dynamics at the Nanoscale. *ACS Macro Lett.* **2017**, *6* (9), 908–914.
(172) Chung, P. C.; Glynos, E.; Green, P. F. The Elastic Mechanical Response of Supported Thin Polymer Films. *Langmuir* **2014**, *30* (50), 15200–15205.
(173) Russell, T. P.; Chai, Y. 50th Anniversary Perspective: Putting the Squeeze on Polymers: A Perspective on Polymer Thin Films and Interfaces. *Macromolecules* **2017**, *50* (12), 4597–4609.
(174) Fang, J.; Zhu, T.; Sheng, J.; Jiang, Z.; Ma, Y. Thickness Dependent Effective Viscosity of a Polymer Solution near an Interface Probed by a Quartz Crystal Microbalance with Dissipation Method. *Sci. Rep.* **2015**, *5*, 8491.
(175) Mansfield, K. F.; Theodorou, D. N. Molecular Dynamics Simulation of a Glassy Polymer Surface. *Macromolecules* **1991**, *24* (23), 6283–6294.
(176) Kostas Ch. Daoulas; Vagelis A. Harmandaris; Mavrantzas*, and V. G. Detailed Atomistic Simulation of a Polymer Melt/Solid Interface: Structure, Density, and Conformation of a Thin Film of Polyethylene Melt Adsorbed on Graphite. *Macromolecules* **2005**, *38* (13), 5780–5795.
(177) Long, D.; Lequeux, F. Heterogeneous Dynamics at the Glass Transition in van Der Waals Liquids, in the Bulk and in Thin Films. *Eur. Phys. J. E* **2001**, *4* (3), 371–387.
(178) Merabia, S.; Long, D. Heterogeneous Dynamics at the Glass Transition in van Der Waals Liquids: Determination of the Characteristic Scale. *Eur. Phys. J. E* **2002**, *9* (2), 195–206.
(179) Mirigian, S.; Schweizer, K. S. Elastically Cooperative Activated Barrier Hopping Theory of Relaxation in Viscous Fluids. I. General Formulation and Application to Hard Sphere Fluids. *J. Chem. Phys.* **2014**, *140* (19).
(180) Wu, Y.; Haugstad, G.; Frisbie, C. D. Electronic Polarization at Pentacene/Polymer Dielectric Interfaces: Imaging Surface Potentials and Contact Potential Differences as a Function of Substrate Type, Growth Temperature, and Pentacene Microstructure. *J. Phys. Chem. C* **2014**, *118* (5), 2487–2497.
(181) Magonov, S.; Alexander, J. Single-Pass Kelvin Force Microscopy and DC/DZ Measurements in the Intermittent Contact: Applications to Polymer Materials. *Beilstein J. Nanotechnol.* **2011**, *2*, 15–27.
(182) Shen, Y.; Barnett, D. M.; Pinsky, P. M. Simulating and Interpreting Kelvin Probe Force Microscopy Images on Dielectrics with Boundary Integral Equations. *Rev. Sci. Instrum.* **2008**, *79* (2).
(183) Hiroyuki Sugimura; Kazuyuki Hayashi; Nagahiro Saito; Osamu Takai; Nobuyuki Nakagiri. Kelvin Probe Force Microscopy Images of Microstructured Organosilane Self-Assembled Monolayers. *Jpn. J. Appl. Phys.* **2001**, *40* (6S), 4373.
(184) Jang-Joo Kim; Sang-Don Jung; Wol-Yon Hwang. Molecular Conformation and Application of Stereoregular PMMA Langmuir-Blodgett Films. *ETRI J.* **1996**, *18* (3), 195–206.
(185) Costello, L. M.; Koros, W. J. Effect of Structure on the Temperature Dependence of Gas Transport and Sorption in a Series of Polycarbonates. *J. Polym. Sci. Part B Polym. Phys. 32* (4), 701–713.
(186) Wu, S. Chain Structure, Phase Morphology, and Toughness Relationships in Polymers and Blends. *Polym. Eng. Sci. 30* (13), 753–761.

(187) Gurau, M. C.; Delongchamp, D. M.; Vogel, B. M.; Lin, E. K.; Fischer, D. A.; Sambasivan, S.; Richter, L. J. Measuring Molecular Order in Poly(3-Alkylthiophene) Thin Films with Polarizing Spectroscopies. *Langmuir* **2007**, *23* (2), 834–842.
(188) Zhang, X.; Richter, L. J.; DeLongchamp, D. M.; Kline, R. J.; Hammond, M. R.; McCulloch, I.; Heeney, M.; Ashraf, R. S.; Smith, J. N.; Anthopoulos, T. D.; et al. Molecular Packing of High-Mobility Diketo Pyrrolo-Pyrrole Polymer Semiconductors with Branched Alkyl Side Chains. *J. Am. Chem. Soc.* **2011**, *133* (38), 15073–15084.
(189) Sugimura, H.; Hayashi, K.; Saito, N.; Nakagiri, N.; Takai, O. Surface Potential Microscopy for Organized Molecular Systems. *Appl. Surf. Sci.* **2002**, *188* (3–4), 403–410.
(190) Alexander, J.; Magonov, S.; Moeller, M. Topography and Surface Potential in Kelvin Force Microscopy of Perfluoroalkyl Alkanes Self-Assemblies. *J. Vac. Sci. Technol. B* **2009**, *27* (2), 903–911.
(191) Gala, F.; Zollo, G. Dielectric Properties of Self-Assembled Monolayer Coatings on a (111) Silicon Surface. *J. Phys. Chem. C* **2015**, *119* (13), 7264–7274.
(192) Yi, Y. W.; Robinson, H. G.; Knappe, S.; Maclennan, J. E.; Jones, C. D.; Zhu, C.; Clark, N. A.; Kitching, J. Method for Characterizing Self-Assembled Monolayers as Antirelaxation Wall Coatings for Alkali Vapor Cells. *J. Appl. Phys.* **2008**, *104* (2), 023534.
(193) DePalma, V.; Tillman, N. Friction and Wear of Self-Assembled Trichlorosilane Monolayer Films on Silicon. *Langmuir* **1989**, *5* (3), 868–872.
(194) Hölzl, J.; Schulte, F. K. Work Function of Metals. In *Solid Surface Physics*; Hölzl, P. D. J., Schulte, D. F. K., Wagner, D. H., Eds.; Springer Tracts in Modern Physics; Springer Berlin Heidelberg, 1979; pp 1–150.